NONLINEAR ELASTICITY, SEISMIC ANISOTROPY, AND PETROPHYSICAL PROPERTIES OF RESERVOIR ROCKS

A DISSERTATION
SUBMITTED TO THE DEPARTMENT OF GEOPHYSICS
AND THE COMMITTEE ON GRADUATE STUDIES
OF STANFORD UNIVERSITY
IN PARTIAL FULFILLMENT OF THE REQUIREMENTS
FOR THE DEGREE OF
DOCTOR OF PHILOSOPHY

By
Xingzhou Liu
June 1994

Abstract

A thorough understanding of the nonlinear elasticity, seismic anisotropy, and other petrophysical properties of rocks is essential to many fields, including geological engineering, petroleum exploration and production, and geophysical explorations. This dissertation presents new experimental and theoretical results on the applicability of second-order elasticity theory to the study of nonlinear elastic properties of rocks, the petrophysical/chemical causes for the seismic anisotropy of kerogen-rich shales, the petrophysical properties of carbonate rocks, and the role of linking rock physics and geostatistics in reservoir characterizations.

The second-order elasticity theory's applicability to rocks is examined using laboratory ultrasonic measurements. Beam-mixing experiments show that the properties of scattered waves from nonlinear wave interaction agree with predictions from the theory. The amplitude of the scattered waves decays with confining pressure as anticipated from the microscopic origin of nonlinearity in rocks. However, measured velocities of wave propagations under different states of stress (uniaxial and hydrostatic) reveal an inconsistency within the system of equations for stress-dependent velocities. This may be attributed to the approximations within the theory and, to a lesser extent, the experimental conditions. First, the stress-strain relation as adopted by Hughes and Kelly (1953) and others may be inappropriate to rocks which have a high degree of nonlinearity under finite load. Second, the third-order approximation of strain in elastic energy may not be enough for problems involving the interaction between static and dynamic stress. It is therefore concluded that second-order elasticity theory is applicable to nonlinear wave propagation phenomena but the approximations made in Hughes and Kelly (1953) and others may not be applicable to problems of wave propagations superimposed on finite load. The experiment shows that in the plane perpendicular to the direction of a uniaxial stress, the ratio of P- to S-wave velocities remains approximately independent of the stress magnitude. This observation allows the prediction of velocities under any states of stress from the hydrostatic measurements of P- and S-wave velocities only.

Three main textural features for the seismic anisotropy of kerogen-rich shales are 1) the preferred orientation of clay particles and other mineral grains; 2) the preferred alignment of the lenticular kerogen-clay mixture; and 3) the micro-lamination of low density kerogen-clay mixture with calcareous, siliceous, or phosphatic materials, and sometimes with highly concentrated kerogen. Bedding-parallel microcracks,

generated during either kerogen maturation or sample preparation, can greatly enhance elastic anisotropy. Factors that can affect the seismic velocity and anisotropy of fluid-saturated shales include fluid compressibility, velocity dispersion induced by fluid motion in pores, and the physical-chemical weakening of clay minerals. In low porosity shales, the weakening effect can significantly reduce S-wave velocities in all directions and P-wave velocity along bedding-parallel direction. Based on dispersion analysis and a comparison of laboratory ultrasonic measurements with sonic logs, it is concluded that ultrasonic and sonic measurements of velocity dispersion are in the same frequency range. Therefore, laboratory measurements can be used directly for field sonic log interpretations, given that the sonic tool configuration is considered. Modeling of the sonic response in the Monterey formation shales confirms the findings of dense fractures in thin, brittle, and more siliceous layers.

The petrophysical properties of carbonate rocks are investigated at core and well logging scales. The velocity-porosity relation for carbonates formed of dolomite, siliciclastics, and anhydrite is $V_p = V_o - 0.084\phi$ km/s (ϕ in %) where V_o depends on lithology. In-situ, lithologies can be inferred from gamma ray intensity N_t (in API unit) and V_p is modeled by $V_p = 6.85 - 0.0785\phi - 0.0162N_t$. It is shown that spectral instead of total gamma ray intensity should provide a better estimation of the lithology. Permeability k (in mD) can be predicted from ϕ through $\log_{10} k = 0.35\phi$. Finally, there exists a good linear correlation between acoustic impedance and velocity.

The role of linking rock physics and geostatistics in reservoir characterization is shown through the study of a carbonate reservoir. Rock physics provides the interrelationships between reservoir properties (porosity, permeability) and field measurables (seismic velocity, gamma ray intensity, etc.). It also provides an insight into the inevitable scatter or variability in any such interrelationships. One major cause for the scatter is the averaging or support effect, as shown from measurements made on core, logging, and crosswell supports. Geostatistics is used to map reservoir properties in regions with no direct measurements. With stochastic simulation, the resolution in a crosswell seismic survey is enhanced globally in that the simulated rock properties honor the velocity tomogram at the crosswell support and at the same time possess the desired spatial variability (variogram) at the core support. Also, geophysical data (core, well logging, and crosswell seismic measurements) on different supports and of different nature are effectively integrated.

Acknowledgements

I express my sincerest gratitude to my advisor Amos Nur for his encouragements, intelligent advice, and continuous financial support through my stay at Stanford.

Joining the Stanford Rock and Borehole Project (SRB) was my wish when I translated the review paper "Recent advances in rock physics" (Yale, 1984) for a Chinese journal, and it was my dream when I met Amos in China at the end of 1987. Now my dream has been well fulfilled.

I wish to thank SRB affiliates for their sponsorship and academic interest in my research. I am grateful to all faculty members and colleagues of the Geophysics Department, in particular, Amos Nur, Gary Mavko, Mark Zoback, Lev Vernik, and Tapan Mukerji, and Andre Journel of the Petroleum Engineering Department as my M.S. degree advisor in Geostatistics for their teaching, discussions, and other kinds of help. As one of the pioneers in rock physics, Amos has made SRB the greatest place for rock physics education and research, as demonstrated by the number of rock physicists who graduated before me and are now active in many parts of the world. I thank my dissertation committee members, especially Tom Hewitt of the Petroleum Engineering Department, for their reviews and many helpful suggestions. I am very indebted to Margaret Muir for always being there when I needed help.

The industrial experience I had during three summers has undoubtedly oriented me towards some of the technical frontiers in the oil industry. I thank Ken Winkler of Schlumberger-Doll Research and Richard Chambers of Amoco Production Research for providing me with the summer internships and the mentorship.

I am grateful to my wife Yanjie Dong who, being a Ph.D student (Stanford Medical School) herself, has undertaken many of the family chores during the past few years. She has dedicated her love to our success now and in the future.

My final gratitude is extended to my parents, grandmother, and sisters for their strong moral support. From them, I learned how education and knowledge can benefit everyone. The pursuit of knowledge has been and will be the goal of my whole life.

Contents

List of Tables

List of Figures

Chapter 1

Introduction

Nonlinear elasticity, seismic anisotropy, and other petrophysical properties of rocks are encountered in a variety of geophysical and geotechnical applications. Problems such as well-bore stability, earthquake prediction, and the seismic probing of stress distributions in the earth's crust all share the common physical basis of strain- or stress-dependent elasticity. To detect hydrocarbon sources using seismic methods, seismic anisotropy as one of the seismic signatures needs to be correlated with the petrophysical/chemical properties of shales, such as mineralogy, kerogen content, texture, porosity, and formation conditions. Finally, in reservoir characterizations, not only reservoir properties need to be related to field measurables, but the scale effect in integrating different geophysical measurements needs to be well understood. This chapter brings about the study topics covered in the following chapters, the methodologies used, and the future research potentials.

Though elastic nonlinearity is recognized as a general property of any material (Breazeal et al., 1984[1]), the study of rocks in the context of nonlinear elasticity theory is fairly recent. The two important aspects of such a study are nonlinear wave propagation or interaction, and the stress-dependence of the dynamic elastic properties. Recently, there has been strong interest in the nonlinear wave interaction in rocks (Johnson et al., 1987, 1989), the goal of study being the use of nonlinear properties of rocks for developing new seismic sources. However, scarce amount of data about the nonlinear parameters of rocks exist for any profound analysis. Though success of second-order theory for the study of nonlinear wave generation has been shown (Johnson el al., 1987), no experimental data is available for testing the theory's

[1]The authors state "A solid medium, in general, is nonlinear. This fact has been understood for many years because so many properties of solids are the result of macroscopic nonlinearity . . . pressure variation of the elastic constants, difference between the adiabatic and isothermal elastic constants, the damping of high-frequency sound waves ... all depend on either anharmonic theory for their microscopic description or nonlinear theory for their macroscopic description."

applicability to the stress-dependence of wave propagation velocities under finite load. The validity of the method based on the stress-strain relation given by Hughes and Kelly (1953) for measuring third-order elastic constants of rocks needs to be examined. It also remains a question whether it is possible to predict velocities of elastic waves under any states of stress.

In order to obtain the petrophysical and geochemical properties of shales from seismic measurements (surface, cross-well, and well logging), it is essential to understand how velocity and elastic anisotropy are affected by these properties as well as environmental factors such as pressure and saturating fluids. The general causes for the elastic anisotropy of rocks include the preferred orientation of clay (or other minerals) and microcracks, and bedding (Lo et al., 1985) or lamination. In kerogen-rich shales, however, the anisotropic distribution of low density kerogen can also cause strong intrinsic anisotropy (Vernik et al., 1992, Bakken formation). The bedding-parallel microcracks induced by hydrocarbon generation can greatly enhance the already strong effect (Vernik, 1993). It is of great interest (Thomsen, 1993) to extend and generalize the study to other shale formations and other important properties, such as the effects of saturating fluids and to propose a textural model for kerogen-rich shales for theoretical analysis. In order to apply laboratory ultrasonic results to field sonic interpretations, it is also very important to investigate the effects of frequency-related velocity dispersion and scale of measurement.

Two crucial steps in modeling formation properties for reservoir characterization are finding the relationships among different petrophysical properties of rocks and then integrating data of different natures and scales to build a reservoir description model. For carbonate rocks, there exist only a few studies on their seismic velocity and other petrophysical properties (e.g., Rafavich, 1983; Wilkens, 1984). Besides, these studies lack rock physics-based analysis and did not provide a link to in-situ applications. In reservoir characterization, the problem frequently arises that data from different measurements are quite different in terms of physical nature, support, and variability. It is therefore necessary to fully understand these effects and find a practical solution to data integration. To achieve this, a joint effect from different disciplines such as rock physics, geostatistics, and reservoir simulation is needed (Haldorsen and Damsleth, 1993).

The objectives of this thesis work are 1) to examine the applicability of second-order elasticity theory to the study of the nonlinear elastic properties of rocks; 2) to study the effects of the petrophysical/chemical properties of shales and measurement frequency/scale on the velocity and seismic anisotropy of kerogen-rich shales; and 3)

to find the petrophysical relations for carbonate rocks and to link rock physics and geostatistics in reservoir characterizations.

Chapter 2 is dedicated to the study of the nonlinear elastic properties of rocks. Ultrasonic experiments are used to examine whether second-order elasticity theory can be used to study both nonlinear wave propagation and stress-dependent elastic wave velocities. For nonlinear wave propagation, a noncollinear beam mixing experiment is conducted to compare the measured properties of nonlinear waves with predictions from the theory and a collinear beaming experiment is used to verify the micro-mechanical origin of the elastic nonlinearity in rocks. These studies are the experimental basis for applications like the nonlinear beam generation for use as seismic or sonic sources, the prediction of wave propagation velocities under any states of stress (e.g., around a borehole), the study of the relationship between static and dynamic moduli, and the study of such petrophysical properties as diagenesis and velocity dispersion.

In Chapter 3 the laboratory measurements on velocity and other petrophysical properties of kerogen-rich shales are presented and analyzed in terms of the average and direction-dependent properties, the effects of saturating fluids, and the sonic response of the Monterey formation shales. Through a shale project of which this study belongs to, the largest data collection on shales is generated that covers the lithology, porosity, permeability, velocity, elastic anisotropy, petrography, etc. It provides the petrophysical basis for seismic (surface, cross-well, and logging) or other types (Passey, 1990) of interpretations of source rocks.

In Chapter 4 the matrix velocity in a velocity-porosity relation for carbonate rocks formed of dolomite, siliciclastic sediments, and anhydrite are studied using effective medium theory. Predictions from the theory are compared with the experimental measurements. For field inference of lithology, the use of both total and spectral gamma ray intensities is studied. Various sources of scatter, especially the averaging effect, in relating different geophysical measurements are analyzed. Interwell reservoir properties are modeled using a geostatistical simulation technique through which core, well logging, and cross-well seismic measurements can be effectively integrated. The results are compared with field data for model validation. This study emphasizes the importance of rock physics study in reservoir characterization and provides one solution to the data integration problem.

The last chapter is a collection of all experimental data for this dissertation. It is self-contained with detailed descriptions of the experimental design and procedures, the equipment used, and finally complete tables of data.

References

Breazeale, M.A. and J. Philip , 1984, Determination of third-order elastic constants from ultrasonic harmonic generation measurements, in Physical Acoustics, XVII, ed. by W.P. Mason.

Haldorsen, J. H. and E. Damsleth, 1993, Challenges in reservoir characterization, AAPG Bulletin, **77**, 541-551.

Hughes, D. S., and I. I. Kelly, 1953, Second-order elastic deformation of solids, Phys. Rev., **92**, 1,145-1,149.

Johnson, P. A., T. J. Shankland, R. J. O'Connell, and J. N. Albright, 1987, Nonlinear generation of elastic waves in crystalline rock, J. Geophys. Res., **92**, 3,597-3,602.

Johnson, P. A. and T. J. Shankland, 1989, Nonlinear generation of elastic waves in granite and sandstone, J. Geophys. Res., **94**, 17,729-17,733.

Lo, T. W., K. B. Coyner, and M. N. Toksoz, 1986, Experimental determination of elastic anisotropy of Berea sandstone, Chicopee shale, and Chelmsford granite: Geophysics, **51**, 164-171.

Thomsen, L., 1993, personal communications.

Passey, Q. R., S. Creaney, J. B. Kulla, F. J. Moretti, and J. D. Stroud, 1990, A practical model for organic richness from porosity and resistivity logs, AAPG Bulletin, **74**, 1777-1794.

Vernik, L., and A. Nur, 1992, Ultrasonic velocity and anisotropy of hydrocarbon source-rocks, Geophysics, **57**, 727-735.

Vernik, L., 1993, Microcrack-induced versus intrinsic elastic anisotropy in mature HC-source shales, Geophysics, **59**, 555-563.

Yale, D. P.,[2] Recent advances in rock physics, Geophys., **50**, 2480-2491.

[2]See **Acknowledgements** on page vi for its referencing.

Chapter 2

Nonlinear elasticity of rocks

Abstract

The second-order elasticity theory's applicability to the study of nonlinear elastic properties of rocks is examined using laboratory ultrasonic measurements. The experiment of noncollinear beam-mixing of two monochromatic waves shows that properties of scattered waves from nonlinear wave interaction agree with those of predictions, demonstrating the theory's validity for describing nonlinear elastic wave propagation/interaction. The amplitude of scattered waves is estimated to be 20 to 40 dB lower than those of the primaries and it decreases with increasing confining pressure, as anticipated from the micro-mechanical origin of nonlinearity in rocks. For stress-dependent velocities, however, the equations derived from second-order elasticity theory are not supported by experimental data. This incompatibility may be due to 1) the stress-strain relation adopted by Hughes and Kelly (1953) and others may be inappropriate for rocks because of the large strain induced by finite load; and 2) the third-order approximation of strain in elastic energy may be not enough for problems involving finite load. Experimentally, the deviation of actual stress in test samples from the uniaxial distribution may be another reason. Therefore, further theoretical and experimental work is needed. It is found that for most samples in this study, the ratio of P- to S-wave velocities for wave propagations in the plane perpendicular to the direction of a uniaxial stress remains approximately independent of the stress magnitude. This observation allows the prediction of velocities under any states of stress from the hydrostatic measurements of P- and S-wave velocities only. Based on petrographical analysis, it is shown that the variation of velocities with stress is intimately related to the texture of granular materials.

2.1 Introduction

Nonlinearity is behind many commonly studied phenomena in rock elasticity: curved stress-strain relations under uniaxial loading, increase of wave propagation velocity with hydrostatic confining pressure, and the disagreement between static and dynamic moduli are some of the examples. The importance of studying nonlinear elasticity, therefore, reaches into many fields such as engineering geology, reservoir engineering, geophysical exploration, and so on.

Recently, there has been increasing interest in exploring the nonlinear elastic properties of rocks (Johnson et al., 1987; Bonner el al., 1992; Johnson et al., 1993), and second-order elasticity theory has been used to study nonlinear wave propagation (McCall, 1994) and to derive higher-order elastic constants of rocks (Bakulin, 1982). The experimental principle in Bakulin (1982) and Johnson et al. (1993) is based on equations of stress-dependent velocities of Hughes and Kelly (1953), which are derived from second-order elasticity theory under certain approximations to total strain resultant from wave propagation superimposed on finite load. So far, however, there has been no experimental work to test the applicability of these equations as applied to rocks. Measurements of third-order elastic (TOE henceforth) constants are abundant in the field of solid state physics,[1] mostly in single crystalline materials (Breazeale, 1983). For rocks, though much data on stress-dependent velocities exist (see e.g., Gupta, 1973; Bonner, 1974; Lockner, 1977, or the CRC Handbook by Carmichael, 1981), they are all incomplete for deriving all TOE constants.

There exist many models that are based on the concept of microcrack for explaining the behavior of stress-dependent velocities (Walsh, 1965; Budiansky et al., 1975; Sayers et al., 1988) The problems with crack models are that they frequently involve idealized approximations such as ellipticity of crack shapes which are seldomly relevant to realistic grain contacts, cracks, or mini-fractures of rocks. When applied to experimental measurements, the end-results of these models are none other than inverting measured velocities for parameters like aspect ratio, crack density, and crack distribution (e.g., Sayers et al., 1990) which are of limited use. On the other hand, the mathematically simpler but more rigorous nonlinear elasticity theory can directly relate velocities to any states of stress through combinations of second- and higher-

[1]This is a big advance considering what Murnaghan said in his classical book *Finite deformation of an elastic solid* (1951), "We have, so far, very little experimental knowledge of the third-order elastic constants or of the effect of applied stress upon the second-order elastic constants. If the mathematical treatment given here serves to stimulate the procurement of experimental knowledge of these phenomena we shall have attained our aim."

order elastic constants. However, though well accepted in solid state physics, this approach has not received enough attention in rock physics. This inattention is, to a larger extent, because of the misbelief that nonlinear theory is used only for large amplitude phenomena such as shock waves from explosions without realizing that the stress dependence of elastic wave propagations is also one of the important properties of nonlinear elasticity. Another reason for the inattention is that experimental work devoted to obtaining all the elastic constants for fully characterizing the elastic properties of a rock sample almost does not exist.

In this chapter I examine the applicability of second-order elasticity theory to two important phenomena: nonlinear wave interaction and stress-dependent elastic wave propagations. The ultrasonic beam-mixing experiment is used to study nonlinear wave interaction. Measurements of ultrasonic velocities under different states of stress are used to check the appropriateness of Hughes and Kelly's (1953) equations to stress-dependent velocities. Finally, the different behavior of velocities under uniaxial stress is explained using models based on the contact mechanics of granular materials.

2.2 Linear versus nonlinear elasticity

First of all, it needs to be understood why nonlinear elasticity theory has to be used for the many elastic properties of rocks and, qualitatively, what causes the nonlinearity.

2.2.1 Why rocks are nonlinear?

A linear elastic solid is defined (Fung, 1965 p.2) as a body that satisfies three hypotheses: continuum, Hooke's law, and a unique unstressed state. The hypothesis of continuum requires that no cracks may open up upon the action of external load. Hooke's law, in its simplest form, stipulates that the displacement u of a point relates to a set of forces P_1, P_2, ..., and P_n by

$$u = a_1 P_1 + a_2 P_2 + ... + a_n P_n$$

where a_1,a_2, ..., a_n are *constants* independent of the *magnitude* of P_1,P_2, ..., P_n.

Rocks obey none of the above hypotheses: not only are cracks prevalent, but also new cracks may open up at even low loads, elastic constants of rocks may vary with external force, and there is strong hysteresis in the elastic properties of rocks. Should Hooke's law be used for rocks, either the stress has to be infinitesimal or the problem be confined to a constant finite stress state. The common practice in geophysics, however, has been to treat finite stress as a function of location coordinates and the

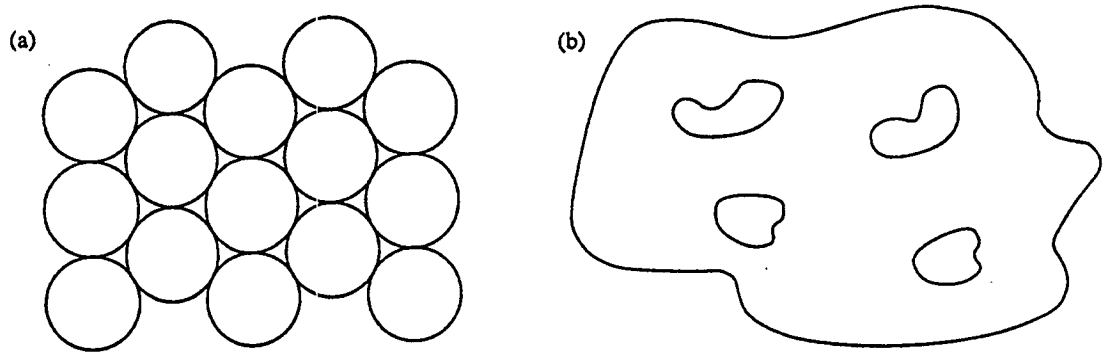

Figure 2.1: Two commonly used models of rocks: (a) an assemblage of discrete grains in contact; (b) a solid matrix containing voids. (after Zimmerman, 1991) The compliant grain contacts or pores can give rise to high intrinsic nonlinearity of rocks.

material "constants" as a function of stress through location coordinates, so Hooke's law becomes

$$u = \sum_i a_i(P_1(\vec{r}), P_2(\vec{r}), ..., P_n(\vec{r}))P_i$$

Therefore, when describing seismic wave propagation (in regions away from the source) with a linear wave equation, it should keep in mind that the variation of elastic properties with depth is due to both lithology and lithostress. This practice successfully avoids the many problems arising from nonlinearity (complexity in a wave equation, among others), but at the same time impedes the understanding of many important properties, such as the behavior of velocities under different states of stress (i.e., other than just hydrostatic), the discrepancy between static and dynamic moduli, and many wave propagation properties, such as nonlinear interaction of mixing beams.

2.2.2 Causes for nonlinearity

In single crystalline solids, elastic nonlinearity is related to the anharmonic crystal lattices. In rocks, however, this effect is negligible compared with the mechanical effects of micro-cracks (such as those thermally developed or generated during pressure relief or mechanical damaging), compliant grain contacts, and mini-fractures (see Figure 2.1). A typical exhibition of these effects is the near exponential curved velocity increase versus hydrostatic confining pressure in rocks (see e.g., Bourbie, 1987). These causes for nonlinear elasticity in rocks will be elaborated further in Section 2.5.

2.2.3 Effects of nonlinear elasticity

A direct consequence of elastic nonlinearity is that many elastic properties of rocks become dependent on strain or stress amplitudes. Also, the principle of superposition no longer holds. For elastic wave propagations with or without an overloading stress, some effects of elastic nonlinearity are

- an initially sinusoidal P-wave of a given frequency distorts as it propagates;
- a pure mode S-wave cannot exist without an accompanying P-wave;
- two waves of different frequencies may interact with each other, generating a third wave with either the sum or the difference frequency of the two primaries;
- the wave propagation velocity is affected by a superimposed static stress.

The last two effects are chosen for this study because of their importance in both applications (such as nonlinear beam generation and borehole stability prediction) and the theoretical analysis of the second-order elasticity theory's applicability to the nonlinear elastic properties of rocks.

2.3 Nonlinear wave interaction

Nonlinear wave interaction (beam mixing) has a wide range of applications. It has been used to determine certain combinations of TOE constants (Rollins, 1963; Dunham and Huntington, 1970), to illustrate the interaction of phonons in solid state physics (Taylor and Rollins, 1964), and to study the potential of using the nonlinear elastic properties of rocks for developing new seismic sources (Johnson *et. al.*, 1989). Following Johnson and Shankland (1987), an experiment was designed to study the properties of nonlinear wave interaction, including 1) the primary to nonlinear wave conversion efficiency, which is needed for field applications such as the design of new seismic sources; 2) the pressure variation of the nonlinear effect to see how overloading stress can affect the effectiveness of nonlinear wave conversion; and 3) the applicability of second-order elasticity theory to nonlinear wave propagations. Below, the principle behind nonlinear wave interaction will be given first, which is then followed by measurement results and an analysis.

2.3.1 Theory

Since the principle of superposition no longer holds in nonlinear elasticity theory, a solution to the equations of motion cannot be written as a linear combination of monochromatic waves. When two plane elastic waves interact, a third wave (scattering wave) can be produced as a solution to the nonlinear equations of motion (see Appendix).

In this section, two cases of nonlinear wave interaction are studied: noncollinear and collinear beam mixing, to test the second-order elasticity theory's applicability to nonlinear wave propagation by comparing the predictions from the theory with the experimental results.

Case I: noncollinear beam mixing

The interaction[2] of two noncollinear propagating longitudinal waves (continuous wave) is investigated here and the properties of the scattered waves are given below.

When two monochromatic longitudinal waves (primaries) ($\vec{k}_1$, ω_1) and ($\vec{k}_2$, ω_2) intersect at angle φ, the scattered wave is of shear mode whose frequency equals the difference between the two primaries, $\omega_1 - \omega_2$ (it is therefore called the difference frequency wave or nonlinear wave since it cannot occur within domain of linear elasticity). The conservation of energy and momentum requires that the interaction angle φ be (Jones and Kobett, 1962):

$$\cos\varphi = 1/c^2 + (c^2 - 1)(a^2 + 1)/2ac^2 \tag{2.1}$$

where $c = V_s/V_p$ is the velocity ratio, $a = \omega_1/\omega_2$ ($\omega_2 < \omega_1$, without loss of generality) is the frequency ratio, and the outgoing angle γ (relative to $\vec{k}_1$) of the scattered wave is given by ($\vec{k}_1 - \vec{k}_2$) or

$$\tan\gamma = \frac{-a\sin\varphi}{1 - a\cos\varphi} \tag{2.2}$$

Equations 2.1 and 2.2 mean that for a given velocity ratio, the geometry for the directions of primary and scattering waves is fixed once the frequency ratio is fixed.

The amplitude of the scattered wave is (Taylor and Rollins, Jr., 1964)

$$X^s = X_1X_2V\omega_1^3\frac{a(1+a)}{16\pi r\rho V_p^4V_s}(2B + A + K + \frac{7\mu}{3})\sin(2\varphi)\cos\theta \tag{2.3}$$

[2]Depending on the wave modes (longitudinal, L or transverse, T), there may be five interaction types between two monochromatic waves with frequencies ω_1 and ω_2 that generates either the sum or the difference frequency waves: $T(\omega_1) + T(\omega_1) \rightarrow L(\omega_1 + \omega_2)$; $L(\omega_1) + L(\omega_1) \rightarrow L(\omega_1 - \omega_2)$; $L(\omega_1) + T(\omega_1) \rightarrow L(\omega_1 + \omega_2)$; $L(\omega_1) + T(\omega_1) \rightarrow L(\omega_1 - \omega_2)$; and $L(\omega_1) + T(\omega_1) \rightarrow T(\omega_1 - \omega_2)$.

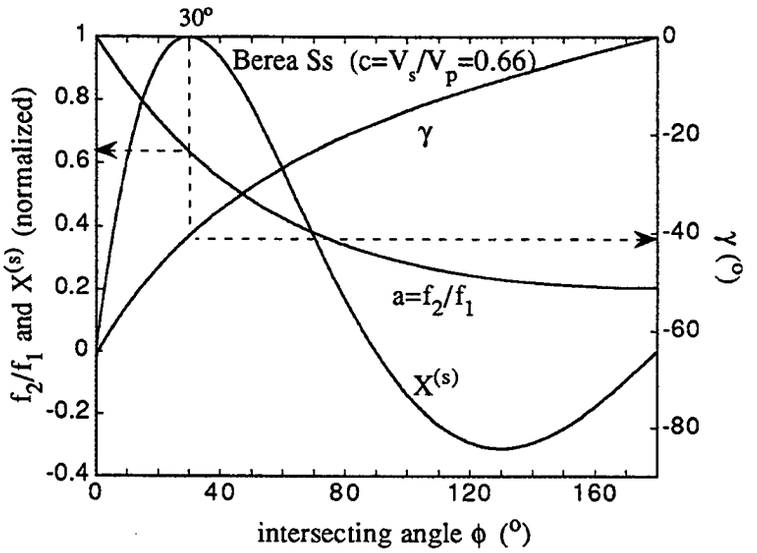

Figure 2.2: Frequency ratio $a = f_2/f_1$ of the two primary P-mode waves and the amplitude $X^{(s)}$ of the difference frequency wave (S-mode) plotted against the intersecting angle ϕ in a $L(\omega_1) + L(\omega_1) \rightarrow T(\omega_1 - \omega_2)$ mode interaction.

which is proportional to the product of the two primary wave amplitudes X_1 and X_2, the interaction volume V, a combination of second- and third-order elastic constants, and inversely proportional to the distance r between the recording point and the interaction point. It is also determined by the primary wave frequencies, ω_1 and $\omega_2 = a\omega_1$, intersecting angle φ, and receiver polarization angle θ. In Figure 2.2, the angle or frequency ratio dependent part $a(1+a)\sin(2\varphi)$ is plotted versus φ for Berea sandstone, assuming that receiver polarization is in the plane of the two primary beams ($\theta = 0$). It can be seen that in order to achieve maximum amplitude (maximum energy conversion from primaries to the scattering wave), the angles φ has to be 30^o and 32^o for Berea sandstone and marble respectively. Accordingly, the outgoing angles are -71^o and -76^o, respectively.

Case II: collinear beam mixing

With the collinear beam mixing experiment, the effect of confining pressure on the nonlinear wave generation is investigated. Since the strong nonlinearity of rocks comes from microcracks, the effect should decrease as the microcracks close. The gradual closure of microcracks can be achieved by applying a confining pressure to the sample.

When two longitudinal waves propagate along the same direction, the equation of motion for the displacement becomes the same as the acoustic equation in fluid. The

amplitude of the difference frequence wave , modified from Lamb's solution (Lamb, 1931) for solids, is given by

$$X^p = X_1 X_2(\omega_1 - \omega_2)\frac{L}{16\alpha^2}(3\alpha + 2A + 6B + 2C) \tag{2.4}$$

where L is the propagation distance and $\alpha = K + \frac{4}{3}\mu$.

2.3.2 Experimental procedure and results

The second-order elasticity theory's applicability is examined by comparing with experiments the following theoretical predictions:

1. For a given rock sample, the frequency ratio $a = f_2/f_1$ is constant when the interaction angle φ is fixed;

2. When all elastic constants are constant, the amplitude of the scattered waves is proportional to the product of the amplitudes of the two primary waves;

3. When confining pressure is increased, the scattered wave amplitude should decrease because of the increase in velocities, as seen from equation.

For the noncollinear beam-mixing experiment, two rock samples were used, Berea sandstone and marble. They were cut into a pre-determined geometry (fixed φ and γ, see Figure 2.3 (a)) to allow maximum amplitude of the scattering wave and to allow monitoring of primary wave amplitudes. In addition to two P-mode transducers used for transmitting the two primary waves and one S-mode transducer for receiving the scattered wave, two other P-mode receivers are used to record the frequency response of the two P-mode transmitters. For the collinear beam-mixing experiment, only Berea sandstone is used. The sample-transducer configuration is shown in Figure 2.3. Two P-mode PZT crystals (unbacked) were stacked to be used as P-wave transmitters operating at two different frequencies. The receiver is also a P-mode transducer.

The properties of the samples are shown in Table 2.1 along with angles and frequency ratios for the maximum amplitude of scattered wave. Before the experiment, the samples were oven-dried for 24 hours, then left at room conditions for another 24 hours.

In the noncollinear beam-mixing, the frequencies of the two primary waves were allowed to vary. The procedure is as follows: ω_1 is fixed first, and ω_2 is allowed to sweep within a range, then ω_1 is increased, and ω_2 swept through the same range again. This is repeated for several ω_1's. The collinear beam-mixing followed the same procedure. The schematic diagram for the experimental set-up is shown in Figure 2.3 (b). In this experiment, it is very important to keep the harmonics of

sample	density (g/cm^3)	V_p (km/s)	V_s (km/s)	c	φ $(^\circ)$	γ $(^\circ)$	a
Berea Ss	2.12	2.22	1.46	0.66	30	-71	0.64
Marble	2.68	5.28	2.96	0.56	32	-76	0.68

Table 2.1: Density, velocities, and geometries of samples used for beam-mixing experiment.

primary frequency waves as low as possible. The purity of the single frequency output from the HP3325B frequency synthesizer meets such a requirement. The recording time for each sample is about 72 hours.

Frequency ratio

The spectra for the scattering wave versus f_2 ($f = \omega/2\pi$) in Berea sandstone are shown in Figure 2.4. The frequency ratio of f_2/f_1, corresponding to the peak amplitude in the difference-frequency wave, is plotted versus f_1 in Figure 2.5 (b). It is 0.62 for $f_1 = 500$ kHz and 0.57 for $f_1 = 1000$ kHz, close to the predicted value 0.64. The discrepancy may be explained by "velocity dispersion". When plotting the velocity ratio c as calculated from 2.1 using measured frequency ratio a ($c = V_s/V_p = (1-a)^2/(1+a^2-2a\cos\varphi)$), we see that it varies with f_1. The extrapolation of the linear fit to zero frequency gives 0.66, the velocity as measured from the first break of broadband signals. It is interesting to note that when extrapolating the linear fit of the frequency ratio to zero frequency, we get $a = 0.64$ exactly as predicted.[3]

Amplitude relationship

The primary wave amplitudes was measured separately by sweeping one of the frequencies. The difference frequency amplitude X^s is plotted versus the product of the amplitudes of the two primary waves X_1 and X_2 in Figure 2.5 (a) (in dB scale) and a good linearity is shown. This shows that X^3 is proportional to the product of the amplitudes of the two primary waves.

Therefore, both amplitude and geometry of the scattered wave agree with those of

[3]This finding may be used to study the velocity dispersion in saturated rocks. It has been shown theoretically that at least two flow mechanisms (Biot, 1956; Mavko, 1975; and O'Connell, 1977) can cause steep increases in velocity in rocks as frequency varies from seismic to ultrasonic frequency range. Because of the inconsistency in experimental techniques for different frequency bands, so far there has been no report of velocity measurement covering a wide enough frequency range. Also, the velocity as calculated from the first break using ultrasonic broadband signal may not represent "high frequency" velocity.

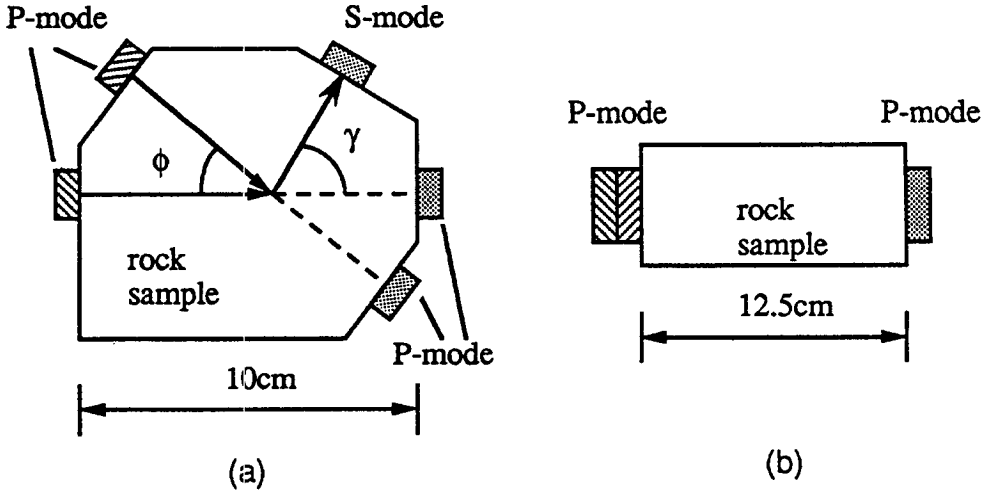

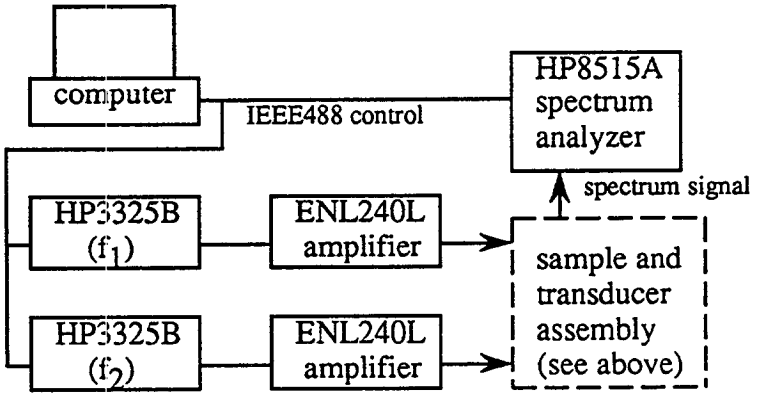

Figure 2.3: Top: Sample configurations for the noncollinear (a) and collinear (b) beam-mixing experiment; Bottom: The schematic diagram of devices used in beamming experiment.

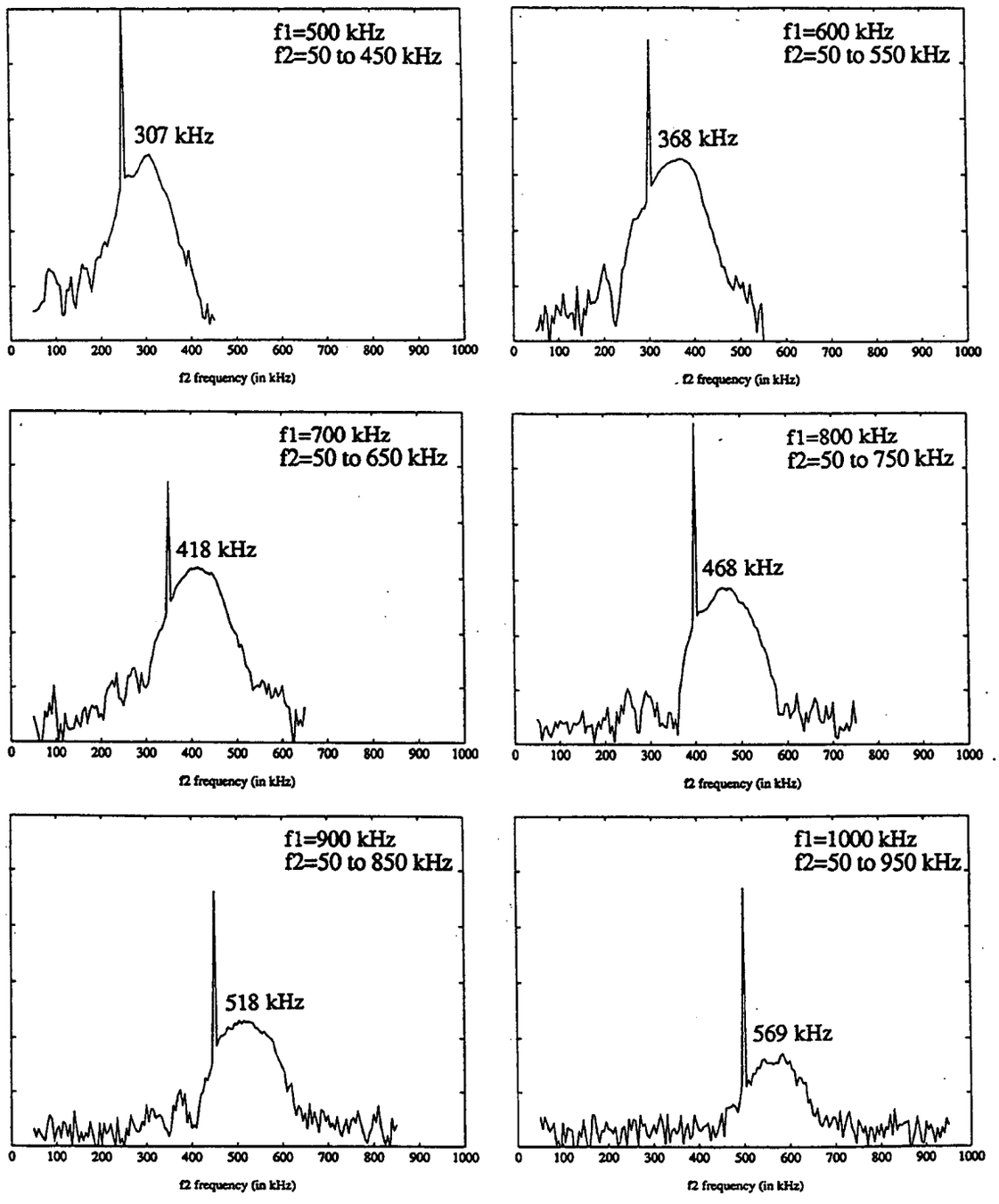

Figure 2.4: Spectra of the difference frequency wave upon sweep of one primary frequency (ω_2) while the other (ω_1) is fixed. Six frequencies for (ω_1) are shown.

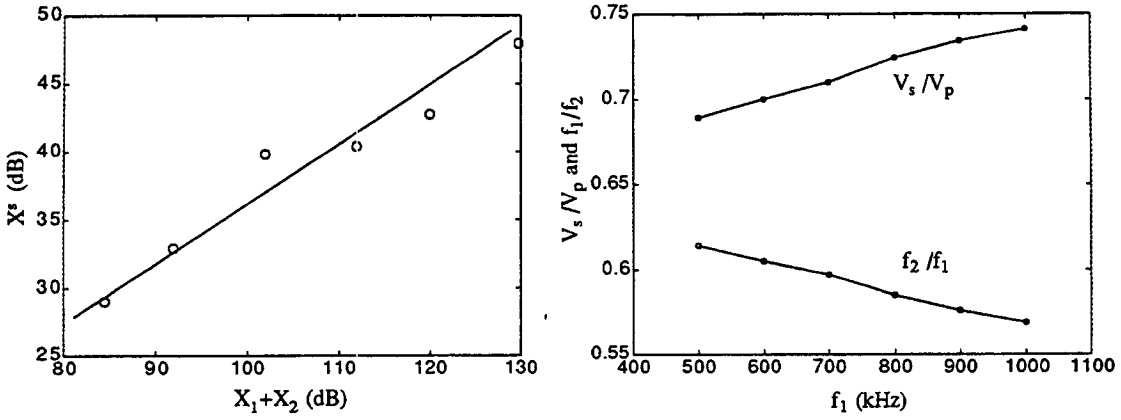

Figure 2.5: (a) Amplitude of the difference frequency wave versus the product of the two primary wave amplitudes; (b) The frequency ratio corresponding to the resonance of interaction and the calculated velocity ratio.

predictions as given by Equations 2.1, 2.2, and 2.3, demonstrating the applicability of the second-order elasticity theory to the nonlinear wave phenomena. Other results of beam-mixing experiment concern the energy conversion from primary waves to scattered wave and the pressure dependence of TOE constants.

Conversion efficiency

The estimation of the exact energy conversion efficiency is difficult because consideration of such factors as the radiation pattern of transducers, the P-S wave mode conversion, and incidence angle have to be involved. As estimated from the S-mode transducer along the propagation direction of scattering wave, the scattered wave is about 20 to 40 dB lower than the primaries. Considering the use of a S-mode transducer to receive P-mode signal and other factors, an estimate of the conversion efficiency is that the scattered wave has an amplitude of 40-50 dB lower than the primaries and the power conversion efficiency is around 10^{-5}. Using Equation 2.3 it is estimated that the order of magnitude of TOE constants is around 10^{13} Pa.

Pressure dependence of the nonlinear wave amplitude

The velocities of rocks depend strongly on the confining pressure, as shown in Figure 2.6 for Berea sandstone. This can cause a drastic decrease in the nonlinearly generated wave amplitude. This is shown in Figure 2.6, which plots the pressure dependence of amplitudes of the difference wave along with the product of the two primaries. The frequencies of the two primary waves are 300 kHz and 278 kHz, with the difference-frequency wave frequence being 22 kHz.

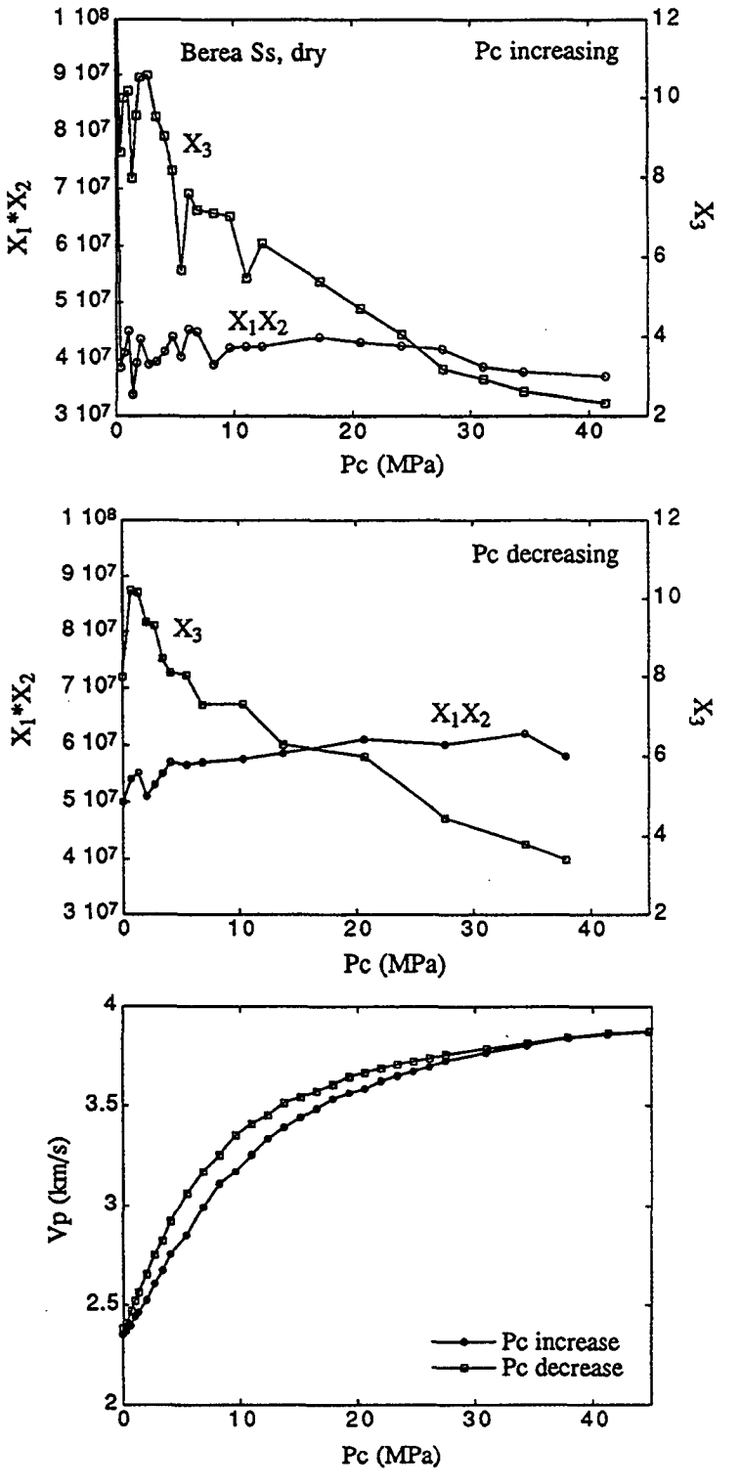

Figure 2.6: The pressure dependence of the P-wave velocity, the product of the two primary wave amplitudes, and the difference frequency wave amplitude.

2.4 Stress-dependent velocities

Higher-order elastic constants are as basic to nonlinear elasticity theory as second-order elastic constants are to linear elasticity theory. In fact, they contain more information about rock properties, especially when stress variation is involved. In this section, the principle of deriving TOE constants from stress-dependent velocities as proposed by Hughes et al. (1953) are examined using measurement results for a number of rock samples. Results of TOE constants are presented and the possibility of predicting velocities under uniaxial stress from hydrostatic measurements is discussed.

2.4.1 Equations for stress-dependent velocities

A number of authors (Hughes et al., 1953; Thurston et al., 1964; Green, 1973) have derived from second-order elasticity theory equations relating TOE constants to velocities of elastic wave propagations to stresses under different states. The recount below highlights the approximations used in these theoretical work and lays out the experimental principle for measurement of TOE constants.

In the formulation by Hughes et al. (1953), strain η_{rs} caused by wave propagation superimposed upon a homogeneous triaxial load in an isotropic solid is given by

$$\eta_{rs} = \alpha_r \delta_{rs} + (1 + \alpha_r + \alpha_s) e_{rs}, \tag{2.5}$$

where $\alpha_{r,s}$ are terms of (static) strain arising from the finite load (uniaxial stress or hydrostatic pressure) and e_{rs} is the ordinary infinitesimal (dynamic) strain arising from wave propagation. The first term describes the finite stress itself. The second term represents the coupling between the wave propagation and the finite load. The velocities of wave propagation for any direction are solutions to the equation of motion, which are given by

$$\begin{aligned} \rho {V_1}^2 &= \lambda + 2\mu + (2l + \lambda)\theta + (4m + 4\lambda + 10\mu)\alpha_1 \\ \rho {V_2}^2 &= \mu + (\lambda + m)\theta + 4\mu\alpha_1 + 2\mu\alpha_2 - \tfrac{1}{2}n\alpha_3 \\ \rho {V_3}^2 &= \mu + (\lambda + m)\theta + 4\mu\alpha_1 + 2\mu\alpha_3 - \tfrac{1}{2}n\alpha_2 \end{aligned} \tag{2.6}$$

where λ and μ are secondary-order elastic (SOE) constants, l, m, n are TOE constants (Murnaghan constants), and $\theta = \alpha_1 + \alpha_2 + \alpha_3$ is the (static) volumetric strain.

In the above equations, the velocity squares are linear functions of the static strain α_r. Assuming (Hughes et al., 1953) that α_r can be linearly related to the finite

S	$\vec{N}$	M	$\vec{u}$	$\rho V^2(S)$	
P	any	L	$\parallel \vec{N}$	ρV_p^2	$= \lambda + 2\mu + (P/K)\,[2l + \frac{4}{3}m + \frac{7}{3}\lambda + \frac{10}{3}\mu]$
P	any	S	$\perp \vec{N}$	ρV_s^2	$= \mu + \quad (P/K)\,[m - \frac{1}{6}n + \lambda + 2\mu]$
T	$\parallel \vec{T}$	L	$\parallel \vec{N}$	$\rho V_{p\parallel}^2$	$= \lambda + 2\mu + (T/E)\,[\frac{2\mu}{\lambda+\mu}l + 4m + 4\lambda + 10\mu + \frac{\lambda\mu}{\lambda+\mu}]$
T	$\parallel \vec{T}$	S	$\perp \vec{N}$	$\rho V_{s\parallel}^2$	$= \mu + \quad (T/E)\,[\frac{\mu}{\lambda+\mu}m + \frac{\lambda}{4(\lambda+\mu)}n + 4\mu]$
T	$\perp \vec{T}$	L	$\parallel \vec{N}$	$\rho V_{p\perp}^2$	$= \lambda + 2\mu + (T/E)\,[\frac{2\mu}{\lambda+\mu}l - \frac{2\lambda}{\lambda+\mu}m - 2\lambda\frac{\lambda+2\mu}{\lambda+\mu}]$
T	$\perp \vec{T}$	S	$\parallel \vec{T}$	$\rho V_{s\perp 1}^2$	$= \mu + \quad (T/E)\,[\frac{\mu}{\lambda+\mu}m + \frac{\lambda}{4(\lambda+\mu)}n + \mu\frac{\lambda+2\mu}{\lambda+\mu}]$
T	$\perp \vec{T}$	S	$\perp \vec{T}$	$\rho V_{s\perp 2}^2$	$= \mu + \quad (T/E)\,[\frac{\mu}{\lambda+\mu}m - \frac{1}{2}n - \frac{2\lambda\mu}{\lambda+\mu}]$

Table 2.2: Stress-dependent velocities for waves under different states of stress S (P - hydrostatic; T - uniaxial) and with different propagation directions $\vec{N}$, modes M (L - longitudinal; S - shear), and polarizations $\vec{u}$. In the equations, ρ is the density, λ and μ are Lamé constants, l, m, n are third-order elastic constants, $K = \lambda + 2\mu/3$, and $E = \mu(3\lambda + 2\mu)/(\lambda + \mu)$.

load, the velocity squares can then be expressed as the linear functions of the applied stress, as presented in Table 2.2 for waves under different states of stress (hydrostatic or uniaxial) and with different propagation directions, modes (longitudinal or shear), and polarizations (refer to Figure 2.8 for definitions of velocity symbols). It can be seen from the velocity expressions that the changes in velocities at elevated stress are related to combinations of SOE and TOE constants as well as the stress (P or T). Note also that if terms involving only SOE constants can be ignored, which is the case for rocks, it follows $V_{s\parallel} \approx V_{s\perp 1}$. This condition can be used to check the uniaxial stress condition is satisfied (not done in this work). It should be pointed out here that when a solid is said to be linear, it does not mean that TOE constants are zero. Rather, it means that either the static strains P/K or T/E are so small that they are regarded as zero, or only the small fluctuations caused by wave propagation are interested, as illustrated in Figure 2.7.

The assumptions/limitations of the above principle are summarized below:

- the solid is isotropic and homogeneous.
- the stress is homogeneous (uniaxial or hydrostatic).
- the stress change is small enough that the linear stress-strain relationship holds for the finite load.

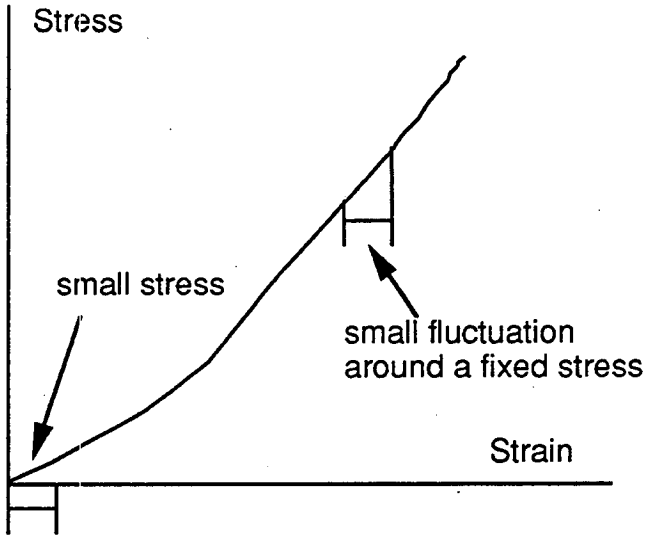

Figure 2.7: Schematic stress-strain diagram explaining the meaning of a solid being "linear": either the stress or strain are small enough (at the origin) or only their fluctuations are of interest.

Because the nonlinearity of rocks is usually very high, these assumptions/limitations imply that TOE constants calculated from velocities deviations from a hydrostatic stress state P are only valid to that stress state. Therefore, to obtain TOE constants at a stress range, one needs to measure the set of velocity-stress curves at fine enough intervals within the stress range of interest.

2.4.2 Experimental procedure

The ideal equipment for the measurement of TOE constants from variation of ultrasonic velocities with applied stress is a triaxial cell plus an ultrasonic measurement system. Since a triaxial cell was not available, the experiment was conducted with two separate devices: one for measurements of velocities under hydrostatic pressure and the other for measurements under unconfined uniaxial stress. Therefore, the calculated TOE constants are valid for atmospheric pressure only.

In this experiment, 6 velocities were measured, which are V_p, V_s, $V_{p||}$, $V_{p\perp}$, $V_{s\perp 1}$, and $V_{s\perp 2}$. Figure 2.8 shows the sample geometries, with denotations of measured velocities for waves propagating with different modes. In the case of the uniaxial test, the stress is incremented until the rock samples fail. The maximum pressure for the hydrostatic measurement is 70 MPa for all samples. However, only low stress (below 8 MPa for most samples) data are used for obtaining TOE constants of rocks under atmospheric pressure. The stress increments are as small as 0.3 MPa at the start

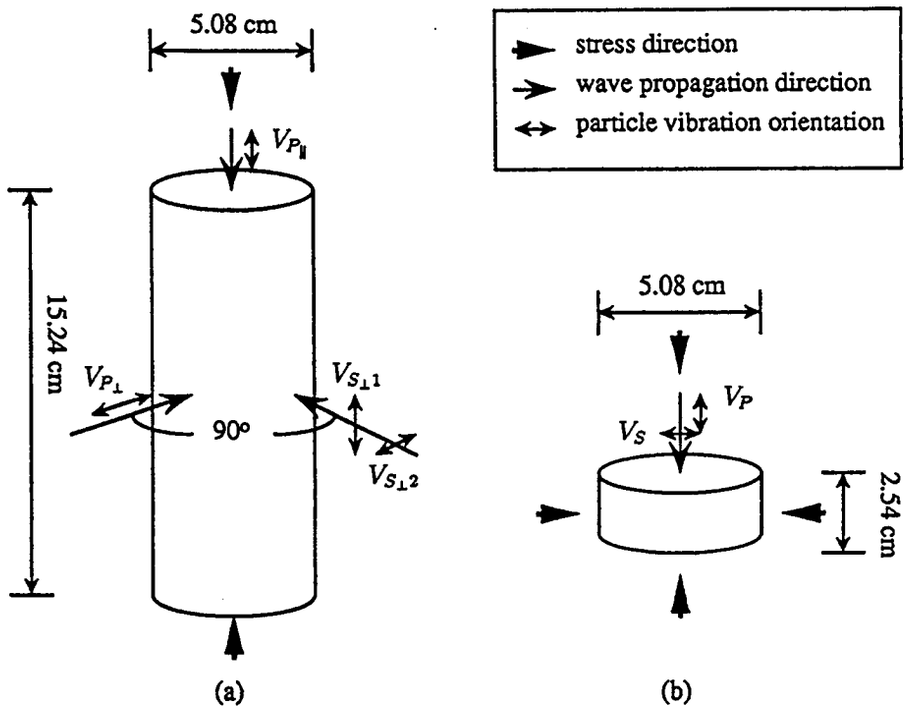

Figure 2.8: Sample geometry showing the notations for velocities of waves of different modes propagating along different directions under (a) uniaxial stress; and (b) hydrostatic stress

of loading to allow examination of the velocities at very low stresses. In an uniaxial test, the velocities of rocks can be strongly affected by sample geometry. However, as the ratio of sample diameter to length increases the effect becomes smaller. Based on suggestions by ASTM (American Society for Testing and Materials), the sample length and diameter chosen are 15.24 cm and 5.08 cm, respectively.[4]

Only the last three equations of ρV^2 in Table 2.2 are used to calculate TOE constants. l, m and n can be solved from the following equations:

$$\begin{aligned} \frac{2\mu}{\lambda+\mu}l - \frac{2\lambda}{\lambda+\mu}m &= C_{p\perp}E + 2\lambda\frac{\lambda+2\mu}{\lambda+\mu} \\ \frac{\mu}{\lambda+\mu}m + \frac{\lambda}{4(\lambda+\mu)}n &= C_{s\perp 1}E - \mu\frac{\lambda+2\mu}{\lambda+\mu} \\ \frac{\mu}{\lambda+\mu}m - \frac{1}{2}n &= C_{s\perp 2}E + \frac{2\lambda\mu}{\lambda+\mu} \end{aligned} \tag{2.7}$$

where λ, μ and E are all SOE constants calculated from measurements of sample

[4]For a more detailed description of experimental procedures, refer to Section 5.1.

sample	ρ (ρ/cm^3)	d (mm)	ϕ %	k mD	V_p (km/s)	V_s (km/s)	Failure (MPa)
Berea Ss	2.66	0.17	22.2	131	3.59	2.52	45
Buff Ss	2.70	0.07	16.0	1.2	4.21	2.72	54
Leuders Ls	2.20		19.8	0.5	4.44	2.58	50
Massillon Ss (#1066)	2.74	0.13	24.6	1.4 D	3.62	2.54	32
Massillon Ss (#1185)	2.65	0.20	21.0	2.5 D	4.14	2.93	44
Westerly Gr	2.67	0.75[a]			4.79	2.99	~ 240[b]

Table 2.3: Some petrophysical properties of rock samples used in this study. The abbreviations are: Ss - sandstone, Ls - limestone, and Gr - granite; ρ - grain density, $\bar{d}$ - average grain diameter, V_p, V_s - P- and S-wave velocities at 70 MPa; ϕ - porosity, k - permeability. Note: a - from Nur and Simmons (1969); b - from Gramberg (1989).

density and the unstressed velocities:

$$\mu = \rho V_s^2, \ \lambda = \rho V_p^2 - 2\mu, \text{ and } E = \mu \frac{3\lambda + 2\mu}{\lambda + \mu}$$

and $C_{p\perp}$, $C_{s\perp 1}$, and $C_{s\perp 2}$ are the slopes of $\rho V^2(T) - \rho V^2(0)$ plotted against stress T for $V_{p\perp}$, $V_{s\perp 1}$, and $V_{s\perp 2}$:

$$C = \frac{\rho V^2(T) - \rho V^2(0)}{T} \tag{2.8}$$

The errors in l, m, and n are prescribed by the errors in measuring V_p, V_s and ρ. If their errors are 1%, 2%, and 1%, respectively, the error is estimated to be 7% for m and n and 5% for l. The 3 to 5 % claim by Bakulin (1981) is overly optimistic, given the fact that the rocks in his experiment are very heterogeneous.

The internal consistency of the above systems of equations can be checked against the other three equations:

$$\begin{aligned} \frac{2\mu}{\lambda + \mu} l + 4m &= C_{p\|} E - (4\lambda + 10\mu + \frac{\lambda\mu}{\lambda + \mu}) \\ 2l + \frac{4}{3} m &= C_p K - (\frac{7}{3}\lambda + \frac{10}{3}\mu) \\ m - \frac{1}{6} n &= C_s K - (\lambda + 2\mu) \end{aligned} \tag{2.9}$$

where, similarly, $C_{p\|}$, C_p, and C_s are the slopes of $\rho V^2(T) - \rho V^2(0)$ plotted against stress T for $V_{p\|}$, and against hydrostatic pressure P for V_p, and V_s.

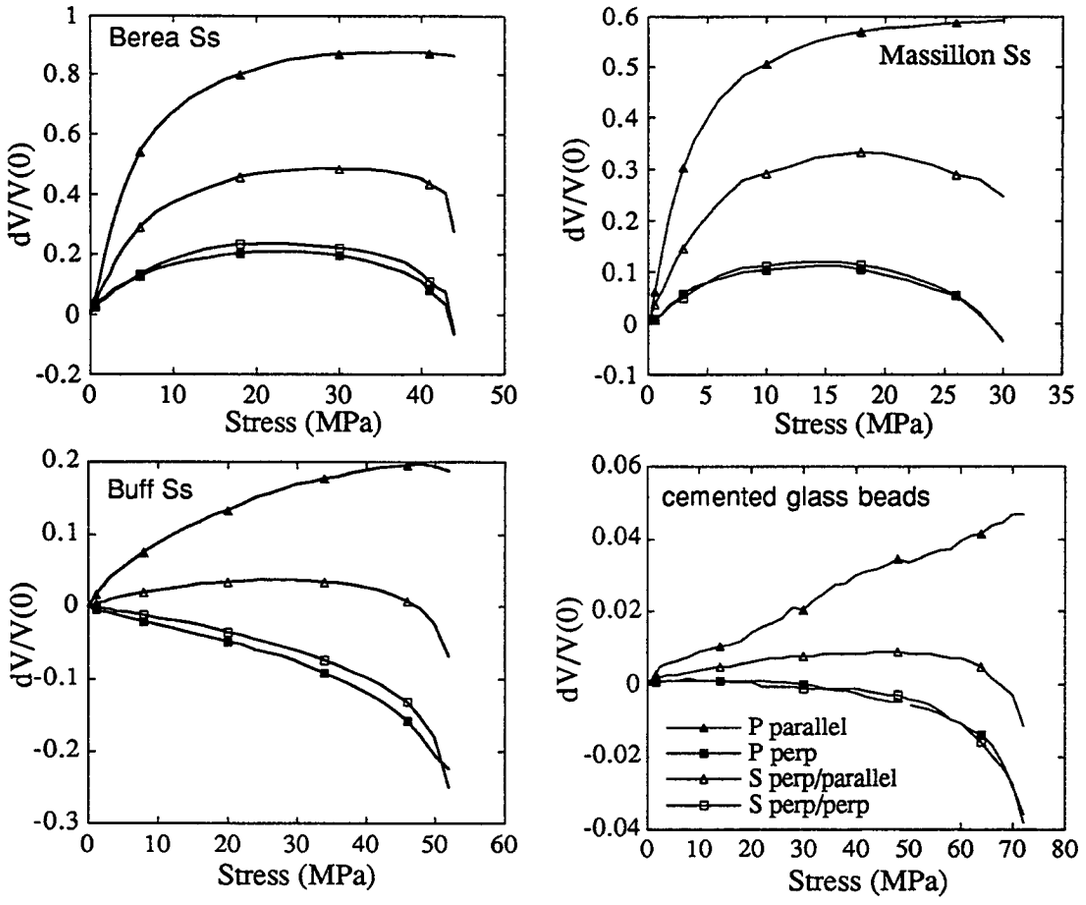

Figure 2.9: Relative changes in velocities along two orthogonal directions ($\parallel$ and $\perp$ to stress) of four samples: Berea Ss, Massillong Ss, Buff Ss, and cemented glass beads. The legend for S-wave velocities stands for propagation/polarization directions.

2.4.3 Measurement results

Figure 2.9 shows relative changes in velocities with uniaxial stress of four representative samples, Berea Ss, Massillon Ss, Buff Ss, and cemented glass beads. Note that in the plotting different scales are used for different rock samples. Two different behaviors can be seen among all samples. For Berea, Hanson and two Massillon sandstones, all velocities increase with uniaxial stress. For Buff sandstone, Leuders limestone and cemented glass beads, however, both V_p perpendicular to the direction of stress, and V_s propagating and polarizing perpendicular to stress decrease with stress. The textural explanation based on petrographical analysis relates the macroscopic velocity behavior of rocks to their microscopic grain contact properties, as discussed in Section 2.5. Table 2.4 lists the calculation results of TOE constants from this experiment using Equations 2.10. The order of magnitude of TOE constants is larger than those of SOE's in rocks because of the large variations of velocities with stress. Therefore,

sample	λ	μ	l	m	n	er($p_{\|\|}$)	er(p)	er(s)
Berea Ss	3.51	0.61	-1290	2180	-3680	140%	110%	240%
Buff Ss	9.07	3.73	3210	3650	-2810	270%	340%	360%
Leuders Ls	9.99	9.69	1610	1003	-624	520%	360%	220%
Massillon Ss (#1066)	4.01	1.15	-1266	2780	4320	150%	120%	220%
Massillon Ss (#1185)	6.36	1.02	-942	3340	-5400	150%	120%	170%
Westerly Gr	23.81	13.17	-7540	4310	-5540	120%	50%	162%

Table 2.4: Second- (λ, μ) and third-order (l, m and n) elastic constants of rock samples measured in this experiment. The unit is $GPa = 10^9 Pa$. The last three columns are prediction.

the second terms on the right hand side of the Equations 2.8 and 2.10 can be dropped.

The prediction errors in the last three columns are defined from Equations 2.8 as $|LHS - RHS| / |LHS|$, where LHS stands for the values of the left-hand side of Equations 2.10 using l, m, and n derived from Equations 2.8 and RHS stands for the values of the right-hand side using experimentally measured velocity slopes. The large errors obviously show inconsistency among equations in Table 2.2. This inconsistency may be, to a lesser extent, due to the deviation of actual stress in rock samples from uniaxial stress distribution (the uniaxial stress condition $V_{s||} = V_{s\perp 1}$ can not be verified since $V_{s||}$ is not measured). Another reason, however, may be the linear approximation used in deriving equations in Table 2.2. Murnaghan (1951) proposed a second-order approximation (p. 69) to the stress-strain relation that can extend the effective stress range of the relation. However, it may or may not significantly reduce the prediction errors. The individual TOE constants calculated from using linear and second-order relations may be significantly different, showing that only the combinations of TOE constants have direct physical meanings.

So far there has been no reliable data on TOE constants of rocks. Bakulin (1982) presented measurement results for some plutonic rock samples. However, a re-calculation using the velocity data given does not lead to the TOE constants he listed, not even SOE constants. No reasons were given to the approximations adopted when using equations in Hughes and Kelly (1953). In both Bakulin (1982) and Johnson et al. (1993), only TOE constants are presented and no error checking is made.

2.4.4 Predicting velocities under uniaxial stress

Is it possible to predict velocities under any states of stress from the hydrostatic measurement of velocities only? It is shown below that within the framework of second-order elasticity theory, the answer is positive. It depends, however, on the experimental observation made in this study. In the following, equations in Hughes and Kelly (1953) (though their correctness to rocks are yet to be studied) are used to illustrate how velocities under uniaxial state of stress can be related to P- and S-wave velocities measured under hydrostatic pressure.

It is observed for all samples except Westerly granite in this study that

$$\frac{V_{p\perp}^2(T) - V_{p\perp}^2(0)}{V_{p\perp}^2(0)} \approx \frac{V_{s\perp 2}^2(T) - V_{s\perp 2}^2(0)}{V_{s\perp 2}^2(0)}$$

which is equivalent to

$$\frac{V_{p\perp}^2(T)}{V_{s\perp 2}^2(T)} \approx \frac{V_{p\perp}^2(0)}{V_{s\perp 2}^2(0)} \approx \text{const.} \tag{2.10}$$

This is shown in Figure 2.10 for samples of Berea Ss, Massillon Ss, Buff Ss, and cemented glass beads. The uniaxial stress data of Nur et al. (1969a) on Barre granite supports this observation (Figure 2.11). It is therefore hypothesized that Equation 2.10 is true for most rocks. Under this hypothesis, the number of independent TOE constants can be reduced from 3 to 2 (see Appendix B). Since P- and S-wave velocities V_p and V_s measured under hydrostatic pressure P are two independent measurements, it is then possible to derive all three TOE constants from $V_p(P)$ and $V_s(P)$. Once all three TOE constants are known, velocities under any states of stress can be predicted, using equations in Table 2.2. For example, the slopes (see Equation 2.8 for definition) of velocities under uniaxial stress can be related to those of hydrostatic measurements by (see Appendix B for derivation)

$$\begin{aligned}
C_{p\parallel} &= \frac{\lambda C_p + 4(1+\frac{\lambda}{\mu})(\lambda+2\mu)C_s}{3\lambda+4\mu} \\
C_{s\parallel} &= \frac{-\mu C_p + (5\lambda+6\mu)C_s}{2(3\lambda+4\mu)} \\
C_{s\perp 1} &= C_{s\parallel} \\
C_{s\perp 2} &= \frac{\mu C_p - 2(\lambda+\mu)C_s}{3\lambda+4\mu} \\
C_{p\perp} &= \frac{\lambda+2\mu}{\mu} C_{s\perp 2}.
\end{aligned} \tag{2.11}$$

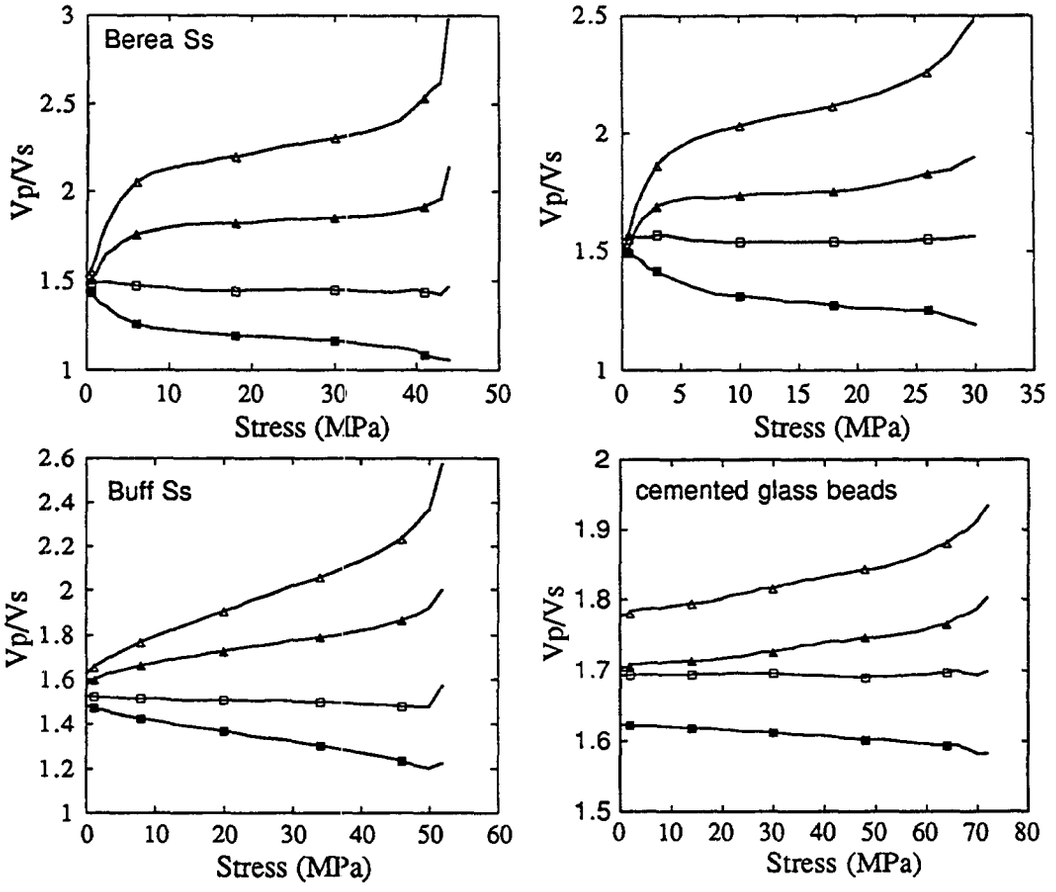

Figure 2.10: Various velocity ratios under uniaxial stress and hydrostatic pressure for four samples: Berea Ss, Massillon Ss, Buff Ss, and cemented glass beads.

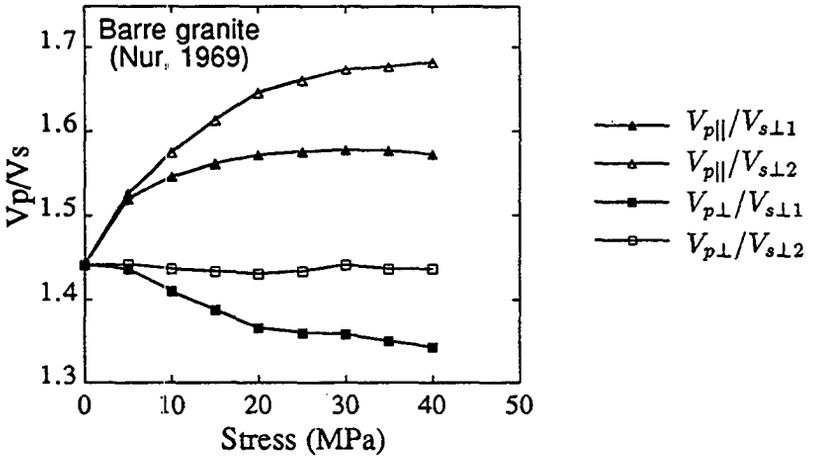

Figure 2.11: Velocity ratios measured in Barre granite under uniaxial stress (data from Nur et al., 1969a). Hollow symbols represent ratios of $V_{p||}$ to all V_s's and solid symbols represent ratios of $V_{p\perp}$ to all V_s's.

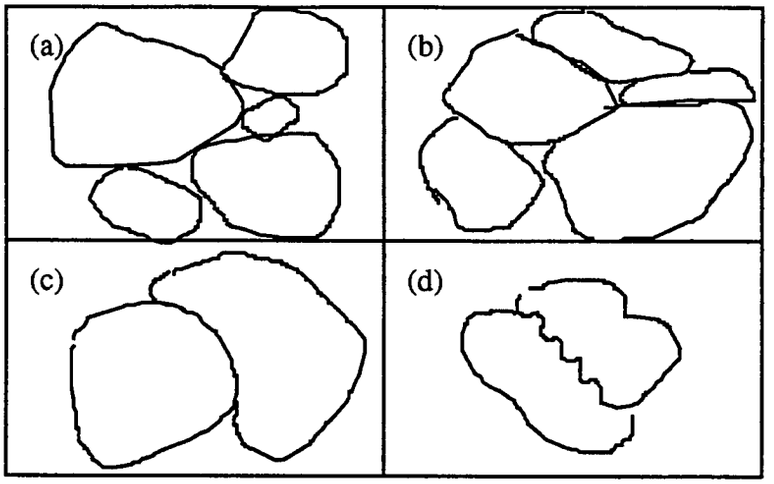

Figure 2.12: Four basic grain contact types in granular rocks: point (a), long (tangential) (b), concave-convex (c), and sutured (d).

2.5 Contact mechanics for sedimentary rocks

In sedimentary rocks, a wide range of grain-scale textures can be observed. For well-cemented noncracked rocks, little pressure dependence of elastic properties should be expected. However, due to pressure relief, heating, or action of large pressure, microcracks often exist at grain contact areas, causing rocks to become more compliant at low confining pressures. In shales, grains (if present) are widely separated and the elastic properties are expected to be dominated by the matrix of clay, silt, and other detritals. The scales of these microcrystalline particles are very small and are usually very porous. It is believed that grain rearrangement upon pressurization is important in shales. As a result of grain rearrangement, the pressure variation of elastic wave velocities is approximately linear and nontrivial even at high pressures. Between the two extreme cases (well-cemented sandstone and shale) are a variety of sand-clay mixtures (shaly sand or sandy shale), and the elastic properties of these mixtures depend clearly on grain contact properties.

Four basic contact types are often described in geology: point, long (tangential), concave-convex, and sutured (Figure 2.12). Mechanically, point contact is distinct from the other three types because of the large stress concentration at contact points (Johnson, 1985). This stress concentration can break grains or cause slippage along grain surfaces, inducing new microcracks. In both cases, stiffness is expected to

drop. This explains the velocity behavior of Buff sandstone. In the direction parallel to stress, the force between grains is mostly normal to contact, so that stiffness of the system increases with stress. In the orthogonal direction, no contact increase is expected; instead, slippage at point contacts causes a decrease in stiffness. Petrographically, this difference in velocity behaviors between Berea and Buff sandstones can be clearly related to clay content and clay/quartz grain texture. When clay content is below 17% (Jizba, 1991), quartz grains is the load-bearing frame and most grain contacts are long and concave-convex type. In this case, no easy slippage is expected and velocities in all directions increase with stress. When clay content is larger than 17%, clay begins to separate quartz grain and the point contact type occurs more often. After clay content exceeds about 40%, grains are well separated and most contacts are of point type. In these types of rocks, velocity in the direction normal to stress decreases.

Though stress concentration at point contacts is high, the stress variation of stiffness is not necessarily so. In fact, microcracks at long type contacts show the highest stress sensitivity, which gives high elastic nonlinearity. From the stress variation point of view, sutured contact is in between point and long contact and rocks containing mostly sutured contacts tend to have intermediate nonlinearity.

2.6 Conclusions

Because of the very low strain amplitudes in elastic wave propagations, second-order elasticity theory, in which strain terms up to third-order in the elastic energy are kept, is well suited for the study of nonlinear wave propagation/interaction. For the interaction of (dynamic) infinitesimal strain and (static) finite strain, however, the approximation adopted by Hughes and Kelly (1953) may be inadequate for rocks which are intrinsically highly nonlinear. More work, both experimental and theoretical, is needed to examine 1) the approximation of stress-strain relation in Hughes and Kelly (1953); 2) the approximation of second-order elasticity theory as applied to rocks; and 3) the uniaxial stress condition in the experiment.

With three more elastic constants (e.g., l, m, and n), velocities of wave propagations in homogeneously stressed isotropic solids can be expressed explicitly as functions of stress. The advantages of using macroscopic nonlinear theory over microscopic crack models are obvious since the three third-order elastic constants are more acceptable and easier to handle than parameters such as crack density, aspect

ratio, and crack distributions. Once all elastic constants for a material (5 for an isotropic solid) is known, it is possible to predict velocities under any states of stress, such as that around a borehole or near fault zones. Another advantage which was not explored in this work is that the relationship between static and dynamic elastic properties of rocks can now be studied quantitatively.

In granular sedimentary rocks, strength, (static) stiffness, and nonlinearity are closed related to each other. The contact mechanics applied to commonly observed grain contact types provides us with tools of anlysis to relate these important elastic properties of rocks, and find their textural origins.

Acknowledgements

Experiments for this study were carried out in Schlumberger-Doll Research Company (Ridgefield, Connecticut). The author acknowledges SDR for providing him with two summers of internship and for the use of all its facilities. He thanks Dr. Ken Winkler for all the advice and help. He also thanks Mr. Larry McGowen for his technical assistance, especially in sample preparation.

Appendix

A. Nonlinear wave equations for an isotropic solid

By incorporating third-order strain terms into the usual elastic strain energy for an isotropic solid (Landau, 1959, p.122)

$$\mathcal{E} = \mu\eta_{ik}^2 + \frac{\lambda}{2}\eta_{ll}^2 + \frac{A}{3}\eta_{ik}\eta_{il}\eta_{kl} + B\eta_{ik}^2\eta_{ll} + \frac{C}{3}\eta_{ll}^3 , \tag{2.12}$$

and using the complete form of the Lagrangian strain (Landuan, 1959, p.2)

$$\eta_{ik} = \frac{1}{2}\left(\frac{\partial u_i}{\partial x_k} + \frac{\partial u_k}{\partial x_i} + \frac{\partial u_l}{\partial x_i}\frac{\partial u_l}{\partial x_k}\right) , \tag{2.13}$$

Goldberg (1961) derived the most general wave equation (3-D) of second-order elasticity theory

$$\begin{aligned}
&\rho\frac{\partial^2 u_i}{\partial t^2} - \mu\frac{\partial^2 u_i}{\partial x_k \partial x_k} - (\lambda+\mu)\frac{\partial^2 u_l}{\partial x_l \partial x_i} = \\
&\quad (\mu + \frac{A}{4})(\frac{\partial^2 u_l}{\partial x_k \partial x_k}\frac{\partial u_l}{\partial x_i} + \frac{\partial^2 u_l}{\partial x_k \partial x_k}\frac{\partial u_i}{\partial x_l} + 2\frac{\partial^2 u_i}{\partial x_l \partial x_k}\frac{\partial u_l}{\partial x_k}) \\
&\quad +(\lambda + \mu + \frac{A}{4} + B)(\frac{\partial^2 u_l}{\partial x_i \partial x_k}\frac{\partial u_l}{\partial x_k} + \frac{\partial^2 u_k}{\partial x_l \partial x_k}\frac{\partial u_i}{\partial x_l}) + (\lambda + B)(\frac{\partial^2 u_i}{\partial x_k \partial x_k}\frac{\partial u_l}{\partial x_l}) \\
&\quad +(\frac{A}{4} + B)(\frac{\partial^2 u_k}{\partial x_l \partial x_k}\frac{\partial u_l}{\partial x_i} + \frac{\partial^2 u_l}{\partial x_i \partial x_k}\frac{\partial u_k}{\partial x_l}) + (B + 2C)(\frac{\partial^2 u_k}{\partial x_i \partial x_k}\frac{\partial u_l}{\partial x_l}),
\end{aligned}$$

where ρ is the density, λ and μ are second-order Lamé constants, and A, B, C are third-order elastic constants (the two sets of TOE constants A, B, and C and l, m, and n are related by $A = n$, $B = m - \frac{1}{2}n$, and $C = l - m + \frac{1}{2}n$). Sometimes, Equation 2.12 is called the "physical" and, Equation 2.13, the "geometrical" cause of nonlinearity.

In 1-D case (x taken as the direction of wave propagation), the above equation can be simplied to

$$\begin{aligned}
\rho\frac{\partial^2 u_x}{\partial t^2} - \alpha\frac{\partial^2 u_x}{\partial x^2} &= \beta\frac{\partial^2 u_x}{\partial x^2}\frac{\partial u_x}{\partial x} + \gamma(\frac{\partial^2 u_y}{\partial x^2}\frac{\partial u_y}{\partial x} + \frac{\partial^2 u_z}{\partial x^2}\frac{\partial u_z}{\partial x}) \\
\rho\frac{\partial^2 u_y}{\partial t^2} - \mu\frac{\partial^2 u_y}{\partial x^2} &= \gamma(\frac{\partial^2 u_y}{\partial x^2}\frac{\partial u_x}{\partial x} + \frac{\partial^2 u_x}{\partial x^2}\frac{\partial u_y}{\partial x}) \\
\rho\frac{\partial^2 u_z}{\partial t^2} - \mu\frac{\partial^2 u_z}{\partial x^2} &= \gamma(\frac{\partial^2 u_z}{\partial x^2}\frac{\partial u_x}{\partial x} + \frac{\partial^2 u_x}{\partial x^2}\frac{\partial u_z}{\partial x})
\end{aligned}$$

where $\alpha = \lambda + 2\mu$, $\beta = 3\alpha + 2A + 6B + 2C$, and $\gamma = \alpha + \frac{A}{2} + B$.

B. Relations between velocities under uniaxial and hydrostatic stresses

In an initially isotropic medium, it is observed that when waves propagate in the plane perpendicular to the direction of a uniaxial stress (i.e., both propagation and polarization directions are perpendicular to that of stress):

$$\frac{V_p^2(T)}{V_s^2(T)} \approx \frac{V_p^2(0)}{V_s^2(0)},$$

where T is the stress magnitude. Using Equations (12) in Hughes et al. (1953), the above experimental observation can lead to the following relation among third-order elastic constants l, m, and n ($\approx$ be replaced by $=$):

$$2\mu^2 l - \mu(3\lambda + 2\mu)m + \frac{1}{2}(\lambda + \mu)(\lambda + 2\mu)n = 0$$

Together with the two equations for hydrostatic velocities V_p and V_s, l, m, and n can be solved and expressed in C_p and C_s (definitions of C's are given in Section 2.4):

$$\begin{aligned} l &= \frac{\frac{1}{2}(3\lambda^2 + 6\lambda\mu + 4\mu^2)C_p - 2(\lambda + \mu)(\lambda + 2\mu)C_s}{3\lambda + 4\mu} \\ m &= \frac{-\mu^2 C_p + 3(\lambda + \mu)(\lambda + 2\mu)C_s}{3\lambda + 4\mu} \\ n &= \frac{-6\mu^2 C_p + 2\mu(9\lambda + 10\mu)C_s}{3\lambda + 4\mu} \end{aligned}$$

Once l, m, and n are known, velocities under any states of stress can be predicted. In the case of a uniaxial stress, the velocities under uniaxial and hydrostatic conditions can be related, in the form of their slopes of variation with stresses through

$$\begin{aligned} C_{p\parallel} &= \frac{\lambda C_p + 4(1 + \frac{\lambda}{\mu})(\lambda + 2\mu)C_s}{3\lambda + 4\mu} \\ C_{s\parallel} &= \frac{-\mu C_p + (5\lambda + 6\mu)C_s}{2(3\lambda + 4\mu)} \\ C_{s\perp 1} &= C_{s\parallel} \\ C_{s\perp 2} &= \frac{\mu C_p - 2(\lambda + \mu)C_s}{3\lambda + 4\mu} \\ C_{p\perp} &= \frac{\lambda + 2\mu}{\mu} C_{s\perp 2}. \end{aligned}$$

In the indices, $\parallel$ or $\perp$ stands for the direction of wave propagation that is parallel or perpendicular to that of stress; 1 or 2 stands for the polarization direction that is parallel or perpendicular to that of stress.

Using Poisson's ratio, the above equations can also be expressed as

$$\begin{aligned} C_{p\|} &= \frac{\nu C_p + 4\frac{1-\nu}{1-2\nu}C_s}{2-\nu} \\ C_{s\|} &= \frac{-(1-2\nu)C_p + 2(3-\nu)C_s}{4(2-\nu)} \\ C_{s\perp 1} &= C_{s\|} \\ C_{s\perp 2} &= \frac{(1-2\nu)C_p - 2C_s}{2(2-\nu)} \\ C_{p\perp} &= \frac{1-\nu}{\nu}C_{s\perp 2} \end{aligned}$$

When calculating velocities from slopes, note that C_p and C_s as well as λ, μ, or ν are functions of confining pressure. Since λ and μ are both nonnegative, we have $C_{p\|} > 0$ always. In most materials, $C_{s\|} > 0$ (as long as $\frac{C_p}{C_s} \leq \frac{2(3-\nu)}{1-2\nu}$). However, $C_{p\perp}$ and $C_{s\perp 2}$ can be negative. The simple relationship between $C_{s\perp 2}$ and $C_{p\perp}$ comes from the experimental observation. Finally, whether $C_{s\perp 1} = C_{s\|}$ or not can be used to test the uniaxial stress condition.

References

Bakulin, V. N. and A. G. Protosenya, 1982, Nonlinear effects in travel of elastic waves through rocks, Doklady of the Academy Sciences of the USSR, **263**, 3-5.

Bonner, B. P., 1974, Shear wave birefringence in dilating granite, Geophys. Res. Letts., **1**, 217-220.

Bourbie, T., O. Coussy, and B. Zinszner, 1987, Acoustics of porous media, Gulf Pub. Co., Houston, Texas.

Breazeale, M.A. and J. Philip, 1984, Determination of third-order elastic constants from ultrasonic harmonic generation measurements, in Physical Acoustics, XVII, ed. by W. P. Mason.

Carmichael, R. S., 1981, Handbook of physical properties of rocks, C.R.C. press.

Dunham, R. W. and H. B. Huntington, 1970, Ultrasonic beam mixing as a measure of the nonlinear parameters of fused silica and single-crystal NaCl, Phys. Rev. B, **2**, 1,098-1,107.

Dvorkin, J., G. Mavko and A. Nur, 1991, The effect of cementation on the elastic properties of granular materials, Mechan. of Materials, **12**, 207-217.

Fung, Y. C., 1965, Foundations of solid mechanics, Englewood Cliffs, N.J., Prentice-Hall.

Gol'dberg, Z. A., 1961, Interaction of plane longitudinal and transverse elastic waves, Soviet Physics: Acoustics, **6**, 306-310.

Gramberg, J., 1989, A non-conventional view on rock mechanics and fracture mechanics, A. a. Balkema Publishers.

Green, Jr., R. E., 1973, Ultrasonic inverstigation of mechanical properties, in Treatise on materials science and technology, **3**, Academic Press, New York.

Gupta, I. N., 1973, Seismic velocities in rock subjected to axial loading up to shear fracture, J. Geophys. Res., **78**, 6936-6942.

Hughes, D. S., and I. I. Kelly, 1953, Second-order elastic deformation of solids, Phys. Rev., **92**, 1,145-1,149.

Jizba, D., 1991, Mechanical and acoustical properties of sandstones and shales, Ph.D. thesis, Stanford University.

Johnson, K. L., 1985, Contact mechanics, Cambridge University Press.

Johnson, P. A., T. J. Shankland, R. J. O'Connell, and J. N. Albright, 1987, Nonlinear generation of elastic waves in crystalline rock, J. Geophys. Res., **92**, 3,597-3,602.

Johnson, P. A. and T. J. Shankland, 1989, Nonlinear generation of elastic waves in granite and sandstone, J. Geophys. Res., **94**, 17,729-17,733.

Jones, G. L. and D. R. Kobett, 1963, Interaction of elastic waves in an isotropic solid, J. Acoust. Soc. Am., **35**, 5-10.

Lockner, D. A., J. B. Walsh, and J. D. Byerlee, 1977, Changes in seismic velocity and attenuation during deformation of granite, **82**, 5374-5378.

McCall, K. R., 1994, Theoretical study of nonlinear elastic wave propagation, J. Geophys. Res., in press.

Lamb, H., 1931, The dynamical theory of sound, 2d ed. London, E. Arnold & Co.

Landau, L. d. and E. M. Lifshitz, 1959, Theory of elasticity, Pergamon Press, Inc., New York.

Murnaghan, F. D., 1951, Finite deformation of an elastic solid, John Wiley & Sons, Inc., New York.

Nur, A. and G. Simmons, 1969a, Stress-induced velocity anisotropy in rocks: an experimental study, J. Geophys. Res., **74**, 6667-6674.

Nur, A. and G. Simmons, 1969b, The effect of saturation on velocity in low porosity rocks, Earth Planetary Sci. Let., **7**, 183-193.

Sayers, C. M., 1988, Inversion of ultrasonic wave velocity measurements to obtain the microcrack orientation distribution function in rocks, Ultrasonics, **26**, 73-77.

Sayers, C. M., 1990, Stress-induced ultrasonic anisotropy in Berea sandstone, Int. J. Rock Mech. Min. Sci. & Geomech. Abst., **27**, 429-436.

Taylor, L. H. and F. R. Rollins, Jr., 1964, Ultrasonic study of three-phonon interaction, Phys. Rev., **136**, A591.

Thurston, R. N., and K. Brugger, 1964, Third-order elastic constants and the velocity of small amplitude elastic waves in homogeneously stressed media, Phys. Rev., **133**, 6A, 1,604-1,610.

Toupin, R. A., and B. Bernstein, 1961, Sound waves in deformed perfectly elastic materials: Acoustoelastic effect, J. Acoust. Soc. Am., **33**, 216-225.

Walsh, J. B., 1965, The effects of cracks on the compressibility of rocks, J. Geophys. Res., **70**, 381-389.

Winkler, K. W., and T. J. Plona, 1982, Technique for measuring ultrasonic velocity and attenuation spectra in rocks under pressure, J. Geophys. Res., **87**, 10,776-10,780.

Zimmerman, R. W., 1991, Compressibility of sandstones, Developments in Petroleum Science, **29**, Elservier, Amsterdam.

Chapter 3

Seismic anisotropy of shales

Abstract

Based on laboratory measurements of shales from several well-known formations, the effects of mineralogy, kerogen content, structure, texture, porosity, and saturating fluids on seismic velocity and elastic anisotropy of kerogen-rich shales are studied. The seismic velocity is determined mainly by mineralogy, kerogen content, and porosity, but strongly affected by confining pressure, fluid saturation, as well as wave propagation direction. Mineralogy and texture are intrinsic factors that affect elastic anisotropy. Textures of kerogen-rich shales can be modeled by one or a mixture of 1) the preferred orientation of clay particles; 2) the micro-lamination of low density kerogen-clay mixture with calcareous, siliceous, or phosphatic materials, and sometimes with highly concentrated kerogen; and 3) the preferred alignment of lenticularly shaped kerogen-clay mixture in the anisotropic background of the same material but with lower kerogen concentration. Bedding-parallel microcracks, generated during either kerogen maturation or sample preparation, can greatly enhance the anisotropy. A numerical experiment by Monte Carlo simulation shows that, unlike isotropic media, the normal stiffnesses of a TI medium may decrease upon saturation. In water-saturated, low porosity shales, it is found that clay softening can significantly reduce S-wave velocities in all directions and P-wave velocity along bedding-parallel direction. This weakening effect should exist in all shaly rocks. As far as fluid flow-induced velocity dispersion is concerned, frequency correction may not be needed when applying laboratory ultrasonic measurements to sonic interpretations. This is concluded from the analysis of transition frequency in shales and the comparison between laboratory ultrasonic and field sonic measurements.

3.1 Introduction

In order to obtain the petrophysical (porosity, permeability) and geochemical (kerogen content, hydrocarbon maturity) properties of source rocks from seismic measurements, it is imperative for us to understand how elastic properties of shales can be affected by their mineralogy, kerogen content, structure, texture, porosity, and saturating fluids. Equally important to know is how in-situ sonic or seismic responses can be correlated with laboratory measurements, considering the big gap between the two in terms of measurement frequency and scale.

Large scale seismic and some geochemical properties of shales have been studied using surface seismic (Banik, 1984; Seriff, 1985; Roy, 1988), cross-well seismic (Winterstein and Paulsson, 1990), VSP, and well logging (Passey *el. al.*, 1990) methods. Early laboratory measurements on elastic properties of shales or shaly rocks include those by Kaarsberg (1976), Morris (1978), Jones et al. (1981), Tosaya (1982), and Johnston (1987). Vernik et al. (1992) first reported in detail the strong anisotropy caused by kerogen micro-laminated with clay particles. Recently, the effects of microcracks generated by hydrocarbon maturation (Vernik, 1993), the modeling of anisotropy, and velocity-porosity transformation (Vernik et al., 1994) were investigated. However, more work is needed 1) to generalize the study to other formations; 2) to propose a physical model for the observed textural features of kerogen-rich shales; 3) to understand the effects of saturating fluids on elastic properties of shales; and 4) to apply laboratory studies to field measurements such as sonic logging. The previous studies (e.g., Vernik et al., 1992) have emphasized the role of kerogen but overlooked factors like mineralogy and texture. Besides, the preliminary model based on Backus average (Backus, 1962) cannot explain all experimental data. A simple physical model based on which modeling can be made is therefore needed. For the effect of fluid saturation, Gassman (1951) equation states that bulk modulus always increases upon saturation. It is not clear, however, whether the conclusion is also true for anisotropic rocks. As for velocity dispersion caused by fluid flow, two mechanisms have been proposed. The Biot flow (Biot, 1956) mechanism considers fluid-solid mass coupling due to inertia and viscous effects in fluids. The other one, called local flow mechanism, deals with the local stiffening of pore space by unrelaxed fluids (Mavko et al., 1975 and O'Connell et al., 1977). Since both mechanisms are frequency-dependent, dispersion correction on velocity may be needed when going from high frequency range (such as ultrasonic) to low frequency range (such as borehole sonic). For shales, however, the necessity for such a correction need to be investigated.

In this chapter, I use laboratory measurements on a world-wide collection of shale samples to study how seismic velocity and anisotropy of kerogen-rich shales can be affected by mineralogy, kerogen content, porosity, textures (micro-lamination, micro-cracks, kerogen distribution), and fluid saturation. A physical model for the texture of shales and a modeling scheme for their elastic properties are proposed to account for the above effects. Two aspects of fluid-saturation effects are studied: (1) fluid flow-induced velocity dispersion; and (2) mechanical (static) stiffening and physical or chemical weakening. At the end, a detailed study is presented on the ultrasonic and sonic properties of shales from the Monterey formation, demonstating the use of rock physics study to locating oil reservoirs.

3.2 Velocity and elastic anisotropy of shales

Analysis of experimental measurements and modeling with known theories are the methodologies used for relating elastic properties of shales to their petrophysical and petrochemical properties. In this section, shale samples, experimental methods, and measurement results are described first. Then, analysis and modeling that are based on experimental observations are made of the effects of mineralogy, kerogen content, porosity, and texture on the seismic velocity and elastic anisotropy of kerogen-rich shales. The analysis draws petrographical evidence from the thin section analysis of shales. A study of the effects of saturating fluids is given in the next section.

3.2.1 Laboratory measurements

Sample collection and the shale database

Shale samples for this study are collected from several well-known formations around the world. These formations are the Bakken from North Dakota and Montana (US), the Niobrara from New Mexico (US), the Monterey from California (US), the Lockatang from New Jersy (US), the Woodford from Oklahoma (US), the Kimmeridge from the North Sea, and the Bazhenov from western Siberia (Russia). These samples cover a very wide range of mineral composition, kerogen content (see Figure 3.1 for histograms of the mineral compositions from XRD mineralogy and TOC from Rock-Eval measurements), porosity, and texture features, and therefore provide an unprecedented collection, in terms of its sample size and the variety of petrophysical/petrochemical properties measured, for a detailed study of the elastic properties of kerogen-rich shales.

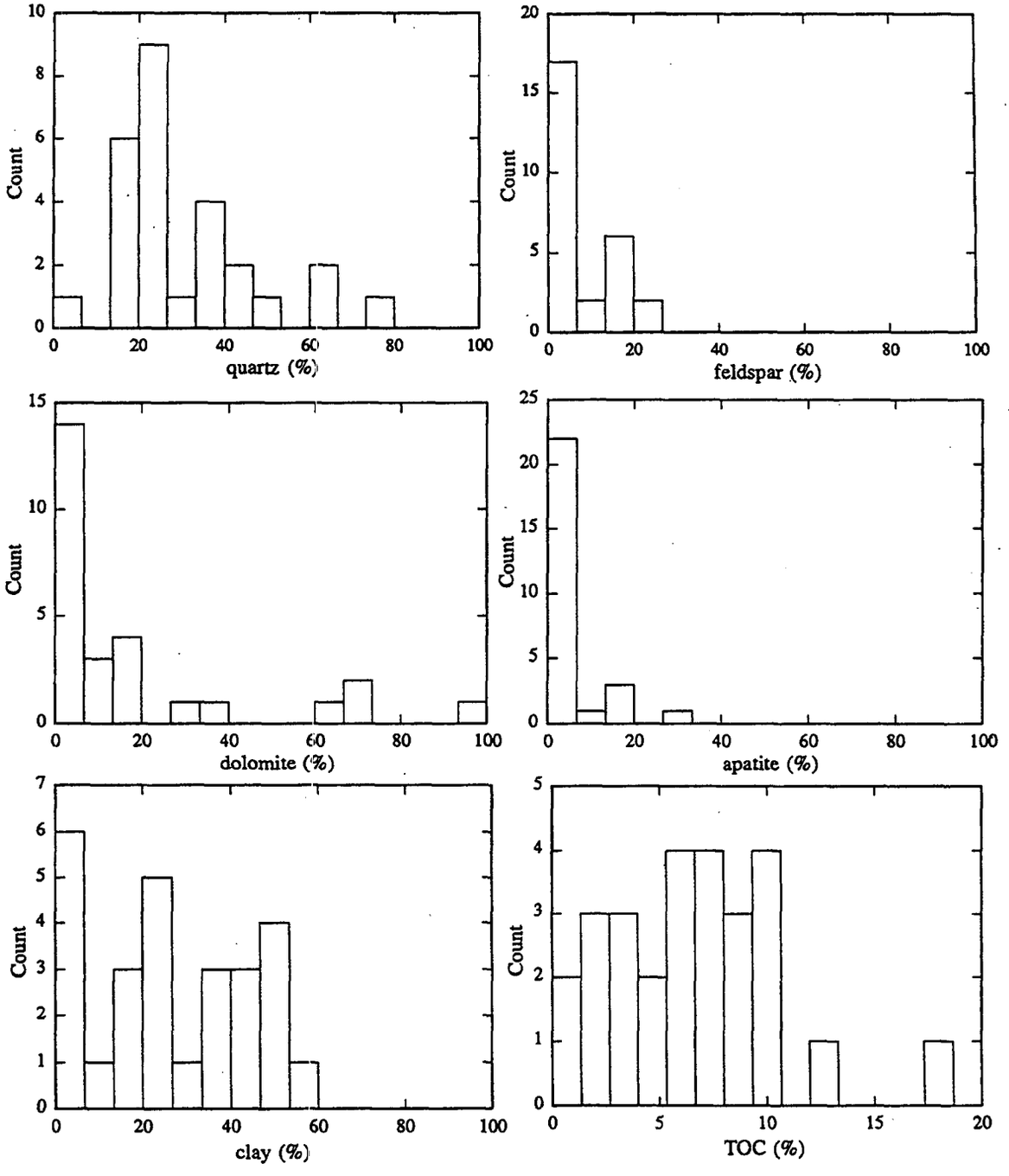

Figure 3.1: Histograms of the mineral distributions from XRD mineralogy analysis and the TOC content from Rock-Eval collectively of shale samples from the Bakken, Bazhenov, and Monterey formations. Vertical axis is the sample count.

Elastic symmetry of shales

A premise in almost all experimental studies of shales is that the symmetry of elastic properties of shales is hexagonal (or transverse isotropic (TI)), with the symmetry axis being normal to the lamination or bedding plane. Therefore, five independent elastic constants are needed to fully characterize the elastic properties. There are exceptions, however. Some highly siliceous samples from the Monterey formation contain two sets of near orthogonal fractures (sealed) that are perpendicular to the bedding-plane. These samples are believed to be orthorhombic in symmetry and have nine elastic constants. For TI samples, three directions are commonly chosen for measurements of five velocities required to derive all five elastic constants: normal, parallel, and 45° to the bedding. This is achieved by cutting three plugs along the three orientations out of the same core (see Section 2 of Chapter 5).

Experimental methods

Ultrasonic P- and S-wave velocities, density, porosity, and permeability are measured on cylindrical samples of 20 to 25 mm in diameter and 22 to 30 mm in length. Standard ultrasonic transmission technique is used to measure velocities. Velocity values are calculated from the measured transmission times of a broadband signal and the sample lengths. The central frequencies of the transducer's vibrating element (PZT) are close to 1 MHz. The received signals, however, have a much lower peak frequency because of attenuation, from 300 to 800 kHz. With the mosaic transducer design, it is possible to measure three velocities at a time: one longitudinal (P) and two orthorgonally-polarized shear waves (S_1 and S_2). Figure 3.2 shows sample orientations and the mosaic transducer design. The overall accuracy for measured V_p is 1% and for V_s is 2%. Densities (accurate to 0.01 g/cm^3) measured from all three plugs serve as a check to the sample homogeneity to ensure valid measurements of anisotropy. Porosity is measured from weight difference caused by water saturation and checked by Helium porosimeter. Fluid (water) permeability is measured on only a few, selected, high porosity Monterey outcrop samples. The measurement is taken at 10 MPa confining pressure to eliminate any bias caused by possible cracks. The criteria for sample homogeneity is that a core with a density/porosity variation more than 3% among the three plugs has to be eliminated.

Before measurements are taken, samples are oven-dried at 110 $°C$ and then allowed to cool down to room temperature in a desiccator. All velocity measurements are taken at room temperature in a pressure vessel filled with silicone oil (dimethylpolysiloxane, viscosity 5 centi-stokes at 20 $°C$) used as pressure fluid. Samples are jacked

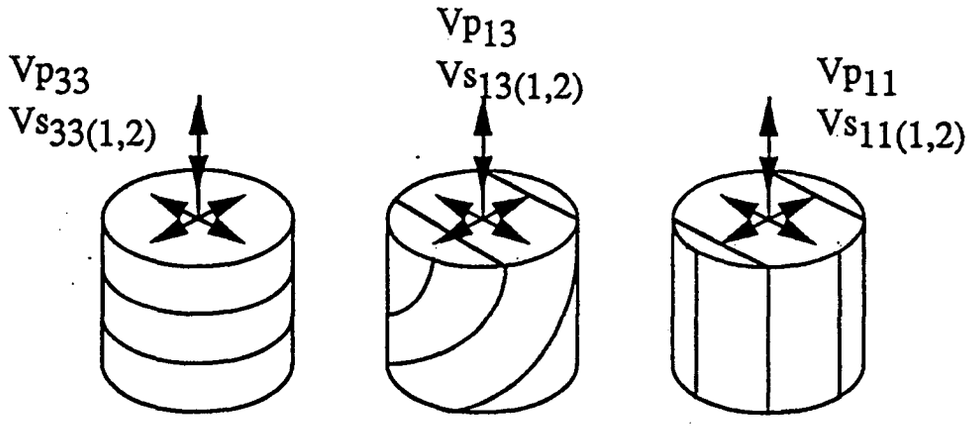

Figure 3.2: A schematic plot showing core orientations relative to bedding direction and the measured velocities of P- and S-waves.

by tygon tubing. During pressuring, the pore pipe is vented to atmosphere and, therefore, the effective pressure equals the confining pressure. Pressure levels are started at 2, 5, 10, 20, ..., MPa and ended at 40 MPa for the Monterey samples and 90 MPa for the Niobrara samples. For saturation measurements, the sample is saturated with brine (5% weight concentration) to prevent the clay from swelling.

Measurement results

Measurement results on the petrophysical/chemical properties of shales include porosity, permeability, density, TOC content, and velocities of P-, SH-, and SV-waves along three different directions: parallel, perpendicular, and 45° to the symmetry axis). Velocity measurements are made at both dry and saturated conditions. In Section 5.2, only the Monterey (outcrop and subsurface) and Niobrara formation data are listed. Elastic constants and anisotropy parameters can be derived from velocities. However, the results are not included in this dissertation. Definitions of stiffness matrix, five independent elastic constants, and anisotropy parameters are given in Appendix A. Also given are their relationships to body wave velocities that can be measured experimentally. For details of the elastic description of solids, refer to Auld (1990).

For the purpose of discussions in the following sections, the elastic constants C_{33}, C_{11}, C_{44}, C_{66}, and anisotropy parameters ϵ and γ (Thomsen, 1986) of the Monterey formation shale samples are plotted, as seen in Figure 3.3 and Figure 3.4).

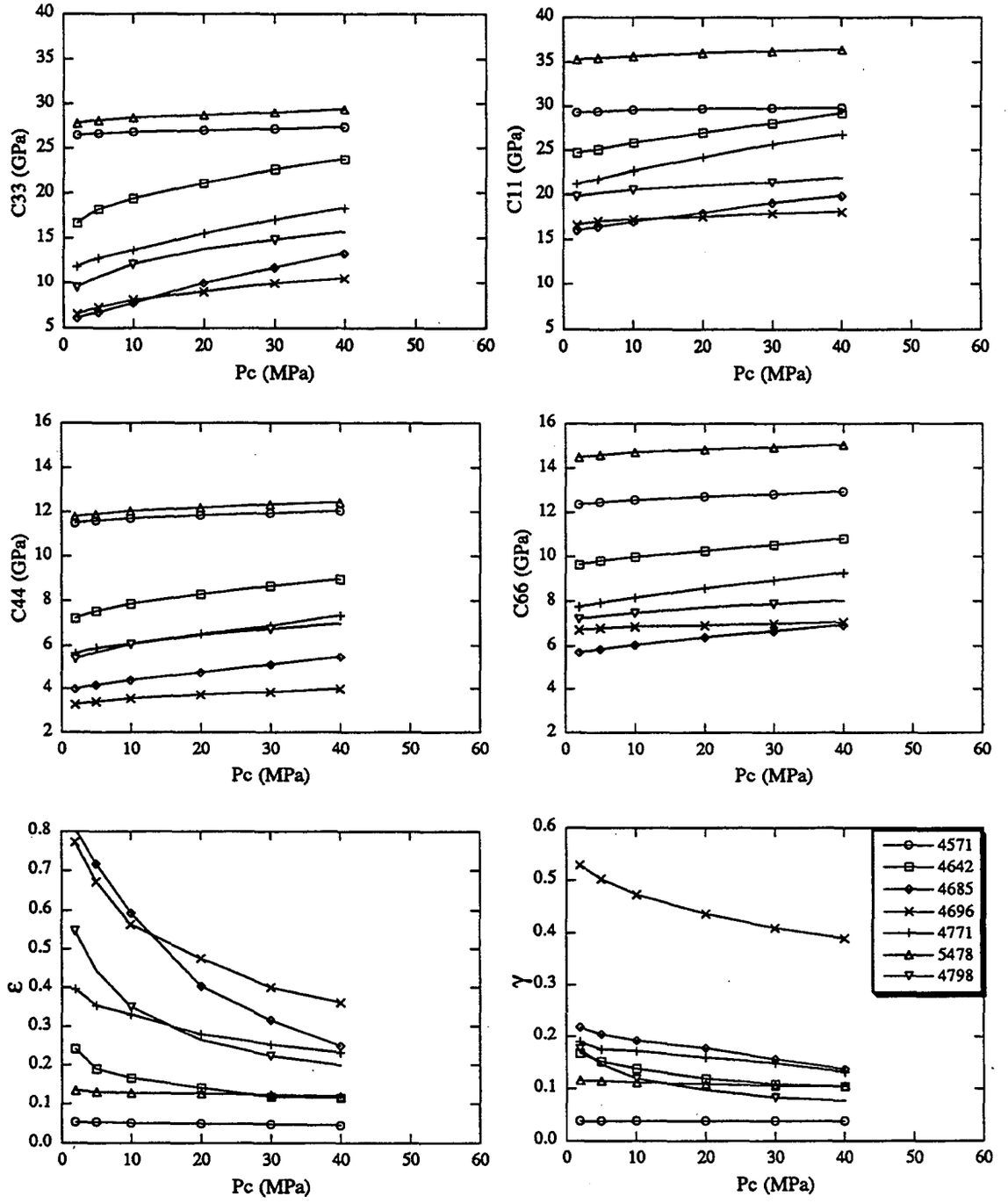

Figure 3.3: Measured elastic constants C_{33}, C_{11}, C_{44} and C_{66} and anisotropy parameters ϵ and γ (dry) of the Monterey shales: subsurface samples. 1 GPa=10^9 Pa.

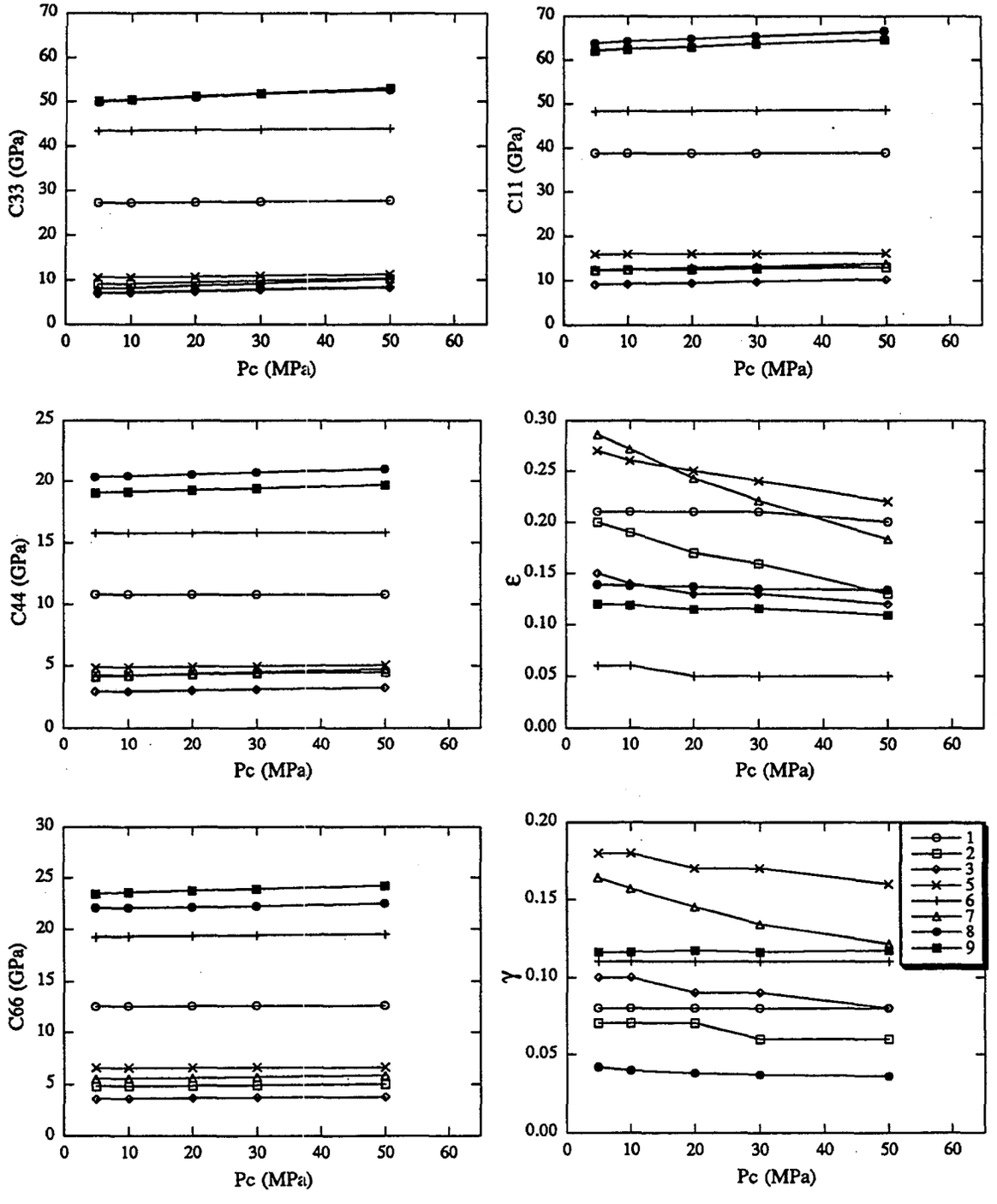

Figure 3.4: Measured elastic constants C_{33}, C_{11}, C_{44} and C_{66} and anisotropy parameters ϵ and γ (dry) of the Monterey shales: outcrop samples. 1 GPa = 10^9 Pa.

3.2.2 Effects of mineralogy, kerogen content, and porosity

There are two reasons for studying the average properties of shales. First, the velocity-porosity-kerogen content relationships are of great interest and two of the parameters in the relationship, porosity and kerogen content, are the average properties of shales. Second, in most samples, the difference in elastic constants along any two different directions is much smaller than the average. Therefore, when the effect of mineralogy is concerned, elastic properties along different directions can be averaged.

Effect of mineralogy and kerogen content

The basic mineral compositions of shales in our collection are dolomite, calcite, feldspar, quartz, Opal-CT (silica), clay, and apatite. Since some minerals have similar elastic properties, they can be grouped together for modeling purposes. Using the mineral properties (density and velocities), V_p and V_s of the composite mineral matrix can be predicted using effective medium theory.

To illustrate this, Figure 3.5 shows the calculated matrix velocities (in contours) from the Hashin-Shtrikman averages (Hashin and Shtrikman, 1963, see Appendix of Chapter 4 for equations used in this calculation) for different volumetric combinations of dolomite, kerogen-rich detritus (K-SHALE), and biogenic silica. The velocities (V_p and V_s) and density of one of the end-members, kerogen-rich detritus, are averaged from velocities of high-rank coal (V_p = 2.8, V_s = 1.6, ρ = 1.25, Yu et al., 1993, Vernik et al., 1994) and quartz, assuming 35% kerogen content, using Voigt-Reuss-Hill average (Hill, 1952). Velocities for the three end-members are shown in Table 3.1. In the figure, Hashin-Shtrikman averages are the upper and lower bounds shown in dashed lines. The solid lines are the average of the two bounds. The effect of mineralogy is shown to be very strong as determined by the extremity of the elastic properties of kerogen (represented by high-rank coal) and dolomite. This effect should exceed any directional dependence caused by the micro-lamination of shale and kerogen-clay mixture.

Even the pressure-dependence of velocities depends on mineralogy. In both sub-surface and outcrop Monterey samples, it is noticed that elastic constants of shaly dolomites display larger pressure variations. The fact that C_{11} and C_{33} have similar behaviors shows that it is not caused by bedding-parallel microcracks such as that in the larger C_{33} variation of samples 4696 and 4798 (phosphatic shale), but by matrix properties, explanable by . by the textural differences between high and low dolomite samples (Figure 3.6). When grains are in contact (high content for the grain mineral), pressure can increase grain contact areas, therefore increasing the stiffness of

components	density g/cm^3	V_p km/s	V_s km/s	source
end-member rocks				
dolomite	2.86	7.0	4.0	(Ch 4, this study)
silica	2.30	5.5	3.45	(average of opal-CT and qtz)
kerogen-shale (30% kerogen)	2.13	4.3	3.0	(average of coal and shale)
rock-forming minerals and kerogen (coal)				
quartz	2.65	6.05	4.09	(CRC Handbook)
dolomite	2.87	7.00	4.10	(Ch 4, this study)
calcite	2.71	6.72	3.49	(Birch, 1962)
coal	1.25	2.80	1.60	(Yu et al., 1993)

Table 3.1: Velocities and densities of the three end-member rocks as well as the minerals used in modeling the matrix velocity by Hashin-Shtrikman averages. The average density of quartz (2.64 g/cm^3) and opal-CT (1.89 g/cm^3) is used for silica.

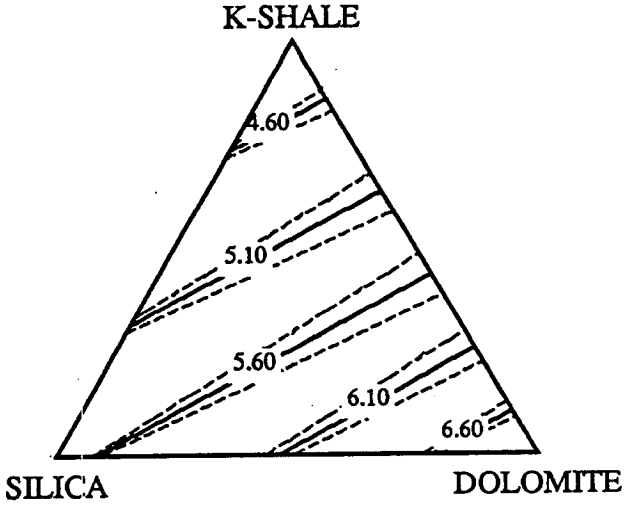

Figure 3.5: The average matrix velocities of P-waves as predicted from Hashin-Shtrikman equations for rocks formed of three end-members: kerogen-rich detritus, silica, and dolomite.

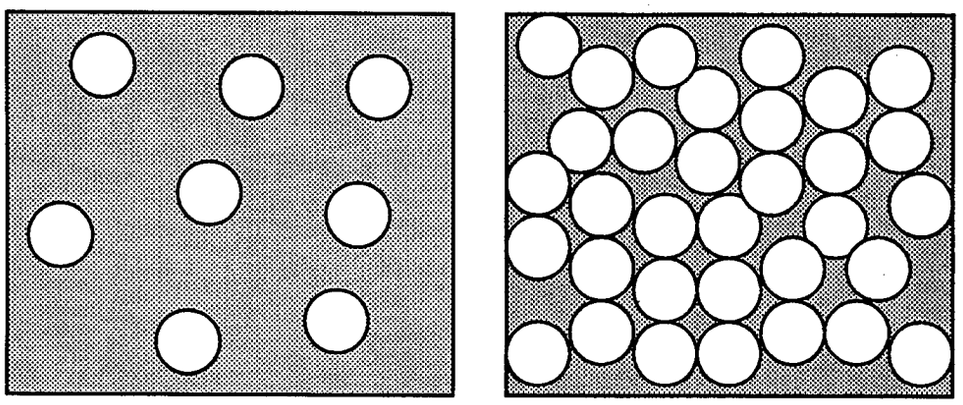

Figure 3.6: A schematic diagram showing the textural difference between high and low contents of mineral grains. The petrographic evidence can be found from thin section photomicrographs.

the rock as a whole. In shales, however, elastically stiffer grains are widely separated. Any pressure variation originates from the matrix itself which shows the typical linear increase with pressure.

Effect of porosity

Pores decrease the elastic stiffnesses and therefore the velocities of a porous medium. However, the slope of variation depends on the mineral properties, as hinted by critical porosity concept (Nur, 1991) and supported by measurement data (Figure 3.7). The higher the mineral matrix velocity, the larger is the slope and vice versa. Besides, it is seen that the scattered trends converse at around 40 % of porosity.

3.2.3 Direction-dependent properties - effect of texture

Three basic textures are responsible for the elastic anisotropy of shales: preferred grain (mainly clay particles) orientation (micron scale); preferred alignment of lenticular kerogen-clay mixture; and the micro lamination of kerogen-clay mixture, thin kerogen layer, and siliceous, phosphatic, or calcareous material. The first type, preferred clay orientation, gives the anisotropy of shales composed completely of clay and kerogen that are both homogeneously distributed. An example of this type is given in Figure 3.8 (c). The third type, micro-lamination, is observed mostly in the Monterey samples (sample 4560, 4571, and 5, as shown by Figure 3.8 (d)). However, most samples belong to the second type (Figure 3.9). In some samples, the length of lenticular kerogen-clay mixture can extend from sub-millimeter to several millimeters

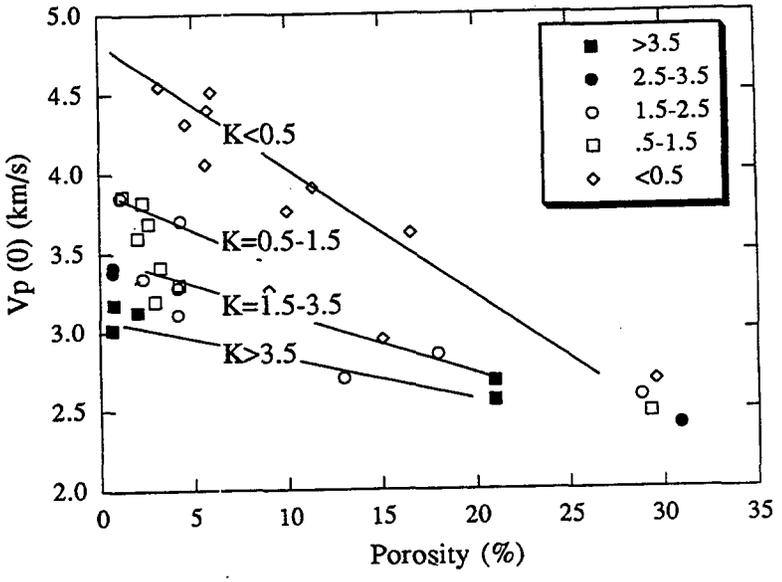

Figure 3.7: Crossplot of P-wave velocity versus porosity for the collection of shale samples. Velocities are high confining pressure data and for the direction perpendicular to bedding.

and, therefore, the third type can be called the "pseudo" lamination. These three texture features contribute to anisotropy in different ways and again also related to the mineralogy. For example, in the micro-lamination type, even though the properties of kerogen-clay mixture layers remain the same, the other layers, whether composed of carbonate grains (higher velocity) or siliceous material (lower velocity), can cause differences in the resultant anisotropy. Because of this, distinct dependence of elastic anisotropy on kerogen content is not expected. It is therefore mineralogy and texture that decide the extent of intrinsic anisotropy.

The measured anisotropy is found to depend strongly on the presence of bedding-parallel cracks. The cracks can be generated by hydrocarbon maturation, as proposed by Vernik (1992), or by pressure relief and/or sample preparation. Figure 3.10 shows an example (4696, organic/phosphatic shale) of cracks in both kerogen-rich layers and apatite-rich layers caused by pressure relief or sample preparation. The anisotropy parameters ϵ and γ are shown together with other Monterey subsurface samples. It has the highest intrinsic anisotropy which is the high pressure asymptotic value and the largest variation with pressure due to crack closure.

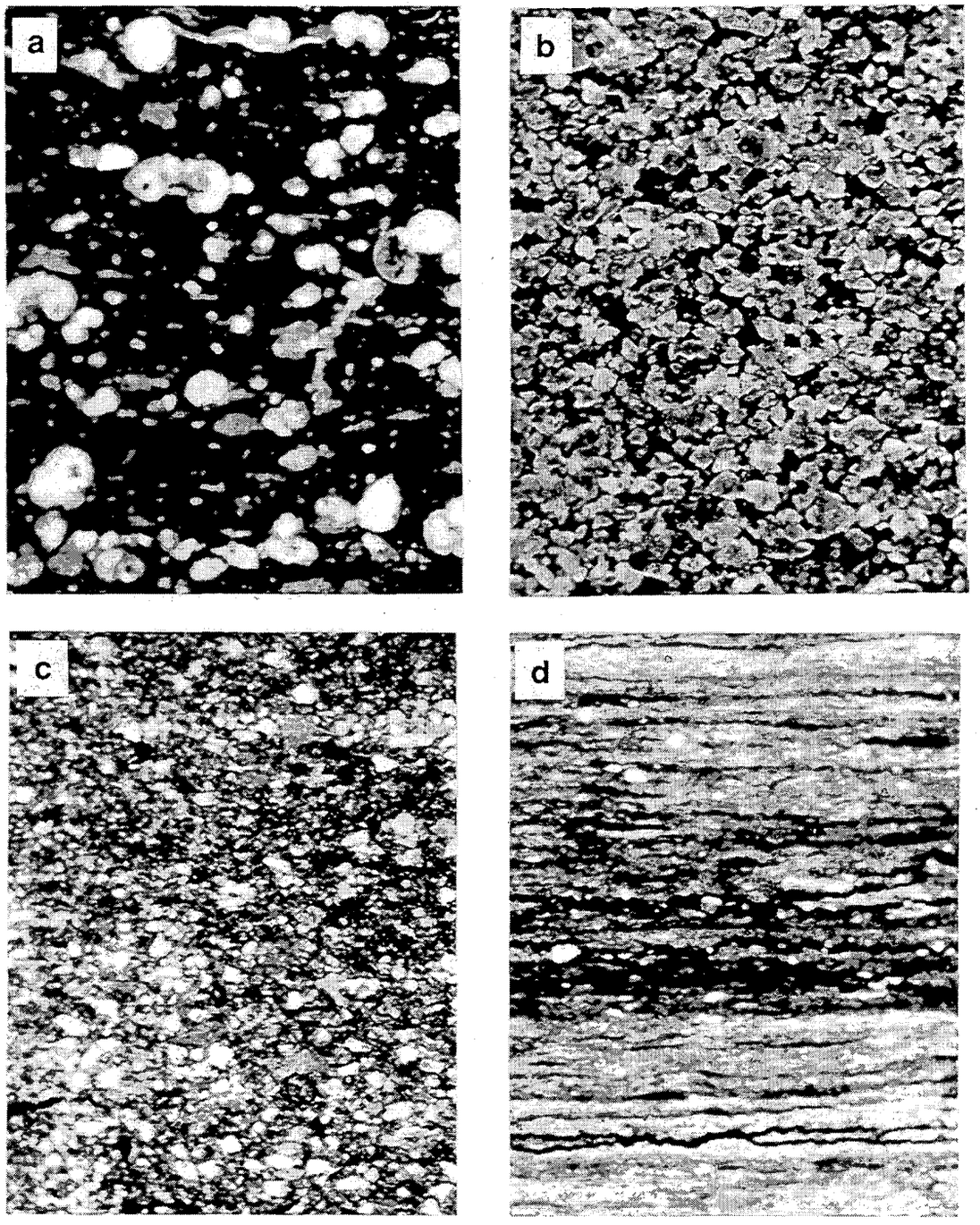

Figure 3.8: Photomicrographs of four different shale samples. *a* and *b* demonstrate the textural difference between isolated grains (biogenic silica) (a) and closely packed grains (dolomite) (b) in the matrix of kerogen-clay mixture. *c* and *d* demonstrate two different types of kerogen distributions in shales, the homogeneous type (c) and the laminated type (d). The vertical scales for *a*, *b*, and *c* are 1 mm and for *d* 2 mm.

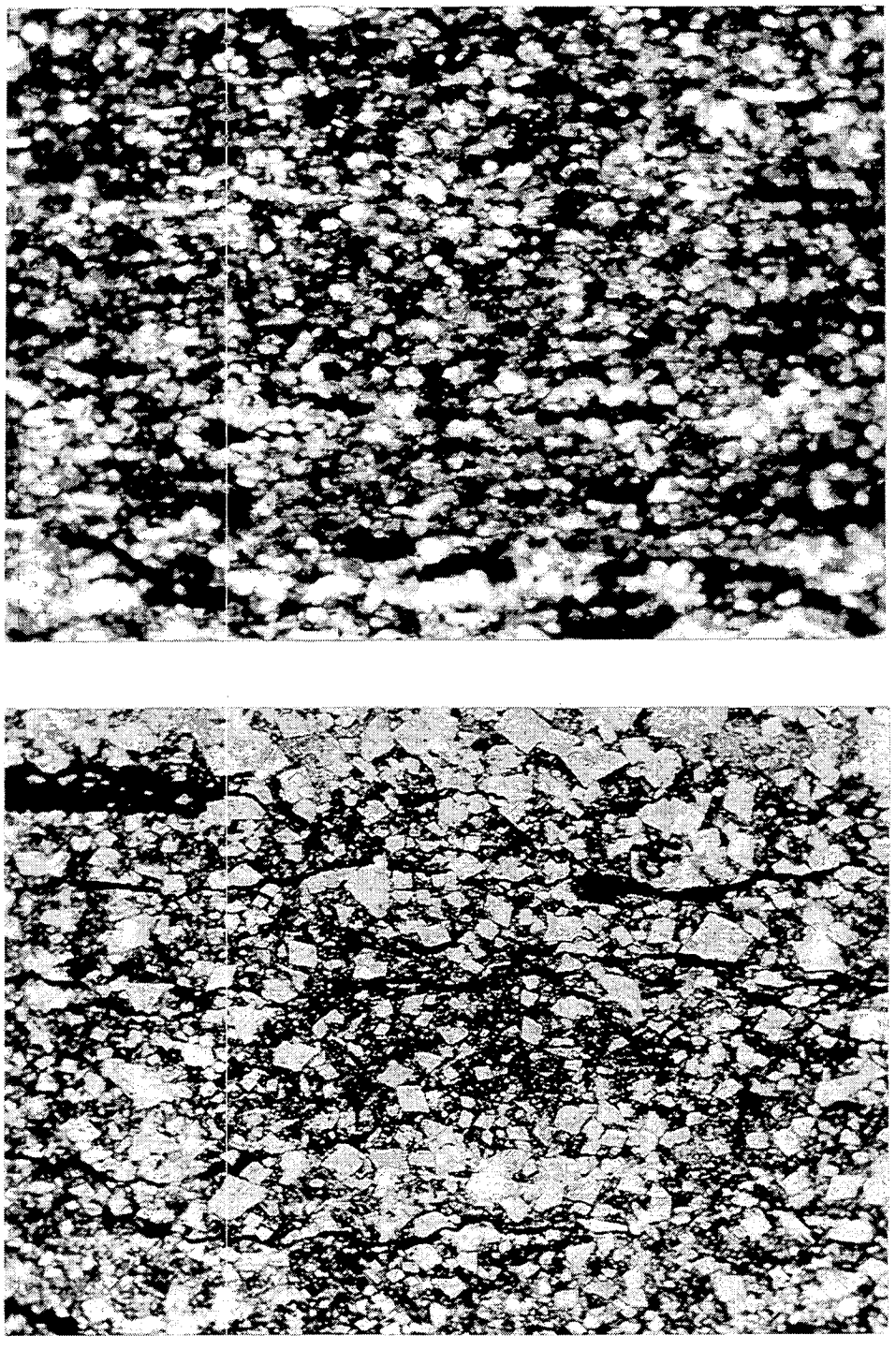

Figure 3.9: Photomicrographs of two shale samples showing preferrably aligned lenses of kerogen-rich mixture in the homogeneous background of the same material but with less kerogen. The vertical scale is 1 mm.

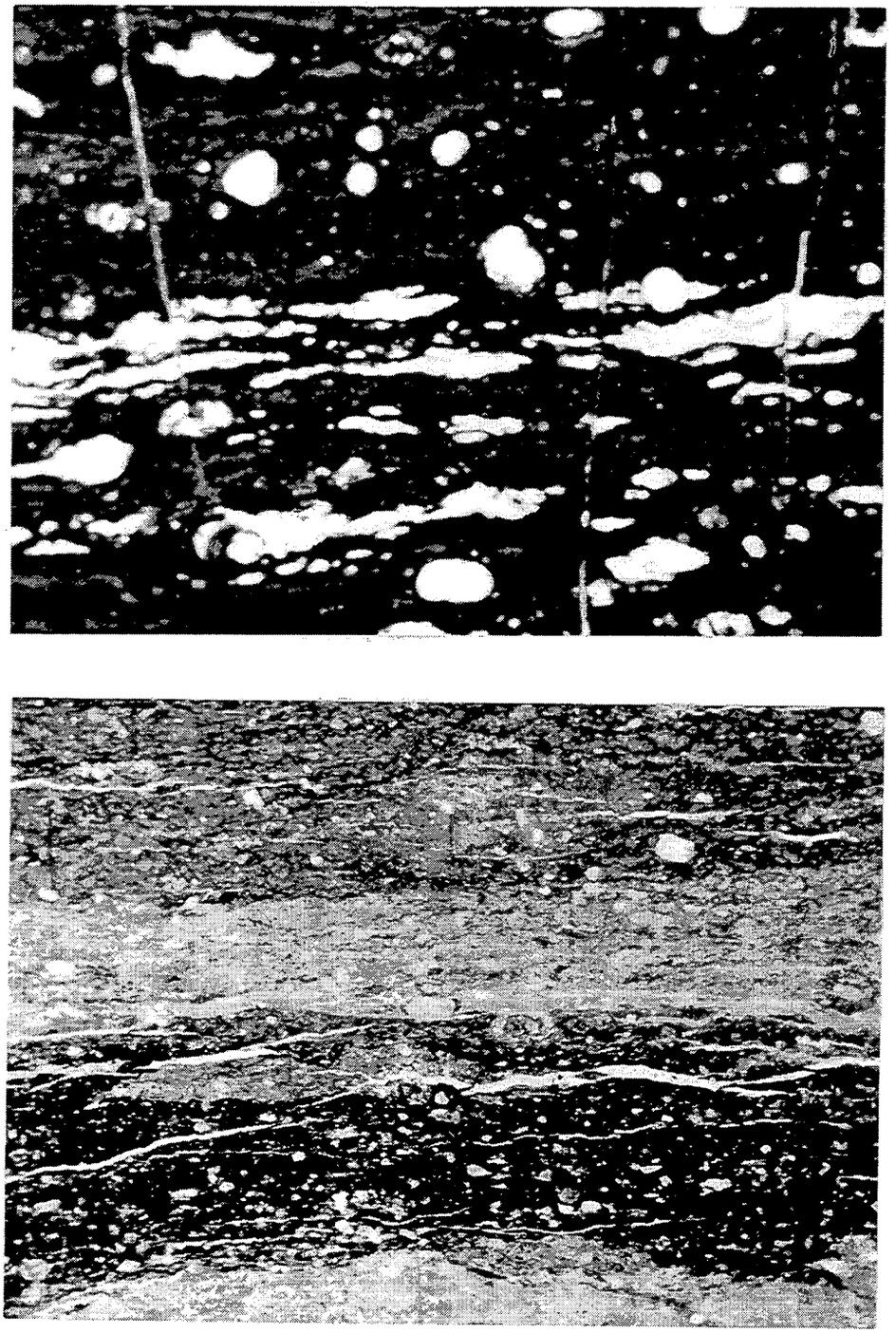

Figure 3.10: Photomicrographs of shale samples showing two types of cracks present in the Monterey formation shales: the natural subvertical cracks (filled with silica, white, or kerogen-rich material, black) from tectonic force (top) and fresh bedding-parallel cracks (filled with epoxy, white color) from the pressure relief/sample preparation (bottom). The vertical scale is 2 mm.

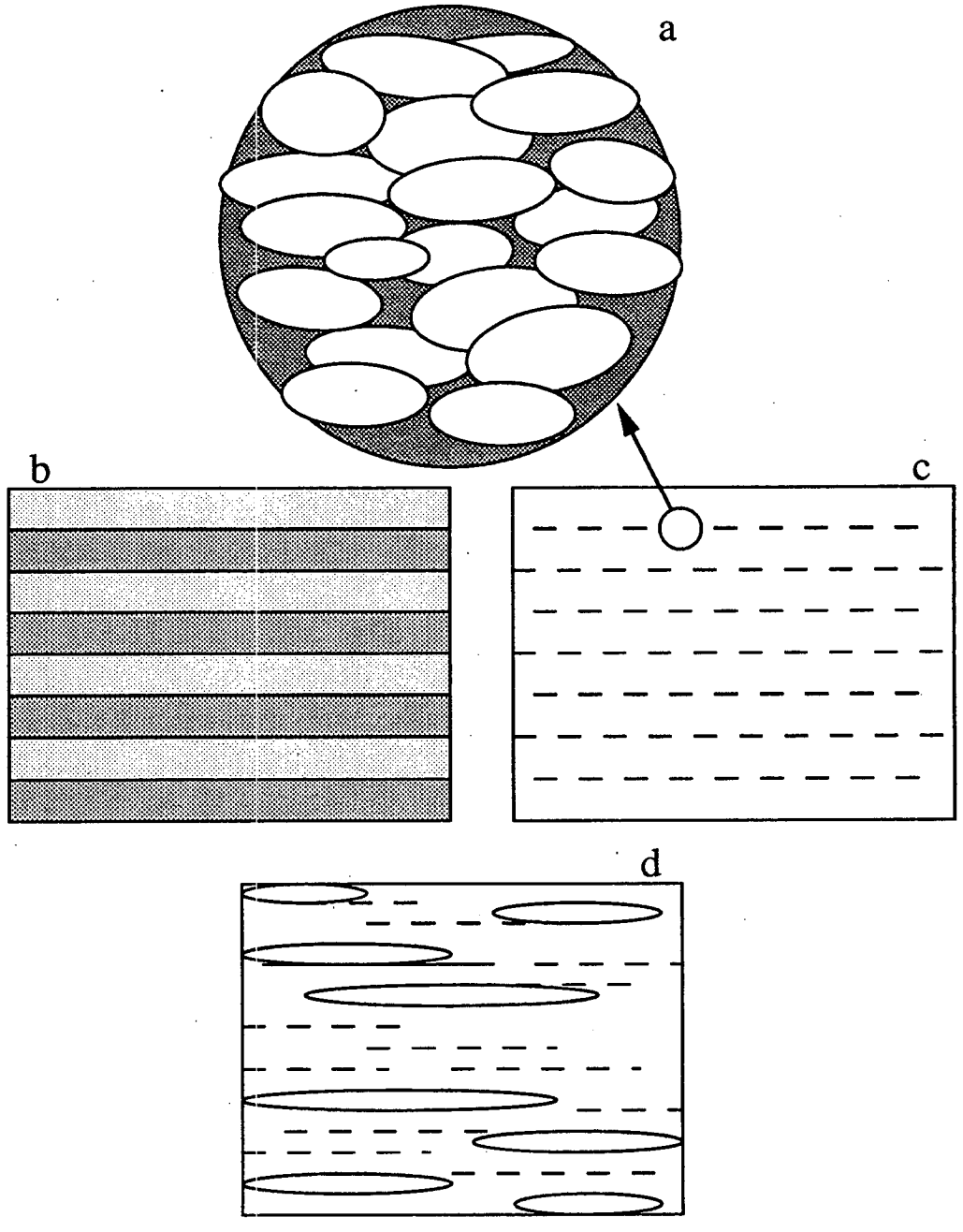

Figure 3.11: A physical model for the texture features of shale. (a) shows the kerogen-clay mixture that may be present in the shale matrix and kerogen-rich lenses; (b) is the micro-lamination structure; (c) is the matrix structure; (d) is the most common case which can be considered a transition in between (b) and (c).

3.2.4 A physical model for kerogen-rich shales

The textural features of shales discussed above can be intuitively described by a physical model shown in Figure 3.11. In the figure, (a) is the microscopic view of the anisotropic matrix constituted by clay particles (preferably oriented) immersed in the isotropic kerogen background. (b), (c), and (d) are typical models for kerogen-rich shales samples seen in the collection. (c) consists completely of the matrix (a) and the medium is represented by parallel dash lines. (b) consists of micro-laminated layers of kerogen-clay mixture having the texture feature of (a), high-concentration kerogen, and stiffer siliceous, calcareous, phosphatic, or other detrital materials. (d) can be seen as the mixture of type (b) and (c). It consists of the lenticularly shaped kerogen-rich material distributed in the matrix of kerogen-clay mixture. Model (c) is similar to the Bakken, Bazhenov, and Niobrara shales. Model (b) is most similar to the Monterey shales. And (d) is observable in all shales.

Modeling of elastic properties of shales has to take into account their textural features. For the micro-lamination case, effective medium theories for thinly-layered media can be used. In calculating elastic constants of the effective medium, the properties of kerogen-clay mixture and siliceous, phosphatic or dolomitic layers are estimated separately. The Backus averages (1962) can be used to calculate the effective elastic constants of the whole medium. For the majority of shales samples that have a distribution of the lenticularly shaped kerogen-clay mixture of highly concentrated kerogen patches, the modeling can be performed with scattering theory. However, as an estimate, the average of two extremity cases can be used to represent this transition case.

3.3 Effects of saturating fluids

When shales are saturated with fluid, at least three factors can affect the measured velocities: the mechanical effect similar to that given by Gassmann equation (1951); the physical/chemical reaction between clay and water (van Olphen, 1963) that may affect the frame elasticity; and the fluid flow-induced velocity dispersion (Biot, 1956; Mavko et al., 1991). Below, the mechanical effect is considered first, based on the equation given by Brown and Korringa (1975) and using a numerical experiment. Then, the measurement results on shales are presented and the weakening effect is introdued. Finally, an estimation is made on the effect of velocity dispersion.

3.3.1 The mechanical effect - a numerical experiment

Given the elastic constants of the dry medium, the mineral matrix, the saturating fluids, and porosity, the elastic constants of the saturated medium can be predicted from the following equation (Brown and Korringa, 1975)

$$S^d_{ijkl} - S^s_{ijkl} = \frac{(S^d_{ij\alpha\alpha} - S^o_{ij\alpha\alpha})(S^d_{kl\alpha\alpha} - S^o_{kl\alpha\alpha})}{(S^d_{\alpha\alpha\beta\beta} - S^o_{\alpha\alpha\beta\beta}) + (\beta_{fl} - \beta_o)\phi} \tag{3.1}$$

where ϕ is porosity, S^d_{ijkl}, S^s_{ijkl}, and S^o_{ijkl} are the elastic compliance (inverse of elastic stiffness) tensors of dry, saturated rock, respectively, and of a mineral matrix; β_{fl} and β_o $(= S^o_{\alpha\alpha\beta\beta})$ are the compressibility of pore fluid and mineral matrix, respectively.

Because of the interaction among different elastic constants of the mineral matrix, the dry rock, and the saturating fluid (i.e., two sets of five elastic constants for dry rock and mineral plus one for fluid), it is very difficult to gain an intuitive understanding of the effects of fluids through analytical discussions. Experimental measurements can provide real results, but it is very costly and next to impossible to cover all possible combinations of those elastic constants. A Monte Carlo simulation is therefore used to provide a statistical view on the fluid saturation effect. The procedure for generating a stochastic, fluid saturated sample and the prediction for saturated elastic constants using Brown and Korringa's relation are described below.

Constraints for a stochastic, fluid-saturated TI sample

There are two types of constraints on the stochastically generated fluid-saturated TI system. First, the stability (non-negative deformation energy) condition for a TI medium requires the positive semidefiniteness of the following matrix (Backus, 1962):

$$\begin{pmatrix} c_{11} & c_{12} & c_{13} & 0 & 0 & 0 \\ c_{12} & c_{11} & c_{13} & 0 & 0 & 0 \\ c_{13} & c_{13} & c_{33} & 0 & 0 & 0 \\ 0 & 0 & 0 & c_{44} & 0 & 0 \\ 0 & 0 & 0 & 0 & c_{44} & 0 \\ 0 & 0 & 0 & 0 & 0 & c_{66} \end{pmatrix}$$

which results in:

$$c_{44} > 0, \quad c_{66} > 0, \quad c_{33} > 0,$$
$$c_{12} + c_{66} > 0 \quad \text{and} \quad (c_{12} + c_{66})c_{33} > c^2_{13}$$

It is derivable then, $c_{11} > 0$, $c_{11} > c_{12}$, $c_{11} + c_{12} > 0$, and $(c_{11} + c_{12})c_{33} > 2c^2_{13}$.

The second type of condition restricts the range of variations for the elastic properties of the mineral matrix and the dry sample. The compressibilities along the two principle directions should be higher for the dry sample than for the mineral matrix;

$\Delta C_{11} < 0$	$\Delta C_{33} < 0$	$\Delta C_{13} < 0$	$\Delta\epsilon < 0$	$\Delta\delta < 0$	$\Delta\delta_{sv} < 0$
20%	0	33%	7.2%	7.2%	32%

Table 3.2: Monte Carlo simulation of fluid saturation effect in a transverse isotropic medium. See definitions for ΔC in Appendix A.

this is also true for the sample as a whole (the compressibility of the dry rock is larger than that of the mineral matrix):

$$c_{11}^o \geq c_{11}^{dry}, \quad c_{33}^o \geq c_{33}^{dry}, \quad c_{66}^o \geq c_{66}^{dry}, \quad c_{44}^o \geq c_{44}^{dry}, \text{ and}$$

$$\frac{c_{11}^{dry} + c_{12}^{dry} + 2c_{33}^{dry} - 4c_{13}^{dry}}{c_{33}^{dry}(c_{11}^{dry} + c_{12}^{dry}) - 2(c_{13}^{dry})^2} \geq \frac{c_{11}^o + c_{12}^o + 2c_{33}^o - 4c_{13}^o}{c_{33}^o(c_{11}^o + c_{12}^o) - 2(c_{13}^o)^2}$$

Simulation procedure and results

In generating a numerical saturated sample, the first step is to draw from a uniform distribution two sets of five elastic constants, each satisfying the stability condition. Then, only those satisfying the second-type constraint are kept. To calculate the change of the five elastic constants upon saturation, there is a $1/5$ chance for C_{11} and a $1/3$ chance for C_{13} to decrease among 5,000 tests. For $\Delta C_{11} < 0$, the cause is $1 - \Delta C < 0$. In all other cases, $1 - \Delta C$ are > 0. In this study, however, $1 - \Delta C > 0$; therefore it is believed that the decrease in C_{11} is not caused by a purely mechanical effect, but by a physical-chemical effect.

3.3.2 Measurements on shales - the physical-chemical effect

Five samples, two from the Bakken (US) formation (*a*, *b*), one from the Niobrara (USA) formation (*c*), and two from the Bazhenov (Russia) formation (*d*, *e*) are selected for the following analysis. Figure 3.12 shows the measured P- and S-wave velocities along with predictions using Brown and Korringa (1975) relations.

Fluid saturation-induced changes in the elastic stiffness of samples as measured and as predicted by considering only the fluid compressibility effect are shown below (instead of showing the actual values, only changes are shown in the table: + stands for increase, − for decrease, and 0 for no change):

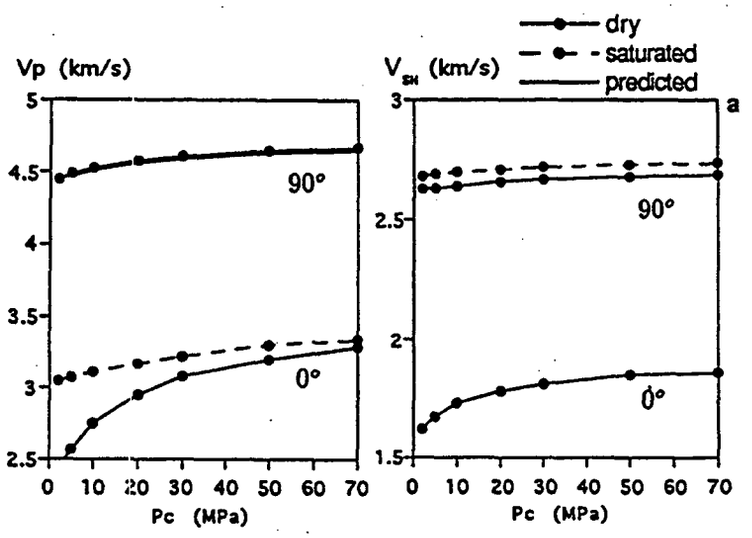

(a) Smectite-free, brine

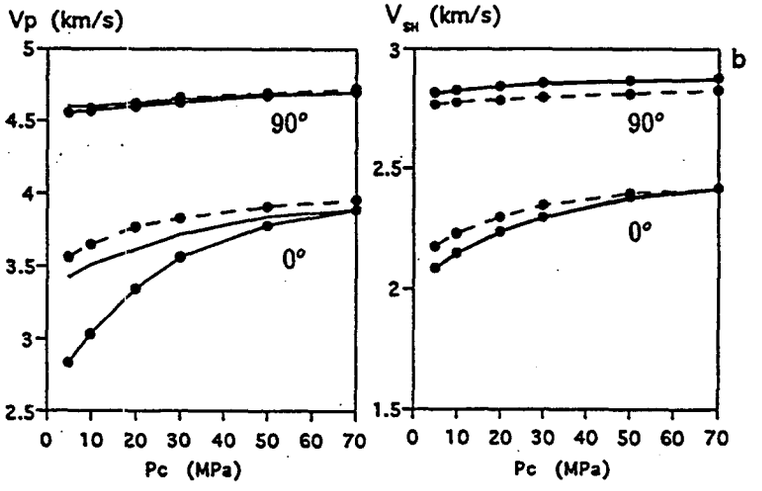

(b) Smectite-free, oil

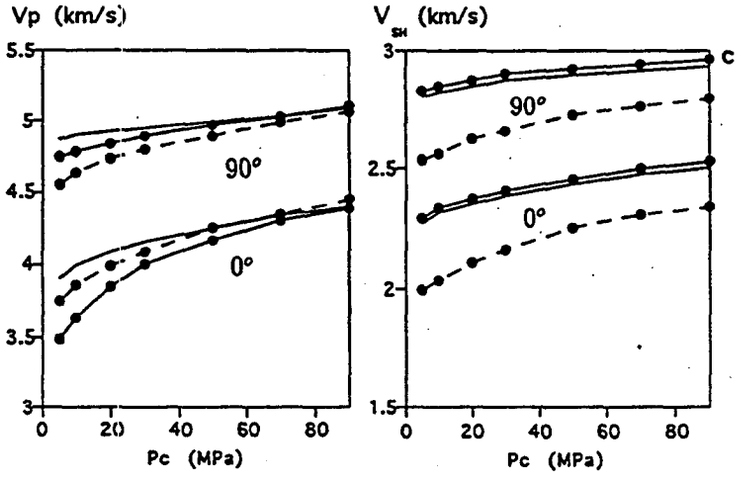

(c) 2% Smectite, brine

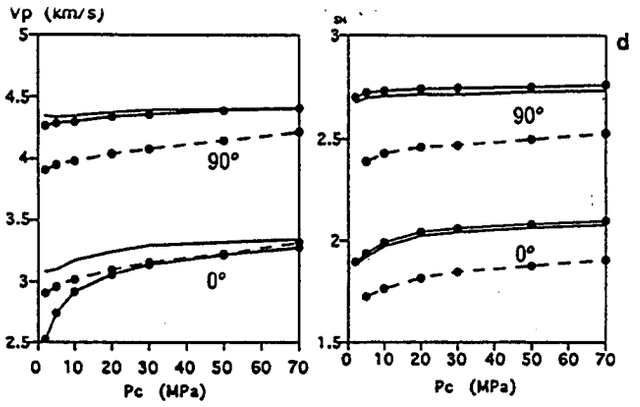

(d) 6% Smectite, brine

(e) 6% Smectite, oil

Figure 3.12: P- and SH-wave velocities for for the principle directions of shales with different smectite content and different saturating fluids.

sample	smectite (vol, %)	fluid type	C_{11}	C_{33}	C_{13}	C_{44}	C_{66}
a	0	brine	+	+	+	+	−
b	0	oil	+	+	+	+	−
c	2	brine	−	+	+	−	−
d	6	brine	−	+	+	−	−
e	6	oil	−	+	+	−	−
predicted			+	+	+	0	0

It is seen that none of the samples behave exactly as predicted. Two behaviors upon saturation can be recognized: 1) increase in C_{11}, C_{33}, C_{13}, C_{44} and decrease in C_{66} typical of smectite-free samples (a, b), and 2) increase in C_{33}, C_{13} and decrease in C_{11}, C_{44}, C_{66} in the shales with smectite (c, d, e). Two of the many acting mechanisms are discussed below: the fluid compressibility effect and the physical-chemical weakening of clay mineral (mainly water-swellable smectite) and grain contacts.

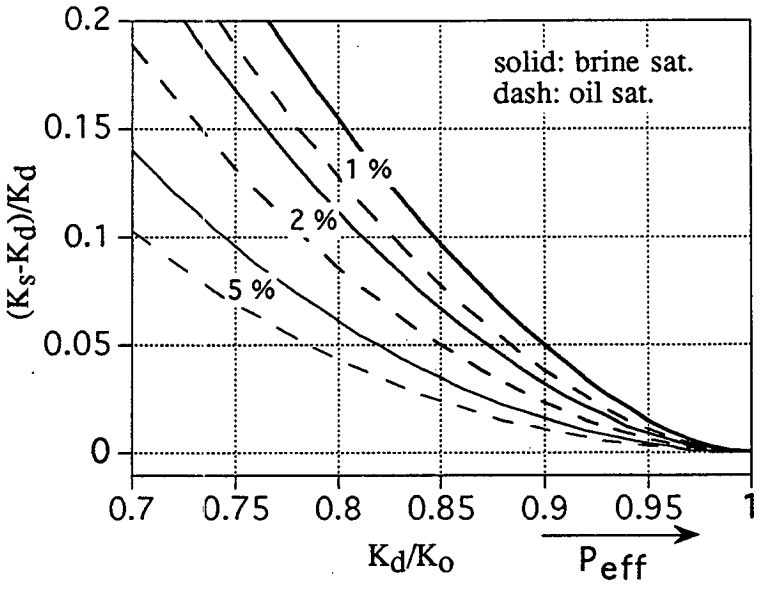

Figure 3.13: The relative increase in bulk modulus of an isotropic rock after saturation as predicted by Gassmann relations.

Stiffening effect of saturating fluids

Figure 3.13 shows how the relative increase $(K_s - K_d)/K_d$ (K_d and K_s are the dry and saturated bulk moduli) in the bulk modulus of an isotropic rock depends on porosity, dry rock modulus, and fluid properties according to Gassmann (1951) relations. This plot is basically designed to show the effect of confining pressure on the fluid saturation-induced increase in elastic stiffness of rocks. In agreement with the dominant bedding-parallel distribution of microcracks in mature black shales (Vernik, 1993), it explains the stronger fluid effect at low P_c in the more compliant bedding-normal direction as compared to the bedding-parallel direction. For an anisotropic rock, Brown and Korringa relations predict that normal stiffnesses C_{11} and C_{33} always increase with fluid saturation, whereas shear stiffnesses C_{44} and C_{66} do not change. Samples *a* and *b*, which are smectite-free, basically agree with the prediction except for the small increase in C_{44}. The increase in C_{44} is probably due to the non-zero shear modulus of fluid inside the thin microcracks at high frequency (Israelachvili et al., 1988). Also, Brown and Korringa equation is a low frequency theory. The high-frequency squirt theory does predict an increase in C_{44} (Mukerji et al., 1994).

Weakening effects of saturating fluids

Samples *c*, *d*, and *e*, which contain 2 to 6% smectite, show significant reductions in C_{11}, C_{44}, and C_{66}. These reductions display the weakening effects by fluids.

Absorption of water molecules into the crystalline lattice of clay minerals is known as the clay-swelling effect (van Olphen, 1963). Comparing Figure 3.14 (a) with (b), we see larger reductions in C_{11}, C_{44}, and C_{66} in the case of brine saturation (b) than in the case of oil saturation (a). The fact that C_{33} is less affected by saturation than C_{11}, and C_{11} and C_{33} together are less affected than C_{44} and C_{66} are, is clearly related to the anisotropic superposition of the fluid compressibility effect upon the water-rock interaction mechanism. Even with oil-saturation, we observe some reductions in C_{11}, C_{44}, and C_{66}. This is attributed to the slippage induced by fluids along the tangential grain contacts between overlapping clay platelets oriented subparallel to bedding. This effect can be referred to as the physical-chemical weakening.

To separately quantify the two different weakening effects, we assume the elastic stiffness of the saturated rock C_{ij}^s to be a sum of the dry rock stiffness C_{ij}^d, the fluid compressibility effect given by ΔC_{ij}^{mech} (as predicted by Brown and Korringa equations), the physical-chemical weakening effect given by ΔC_{ij}^{ph-ch}, and finally, the chemical weakening effect given by ΔC_{ij}^{chem}:

$$C_{ij}^s = C_{ij}^d + \Delta C_{ij}^{BK} + \Delta C_{ij}^{phys} + \Delta C_{ij}^{chem} \tag{3.2}$$

Further, we assume that the physical-chemical weakening effects caused by oil and brine are about the same. The procedure of decomposition is then shown in Figure 3.14 (b). At 50 MPa, the reductions in percent caused by the two types of weakening effects are shown below:

type	$\Delta C_{11}/C_{11}^d$	$\Delta C_{33}/C_{33}^d$	$\Delta C_{44}/C_{44}^d$	$\Delta C_{66}/C_{66}^d$
chem.	-6	-2	-12	-13
ph-ch	-5	-6	-5	-3

Therefore, the physical-chemical mechanism affects all the stiffness constants to about the same degree, whereas the chemical weakening affects the shear stiffnesses much more than the normal stiffnesses.

3.3.3 Laboratory versus field measurements

Below, the effect of frequency-related velocity dispersion is evaluated in shales by considering the critical frequency defined in Biot theory and the transition frequency operating in the local flow mechanism.

The Biot critical frequency is given by (Biot, 1956)

$$f_c = \frac{\phi\eta}{2\pi\rho_f\kappa} \tag{3.3}$$

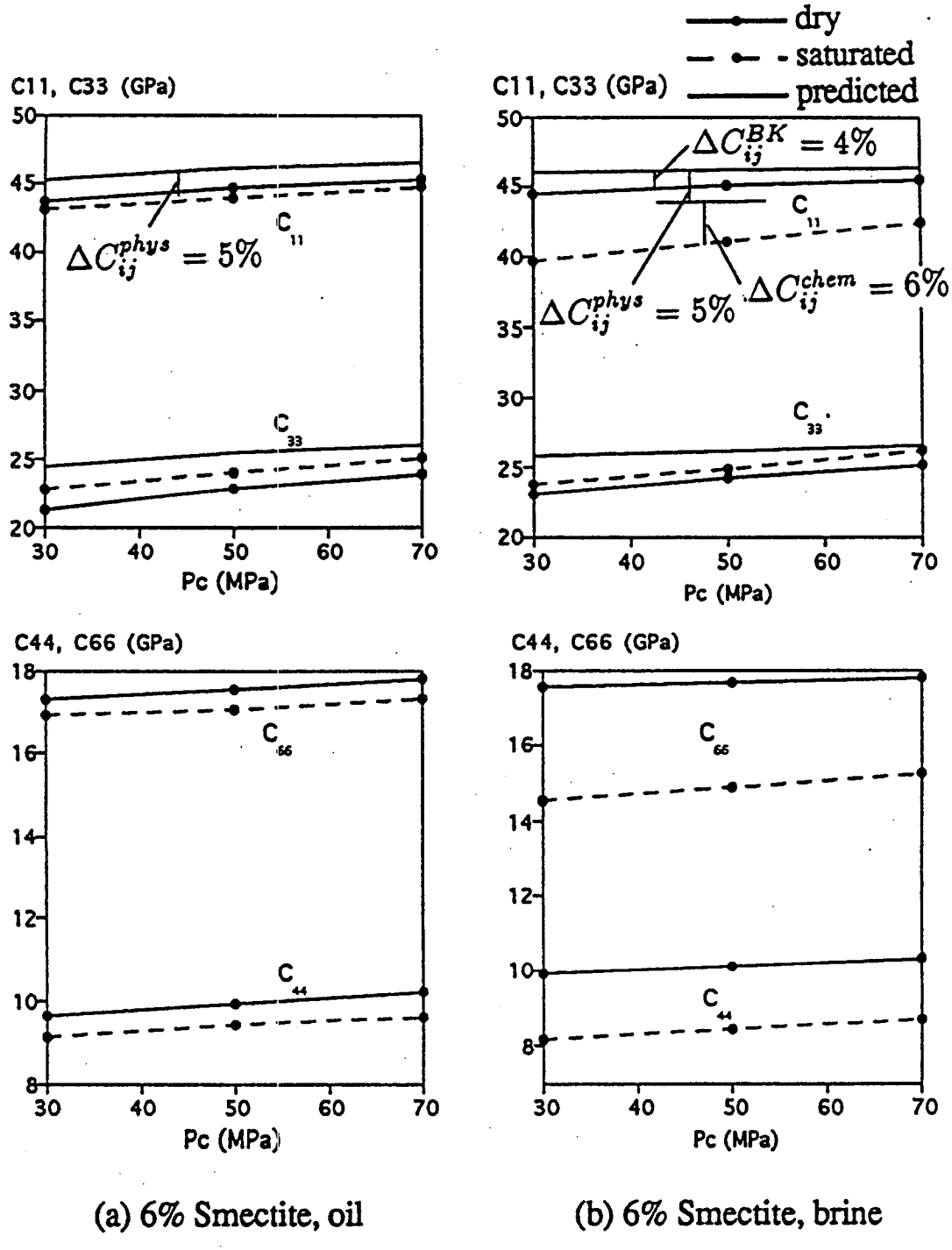

Figure 3.14: Elastic stiffness versus confining pressure in oil- and brine-saturated shales containing 6% smectite. Note that the curves for dry and saturated (predicted) shear stiffnesses overlap as fluid saturation does not affect the shear stiffness.

where ϕ and κ are porosity and permeability of rock and η and ρ_f are viscosity and density of fluid. The permeability measured in selected high porosity ($\phi \approx 30\%$) shales is on the order of 10^{-3} md. The majority of shales have much lower porosities (1 to 6%) and so do the permeabilities. On average, we choose ϕ=4% and, accordingly, $\kappa = 10^{-20}$ m^2 (10^{-5} md). The fluid viscosity $\eta = 10^{-3}$ $Pa \cdot s$ and density $\rho_f = 10^3$ kg/m^3. Therefore, the Biot critical frequency $f_c \sim 0.04 \cdot 10^{-3}/(2 \cdot 3.14 \cdot 10^3 \cdot 10^{-20}) \approx 6 \times 10^{11}$ Hz or 6×10^5 MHz. Compared with the ultrasonic frequency (1 MHz) that we use in our velocity measurements, the Biot critical frequency is much too high for any high frequency effect to be considered. It is noticed that this very high critical frequency is a direct result of the very low permeability of shale.

The transition frequency for local flow mechanism is more ambiguous because of the difficulty involved in estimating the squirt-flow length R which enters the equation (Dvorkin et al., 1993):

$$f_s = \frac{\kappa F}{2\pi R^2 \eta \phi} \tag{3.4}$$

where $F = (\frac{1}{k_{fl}} + \frac{1}{\phi Q})^{-1}$, $Q = k_o/(1 - \phi - k_d/k_o)$ (k_o and k are the bulk moduli of the mineral and dry rock, respectively).

Using the parameters given above and the bulk modulus of 2.3 GPa for fluid, 33 GPa for mineral modulus, and 28 GPa for dry rock modulus, we get $Q = 33/(1 - 0.04 - 16/33) \approx 70$ GPa and $F = 1/(\frac{1}{2.25} + \frac{1}{0.04 \times 70}) \approx 1.3$ GPa. R can be estimated according to its meaning as a dimension characteristic of the local flow length. In order for water to be expelled out of the pore space of source rocks during maturation, the microcrack aperture must be at least 0.1 μm (Vernik, personal communications). The aspect ratio of a typical microcrack in mature shales, as estimated from the closure pressure, is on the order of 10^{-3}. So the local flow path is at least 10^{-4} m (100 μm). Therefore, $f_s \approx 10^{-21} \times 1.3 \times 10^9/(6.28 \times (10^{-4})^2 \times 10^{-3} \times 0.04) \approx 5$ Hz, which is below the frequency range employed in borehole sonic and seismic studies.

Another equation used for estimating the transition frequency for local flow is given by (Mavko et al., 1975; O'Connell et al., 1977)

$$f_s \sim \frac{\alpha^3}{\eta} K \tag{3.5}$$

where α is the aspect ratio of cracks, η the viscosity, and K the mineral bulk modulus. It gives $f_s \sim 33kHz$ which is much higher than the above estimate. Note that the estimate by Equation 3.5 does not take into account of the permeability.

Assuming that Biot and local flow mechanisms are solely responsible for any frequency dispersion, the above calculations show that laboratory and borehole sonic

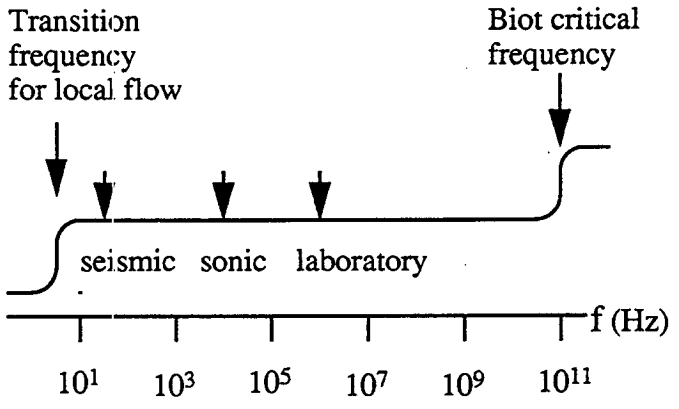

Figure 3.15: Schematic frequency spectrum illustrating the low (V_0) and high (V_∞) frequency limits for shales as well as the range from seismic to laboratory measurements.

measurements are in the same frequency range, as shown in Figure 3.15. Therefore, when applying the laboratory measurement results, corrections may not be needed as far as the frequency-related velocity dispersion is concerned.

3.4 Ultrasonic and sonic properties of the Monterey formation

The Miocene Monterey formation has long been recognized as a major petroleum source (organic-rich shale) and often an important reservoir (naturally fractured siliceous rocks) in many basins both onshore and offshore southern California (Isaacs, 1984). In the past, extensive studies have been made about the geology, geochemistry, and tectonics of the Monterey formation in order to understand the mechanisms of oil generation and transport. In contrast, little work has been published or done on its seismic properties. In this section, a detailed study on the velocity and elastic anisotropy of the Monterey formation rocks is presented using samples from both outcrop (Gaviota) and subsurface (Santa Maria basin). The purpose of study is to fill the gap of seismic properties of the Monterey formation for the application of sonic and seismic interpretations and to demonstrate how laboratory rock physics study can be used in delineating reservoir properties. In this section, the lithology and mineralogy of the samples are presented first. Then, the laboratory acquired velocity and elastic anisotropy are correlated with the mineralogy, kerogen content, porosity, and texture of the samples. Finally, core data are used to model the sonic responses of the formation and to interprete the field sonic log.

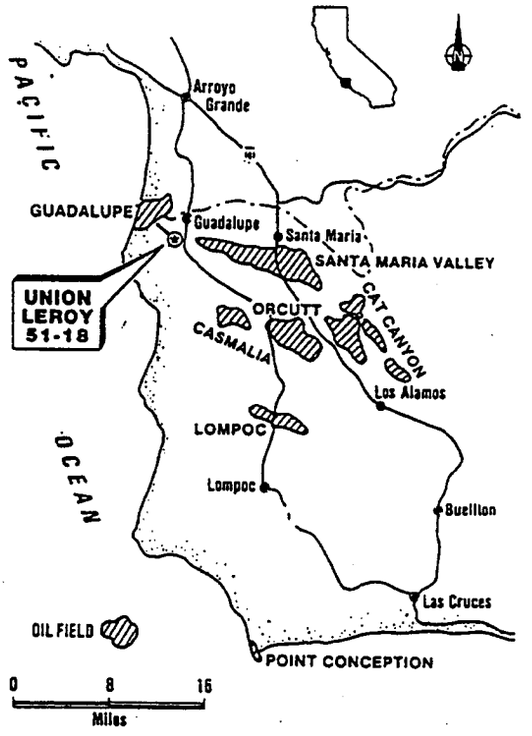

Figure 3.16: Location map for the Union-Leroy 51-18 well (Unocal), Santa Maria Valley field, Santa Maria basin, California.

3.4.1 Lithology, mineralogy and petrography

Lithologies of core samples from the Monterey formation are determined from their mineral compositions. In the ternary diagram commonly used for the rock type classification of the Monterey formation, three end-member rock components are detritus, carbonate, and biogenic silica (Isaacs, 1981b). For the purpose of sub-classifying shales, another ternary diagram can be introduced for detritus (Figure 3.17), for which three end members are shale (siliceous shale), kerogen (organic shale), and phosphate (phosphatic shale). Note that all boundaries are approximate.

Samples for this study come from the outcrop (coast) and two onshore wells, Union-Leroy 51-18 (Unocal, see location map in Figure 3.16) and Union-Humble Bell 1-56 (USGS) in the Santa Maria Valley field, Santa Maria Basin, California. The subsurface samples scatter in depth within the phosphatic and siliceous facies of the Monterey formation. There are 4 dolomite (3 of them are shaly dolomite), 2 porcelanite, and 4 shale samples altogether. Table 3.3 lists the sample depth, rock type, TOC (Rock-Eval), XRD mineralogy, porosity, and mineral density of these samples. The petrography of six selected samples are described below.

4560 and 4571 (porcelanite, see Figure 3.10 upper photo) are very similar and

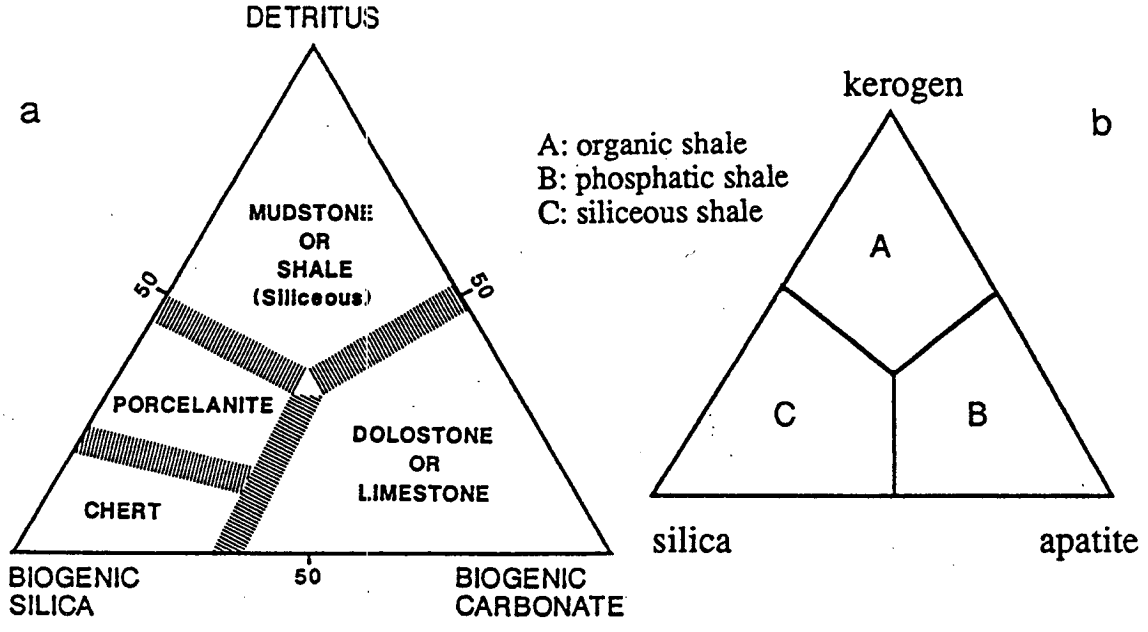

Figure 3.17: Ternary diagrams of rock types in the Monterey formation. (a) shows the four basic rock types (after MacKinnon, 1989b), chert, dolomite, porcelanite, and shale. and (b) subdivides shale into three types: siliceous, phosphatic, and organic.

depth (ft)	rock type	TOC (% wt)	dolomite (%)	detritus (%)	silica (%)	Por (%)	Density (g/cm^3)
4560	porcelanite	2.40	0	20.8	73.2	11.4	2.17
4571	porcelanite	2.28	0	15.1	79.0	10	2.14
4590	dolomite	0.19	93.4	2.3	0	3	2.72
4642	shaly dolomite	8.12	64.6	24.6	0	16.5	2.38
4685	shaly	8.19	35.5	40.7	0	21	2.35
4696	shaly	18.2	0	61.2	0	21	2.02
4771	shaly dolomite	5.83	59.2	19.1	0	19	2.49
4798	shale	9.31	27.1	52.8	0	18	2.35
5478	shale	6.81	0	84.4	0	5	2.24
5553	shaly dolomite	0.52	64.2	29.6	0	11	2.70

Table 3.3: Petrochemical parameters of the Monterey formation shale samples from the Union-Leroy 51-18 and the Union-Humble Bell wells, Santa Maria Valley, Santa Barbara, California.

both are characterized by fine laminations of highly siliceous material, kerogen-clay mixture, and highly organic matter. The laminae thickness ranges from 20-30 μm to 1 mm (coarser in 4560). The presence of natural fractures (average spacing 3 to 4 mm) and cracks verifies other studies that fracture development is highest in more siliceous rocks (Sadler, 1990).

4590 (dolomite) contains finely grained, nearly pure dolomite. Scattered silica patches in lenticular forms show weak alignment along the bedding direction which is believed to cause most of the anisotropy since elastic properties of silica and dolomite differ. Natural fractures also exist.

4642 (shaly dolomite, Figure 3.8, upper right photo) is quite remarkable in that it consists of very high percentage of euhedral carbonate grains (most of them have point contacts with neighbors) dispersed nearly isotropically in the groundmass of kerogen-clay mixture. The anisotropy should be caused by continuous kerogen-clay laminae which are 1 to 2 mm thick and 2 to 5 mm spaced.

4696 (organic/phosphatic shale, Figure 3.10 lower photo) contains interlayered organic-rich substance and microcrystalline phosphate. Volumetric contents of both TOC and phosphate are the highest among all samples. Cracks as long as half a centimeter in organic-rich layers are contained entirely along the bedding plane. In phosphate, abundant bedding-parallel cracks were produced by stress relief or sample preparation as seen by filled fresh epoxy. Some minor vertical cracks exist and it shows the more brittle nature of phosphate.

4771 (phosphatic shale) is rich in both phosphatic nodules and carbonate grains of less euhedral form. Carbonate grains show preferred alignment. The fabric of this sample, however, is dominated by phosphate layers with a thickness of 0.3 to 1.5 mm.

From the anisotropy point of view, there are two major types of fabrics in the Monterey formation samples. One is the micro lamination of kerogen-clay layers with other materials: silica, phosphate, or carbonate. The layers are on the millimeter scale and are more or less continuous. Another is the weak alignment on the finer scale of lenticularly shaped kerogen-rich substances. The minor fabric features include the preferred orientation of clay particles and interspersed biogenic silica or dolomite grains.

3.4.2 Ultrasonic velocity and anisotropy

At least three factors may affect the correlation between laboratory plug-scale core measurements and in-situ sonic measurements: lithology, porosity, and formation pressure. Below, we first consider how average velocities are affected by these factors.

As a rough estimate, the confining pressure at depth z is given by the lithostatic state of stress minus the hydrostatic stress (i.e., no tectonic stress): $P_c = (\rho_{rock} - \rho_{water})gz$ (g: gravitational constant, z: depth). Further, assuming the average bulk density of saturated rock to be 2 g/cm^3, $P_c = 0.003h$ (h in foot). From 4500 ft to 5000 ft of depth, the confining pressure then changes from approximately 13.5 MPa to 15 MPa, or 1.5 MPa difference, which is negligible. Therefore, velocities at about 15 MPa are used when correlating laboratory measured velocities with measurements in situ.

In Figure 3.18 which plots ultrasonic velocities versus porosity, dolomite samples (e.g., 4590 and 5553) have the highest velocities. As samples become more shaly, both P- and S-wave velocities decrease, as shown by 5478, 4798, and 4696 compared with the more dolomitic samples at approximately the same porosities. Siliceous rocks (4560, 4571, 5, 6) tend to have intermediate velocities. As a first order approximation, on the P-wave velocity plot, phosphatic, organic, and siliceous shales (5478, 4798, 4696, 3) can be grouped together, and porcelanite (4560, 4571, 5) or chert can be grouped together. The effect of shaliness on P-wave velocities of dolomitic rocks is very strong. However, except 4590, which is almost pure dolomite, and 5553, which is more compacted than the others, all other dolomitic samples (8, 9, 4642, 4771) can be grouped together. The following equations can then describe the velocity-porosity relations for the three groups (since the small number of data points tends to make linear regression biased, the equaitons are fit by eye):

$$
\begin{aligned}
V_p &= 7.0 - 0.1\phi && \text{(dolomite)} \\
V_p &= 5.9 - 0.096\phi && \text{(shaly dolomite)} \\
V_p &= 4.83 - 0.075\phi && \text{(porcelanite or dolomitic shale)} \\
V_p &= 4.37 - 0.06\phi && \text{(kerogen-rich shales)}
\end{aligned}
$$

The slope for dolomite group is more arbitrary than the others since there are only two samples and one of them (5553) is quite siliceous. For S-wave velocities, only two groups are distinct, shaly dolomite and porcelanite, and shales. This is because of the coalescence of the trending lines for porcelanite and shaly dolomite due to the high S-wave velocity of quartz. The velocity-porosity relations grouped by lithology for S-waves are

$$
\begin{aligned}
V_s &= 3.9 - 0.065\phi && \text{(dolomite)} \\
V_s &= 3.24 - 0.061\phi && \text{(shaly dolomite, porcelanite)} \\
V_s &= 2.67 - 0.047\phi && \text{(shales)}
\end{aligned}
$$

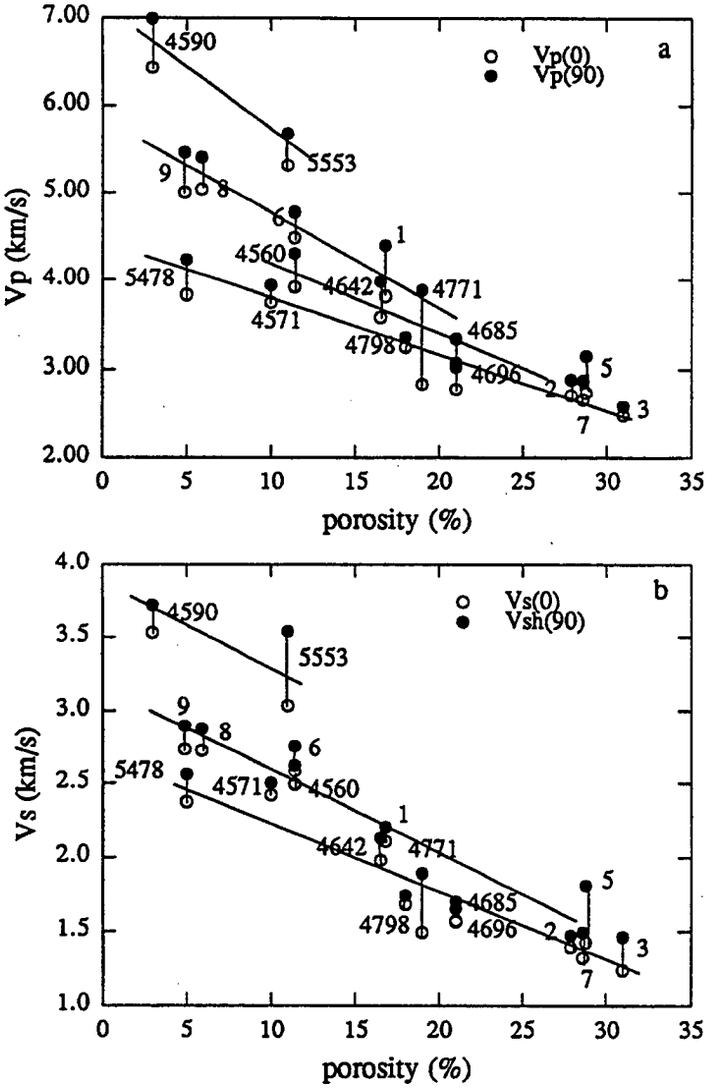

Figure 3.18: P- and S- wave ultrasonic velocities of the Monterey formation samples (water saturated) from Union-Leroy 51-18 well, Santa Maria Valley field, Santa Barbara, California.

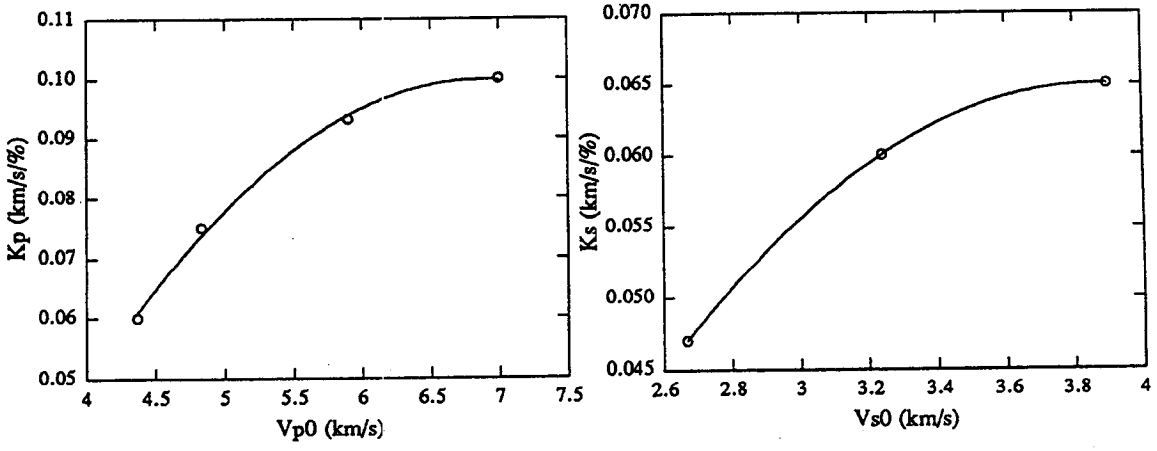

Figure 3.19: Crossplots of the slopes in the velocity-porosity relationship versus velocity. a is for V_p and b for V_s.

The velocity modeling scheme adopted in Section 3.2 is applied to some samples reported in Dunham (1990). These samples were taken from the same core in the same depth range. For convenience, the slope of velocity variation versus porosity is functionally related to the matrix velocity (Figure 3.19) by a third power polynomial. For V_p, the slope $k_p = -0.192+0.0845V_{p_0}-0.00613V_{p_0}^2$. For V_s, the slope $k_s = -0.121+0.096V_{s_0} - 0.0124V_{s_0}^2$. The predicted P-wave velocities are shown in Figure 3.20 using velocity histograms for each major rock type. Measurements from in this study are marked by cross. It can be seen that the scattered measurements fall within the predicted region of each rock type. Therefore, the measurements are representative for the modeling purpose. The representative velocity for siliceous shales, which was not in the collection, can be picked up from the predicted values.

The anisotropy is mainly affected by lithology, kerogen content, and confining pressure. Figure 3.3 and Figure 3.4 shows how anisotropy parameters ϵ and γ of both subsurface and outcrop samples vary with confining pressure and lithology. It is concluded that elastic anisotropy as characterized by ϵ and γ is strongest in the organic shale and lowest in porcelanite or chert; dolomitic shale or shaly dolomite have the intermediate anisotropy. These criteria are used to assign the anisotropy ratios to the average velocities predicted above. Below about 20 MPa, anisotropy is strongly affected by confining pressure. The main reason for this is that the effect of crack closure is more significant at low pressure; In some cases, texture may be important. For examle, when dolomite grains are interspersed in the softer kerogen-clay mixture, an increase in stiffness with pressure is expected grain contacts are enhanced.

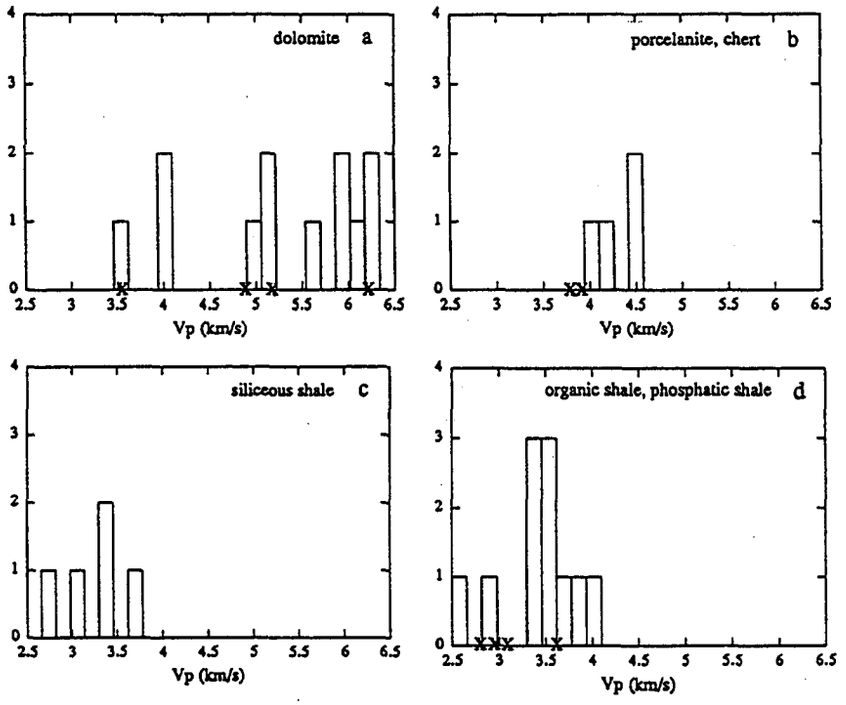

Figure 3.20: Predicted P-wave velocities for samples in Dunham (1990), grouped by major rock types.

3.4.3 Sonic response - modeling and interpretation

Core study is made on inch scale samples and conducted with ultrasonic measurement. Large scale fractures, for example, may have been intentionally avoided in sampling. The sonic measurement, however, should sense these fractures as well as imperfect wellbore conditions because of longer wavelength and traversing longer distance. This is elaborated below by a comparison between core and sonic measurements and by modeling the sonic responses.

A comparison between laboratory ultrasonic velocity measurements and the sonic log truncated at corresponding sample depths for some major rock types is shown in Figure 3.21. According to the brittleness of rocks, there are three cases:

brittle rocks

The difference between the two velocityf measurements is large. In thin layers (4494-4504), it is more significant.

brittle-ductile shale

At some depths, the agreement is good. At other depths, there is disagreement. However, the difference is not as significant as that of brittle rocks.

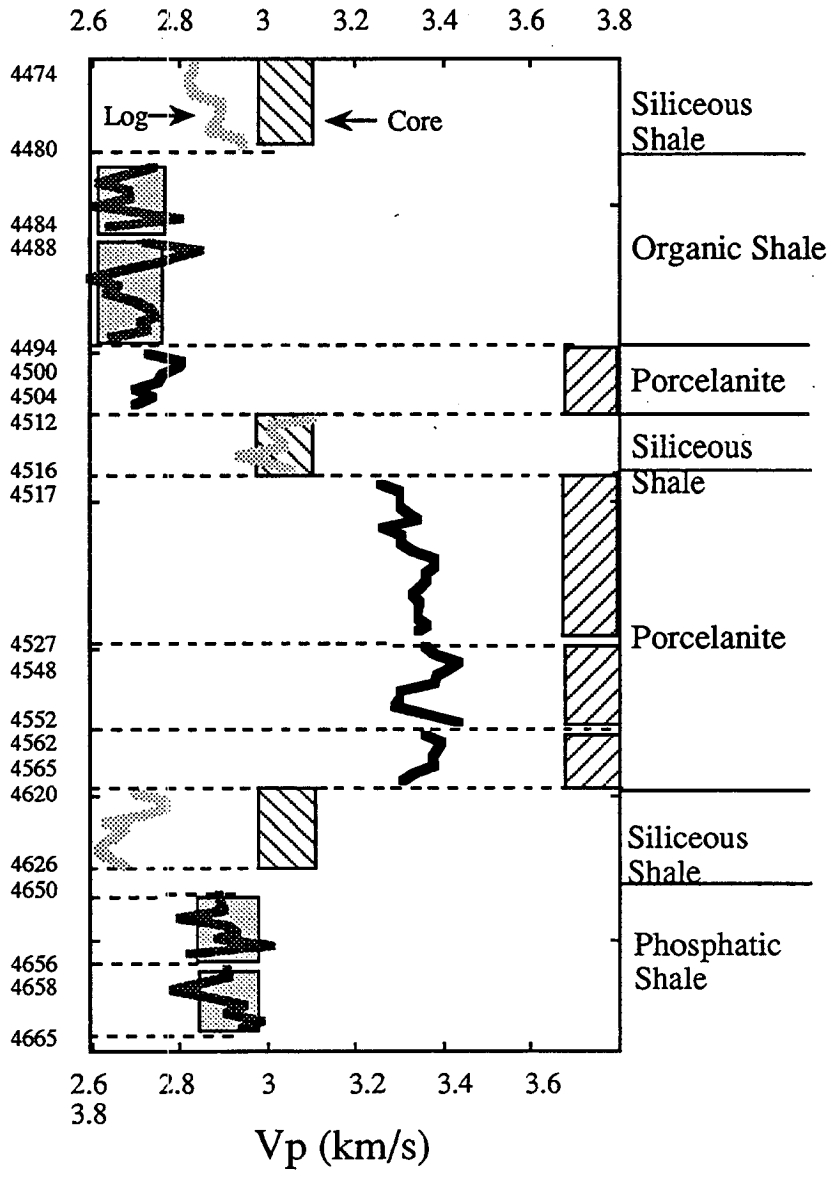

Figure 3.21: Comparison between core measurements and sonic log for some major lithologies of the Monterey formation. Union-Leroy well 51-18.

ductile shales

In both organic shale and phosphatic shale, velocity agreement in the two types of measurements is seen.

Therefore, there exists a close tie between the velocity mismatch and the rock types. Union-Leroy 51-18 well is located on one of the flanks of a slightly asymmetric anticline created by horizontal compressive stresses. Studies (Sadler, 1990; Narr, 1991) of the fracture distribution in the Monterey formation have shown that fracture development is highest in the more siliceous rocks (chert and porcelanite) and is lower in more shaly rocks. It is concluded therefore that the discrepancy between laboratory core measurements and sonic log is directly related to fracture density. In other words, by comparing the two measurements, the fracture distribution along the well can be delineated.

In the comparison, however, the tool configuration and wave frequency factors should also be included, especially for thinly layers formations. In the modeling below, two schemes corresponding to two frequency extremes are used with appropriate consideration of the sonic tool configuration (Figure 3.22). At the high frequency extreme, the total travel time between two receivers is the sum over the travel times through individual layers (ray tracing):

$$t = \sum t_i \tag{3.6}$$

where t_i is the travel time through layer i. Velocity is then given by $V = D/t$ (D is the receiver spacing). At the low frequency extreme, the layers behave as an effective medium with elastic constants being the averages of individual layers that the wave travel through. For a layered medium, Backus equations (Backus, 1962) give the five elastic constants of the effective medium in properties of individual layers:

$$\begin{aligned} c_{11} &= < c_{11} - c_{13}^2 c_{33}^{-1} > + < c_{33}^{-1} >^{-1} < c_{33}^{-1} c_{13} >^2 \\ c_{33} &= < c_{33}^{-1} >^{-1} \\ c_{13} &= < c_{33}^{-1} >^{-1} < c_{33}^{-1} c_{13} > \\ c_{44} &= < c_{44}^{-1} >^{-1} \\ c_{66} &= < c_{66} > \end{aligned} \tag{3.7}$$

Velocities can be calculated from the five elastic constants. The sonic response is modeled using the lithology column generated from core description (Dunham, 1990). Because the well penetrates one flank of an anticlinal structure, waves travel at an angle with the principle direction. The change of this angle is given by angles measured at the depth of samples (Figure 3.23 (b)).

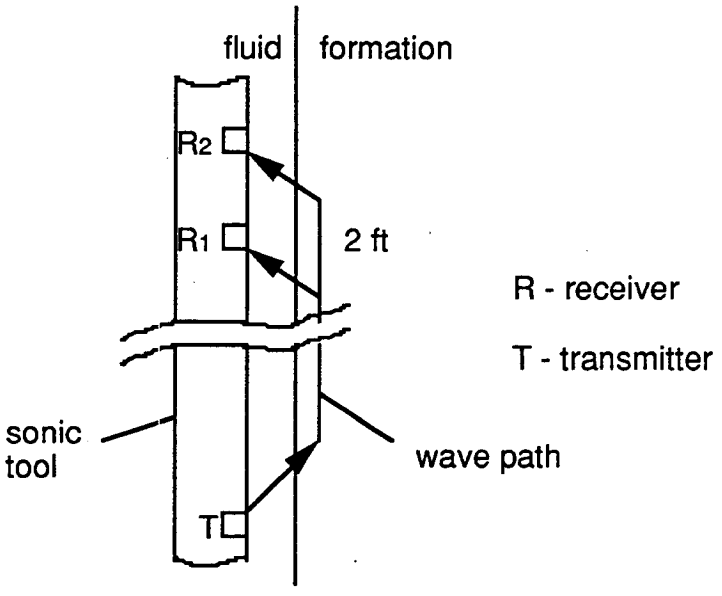

Figure 3.22: Sonic tool configuration with two measurement schemes. The receiver spacing between R_1 and R_2 is 2 ft.

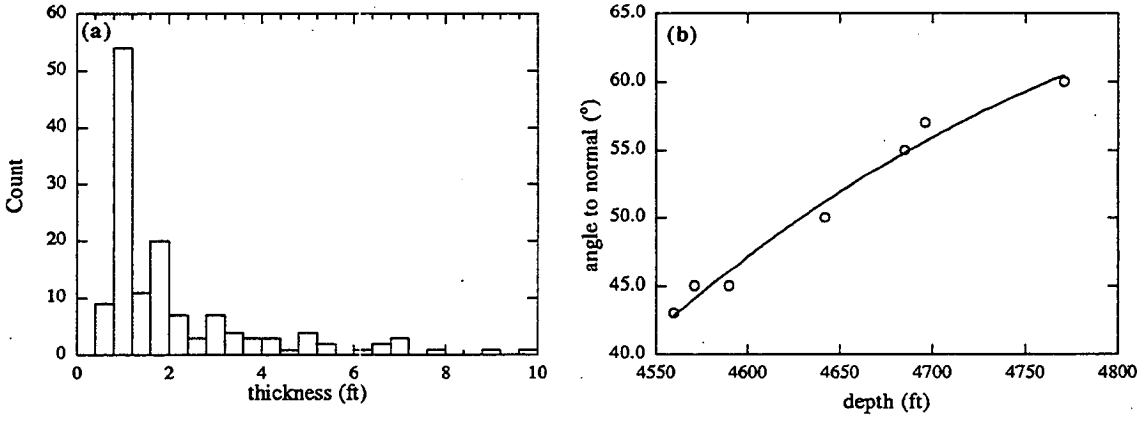

Figure 3.23: Histogram of the major layer thickness (left) and the angles of waves traveling relative to the bedding direction (right).

Inputs to the modeling program are velocities for typical rock types (from measurements at 15 MPa confining pressure or the above predictions in the case of siliceous shale), angles relative to the bedding normal direction , rock types (coded), and layer thickness. The histogram for layer thickness is shown in Figure 3.23 (a). We see that most layers are below 2 ft thick. Backus averaging (low frequency extreme) requires thin layering. Using the nominal frequency of 10 kHz, the wavelength would be around 0.4 m or 1.3 ft. However, due to attenuation the central frequency of actual propagating signal could be lower and therefore the wavelength is longer 1.3 ft. Also, as seen from core photographs, there is no drastic change in lithology at most depths and fine layering is a common feature at all depths. Therefore, use of Backus average is likely justified. The variation of angle with depth can be fit by $\theta = -3428 + 1.4089z - 0.000142z^2$ (z in ft) (Figure 3.23) from the dip angles measured at sample depths.

Modeling results are shown in Appendix D. Overall, ray-tracing average scheme provides a better match with sonic log than the Backus average scheme. This implies that the high frequency extreme, to which ultrasonic measurement belongs, works better in situ in even highly inhomogeneous formations, as long as the tool configuration is accounted for. Therefore, the ultrasonic measurement and sonic measurement are in the same frequency range as far as the frequency-related dispersion is concerned.

3.5 Conclusions

Though kerogen effect is of great interest in this study, mineralogy and texture are the most important factors affecting the elastic properties of shales. Realizing this can avoid the over-simplification of blindly correlating seismic velocity or elastic anisotropy with kerogen content and exaggering the role of seismic methods in detecting hydrocarbons. For example, the velocity-porosity relation of shales does depend on kerogen content. However, the dependence is far less strong than that on mineralogy.

A rather complete rock physics study such as this one, starting with laboratory core analysis and ending with field sonic interpretation, of the Monterey formation has been the first time. This work not only demonstrates the importance of laboratory measurements but also provided the practical tools both for theoretical analysis and for linking with field scale applications. For example, the detection of fractured layers through comparison of laboratory measurement and sonic logging can be a very useful way in locating reservoir zones.

Effects of fluid saturation in anisotropic porous media are difficult to tackle both experimentally and analytically. The numerical Monte Carlo experiment in this study offers a promising solution to the problem. As an example of its applications, artificial anisotropic samples can be made based on the numerical analysis results to focus on properties such as pore geometry, distribution of anisotropic particles, signal frequency, and so on.

Low porosity shale samples that contain different amounts of smectite are shown to be affected upon saturation by mechanical stiffening, but more importantly, by the chemical and physical-chemical weakening effects of saturating fluids. The ultrasonic velocities in shales measured in the laboratory may not require any frequency dispersion correction when applied to borehole sonic/seismic studies. However, the chemical and physical-chemical weakening effects may be very strong and should be accounted for in interpretation. They are related to water absorption into clay mineral structure and slippage along grain contacts lubricated by pore fluid, respectively.

Acknowledgements

This study was partially sponsored by Arco, BP, Marathon, Mobil, Norsk Hydro, Shell, Texaco, and Unocal through a shale project within Stanford Rock Physics Project (SRB). The author is supported as a Ph.D student through SRB. He wishes to thank Dr. Lev Vernik for acquiring samples and helping with part of the experimental work. He also thanks Dr. Amos Nur, Dr. Gary Mavko, Dr. Leon Thomsen, and Dr. De-hua Han for their advice and suggestions during discussions.

Appendix

A. The elastic description of a transverse isotropic (TI) medium

A TI medium has hexagonal symmetry. Its elastic properties can be fully characterized by 5 independent elastic constants. Let axis 3 of a Cartesian coordinate be along the symmetry axis and axes 1 and 2 be in the plane perpendicular to the symmetry axis, the stiffness matrix then takes the form (Auld, 1990)

$$\begin{pmatrix} c_{11} & c_{12} & c_{13} & 0 & 0 & 0 \\ c_{12} & c_{11} & c_{13} & 0 & 0 & 0 \\ c_{13} & c_{13} & c_{33} & 0 & 0 & 0 \\ 0 & 0 & 0 & c_{44} & 0 & 0 \\ 0 & 0 & 0 & 0 & c_{44} & 0 \\ 0 & 0 & 0 & 0 & 0 & c_{66} = \frac{1}{2}(c_{11} - c_{12}) \end{pmatrix}$$

The 5 constants c_{11}, c_{12}, c_{33}, c_{44}, and c_{13} can be obtained experimentally from body wave velocity measurements and with the density ρ, as

$$\begin{aligned} c_{11} &= \rho {V_p}^2(90^\circ) \\ c_{12} &= c_{11} - 2\rho {V_{sh}}^2(90^\circ) \\ c_{33} &= \rho {V_p}^2(0^\circ) \\ c_{44} &= \rho {V_{sh}}^2(0^\circ) \\ c_{13} &= -c_{44} + \\ &\quad \sqrt{4\rho^2 {V_p}^4(45^\circ) - 2\rho {V_p}^2(45^\circ)(c_{11} + c_{33} + 2c_{44}) + (c_{11} + c_{44})(c_{33} + c_{44})} \\ c_{66} &= \rho {V_{sh}}^2(90^\circ) \end{aligned}$$

in which all angles are measured from the symmetry axis (axis 3). The subscript *sh* (*sv*) represents shear waves that are polarized parallel (perpendicular) to the intersection lines between the bedding plane and the sample end surface. The last equation is in fact redundant because $c_{66} = (c_{11} - c_{12})/2$. c_{11} and c_{33} can be called the 'normal' stiffnesses and c_{66} and c_{44} the 'shear' stiffnesses. c_{12} and c_{13} are therefore combinations of normal and shear stiffnesses.

Elastic anisotropy is commonly described by a set of parameters defined using elastic constants (Thomsen, 1986; Vernik, 1992):

$$\begin{aligned} \epsilon &= \frac{c_{11} - c_{33}}{2c_{33}} \quad \text{(P-wave anisotropy)} \\ \gamma &= \frac{c_{66} - c_{44}}{2c_{44}} \quad \text{(S-wave anisotropy)} \end{aligned}$$

$$\delta_p = \frac{(c_{13}+c_{44})^2-(c_{33}-c_{44})^2}{2c_{33}(c_{33}-c_{44})}$$
$$\delta_{sv} = \frac{(c_{11}-c_{44})(c_{33}-c_{44})-(c_{13}+c_{44})^2}{2c_{44}(c_{33}-c_{44})}$$

The motivation for introducing the above parameters is that for weak anisotropy, expressions of phase velocities for qP-, qSV and SH waves can be simplified to

$$\begin{aligned} V_p(\theta) &\approx V_p(0^\circ)(1+2\delta_p\, sin^2(\theta))^{1/2} \quad \text{(small } \theta\text{)} \\ V_{sv}(\theta) &\approx V_{sv}(0^\circ)(1+2\delta_{sv}\, sin^2(\theta))^{1/2} \text{ (small } \theta\text{)} \\ V_{sh}(\theta) &= V_{sh}(0^\circ)(1+2\gamma\, sin^2(\theta))^{1/2} \quad \text{(exact).} \end{aligned}$$

B. Relationships between dry and saturated stiffnesses for a TI medium

The Brown-Korringa equation (Brown et al., 1975)

$$S^d_{ijkl} - S^s_{ijkl} = \frac{(S^d_{ij\alpha\alpha} - S^o_{ij\alpha\alpha})(S^d_{kl\alpha\alpha} - S^o_{kl\alpha\alpha})}{(S^d_{\alpha\alpha\beta\beta} - S^o_{\alpha\alpha\beta\beta}) + (\beta_{fl} - \beta_o)\phi} \tag{3.8}$$

provides a relationship between dry and saturated compliances for a general anisotropic medium. Here, the same relation is expressed in stiffnesses for a TI medium.

Let

$$\begin{aligned} \Delta s_1 &= (S^d_{11\alpha\alpha} - S^o_{11\alpha\alpha})/\sqrt{S_b} \\ \Delta s_3 &= (S^d_{33\alpha\alpha} - S^o_{33\alpha\alpha})/\sqrt{S_b} \end{aligned} \tag{3.9}$$

where $S_b = (S^d_{\alpha\alpha\beta\beta} - S^o_{\alpha\alpha\beta\beta}) + (\beta_{fl} - \beta_o)\phi$ (for meanings of the notations, refer to page 53) and use 2-index notations, Equation 3.8 for a TI medium becomes

$$\begin{aligned} s^s_{11} &= s^d_{11} - \Delta s_1^2 \\ s^s_{12} &= s^d_{12} - \Delta s_1^2 \\ s^s_{13} &= s^d_{13} - \Delta s_1 \Delta s_3 \\ s^s_{33} &= s^d_{33} - \Delta s_3^2 \\ s^s_{44} &= s^d_{44} \end{aligned}$$

The relationships between stiffness and compliances for hexagonal symmetry are given by (Auld, 1992)

$$c_{11} = \frac{1}{2}\left[\frac{s_{33}}{s} + \frac{1}{s_{11}-s_{12}}\right]$$

$$
\begin{aligned}
c_{12} &= \frac{1}{2}\left[\frac{s_{33}}{s} - \frac{1}{s_{11}-s_{12}}\right] \\
c_{13} &= -s_{13}/s \\
c_{33} &= (s_{11}+s_{12})/s \\
c_{44} &= 1/s_{44}
\end{aligned}
$$

where $s = s_{33}(s_{11}+s_{12}) - 2s_{13}^2$. By switching s and c, exactly the same equations can be used for conversions the other direction. As an example, $S_{11\alpha\alpha}$ and $S_{\alpha\alpha\beta\beta}$ in Equations 3.9 become

$$
\begin{aligned}
S_{11\alpha\alpha} &= (c_{33}-c_{13})/c \\
S_{\alpha\alpha\beta\beta} &= (c_{11}+c_{12}+2c_{33}-4c_{13})/c
\end{aligned}
$$

where $c = c_{33}(c_{11}+c_{12}) - 2(c_{13})^2$. So that Δs_1 and Δs_3 are parameters of dry rock and mineral properties only.

Changes in elastic stiffnesses from dry to fully saturated state, $\Delta c_{ij} = c_{ij}^s - c_{ij}^d$, can now be found and expressed in dry properties (the superscript d is dropped from all symbols on the right-hand side and Δc on the left-hand side) and fluid compressibility

$$
\begin{aligned}
\Delta c_{11}(1-\Delta c) &= \begin{pmatrix} \Delta s1 & \Delta s2 \end{pmatrix} \begin{pmatrix} (c_{11}+c_{12})^2 & c_{13}(c_{11}+c_{12}) \\ c_{13}(c_{11}+c_{12}) & c_{13}^2 \end{pmatrix} \begin{pmatrix} \Delta s1 \\ \Delta s2 \end{pmatrix} \\
\Delta c_{13}(1-\Delta c) &= \begin{pmatrix} \Delta s1 & \Delta s2 \end{pmatrix} \begin{pmatrix} 2c_{13}(c_{11}+c_{12}) & c_{13}^2+(c_{11}+c_{12})/2 \\ c_{13}^2+(c_{11}+c_{12})/2 & c_{13}c_{33} \end{pmatrix} \begin{pmatrix} \Delta s1 \\ \Delta s2 \end{pmatrix} \\
\Delta c_{33}(1-\Delta c) &= \begin{pmatrix} \Delta s1 & \Delta s2 \end{pmatrix} \begin{pmatrix} 4c_{13}^2 & 2c_{13}c_{33} \\ 2c_{13}c_{33} & c_{33}^2 \end{pmatrix} \begin{pmatrix} \Delta s1 \\ \Delta s2 \end{pmatrix}
\end{aligned}
$$

where $\Delta c = c_{33}\Delta s_3^2 + 2(c_{11}+c_{12})\Delta s_1^2 + 4c_{13}\Delta s_1 \Delta s_3$.

Because of the positive semidefinitenss of the right hand side, it follows that $\Delta c_{11}(1-\Delta c) \geq 0$ and $\Delta c_{33}(1-\Delta c) \geq 0$. However, the sign for $\Delta c_{13}(1-\Delta c) \geq 0$ is uncertain. Finally, the shear stiffness c_{44} and c_{66} remain unchanged upon saturation, i.e., $\Delta c_{44} = \Delta c_{66} \equiv 0$.

C. Major rock types in the Monterey formation

Definitions and short descriptions for the major rock types in the Monterey formation are available in Isaacs (1980, 1981) and Dunham et al. (1990). For convenience, a simplified version of the definitions in Dunham et al. (1990) is given below. Siliceous shale is not listed under shale because it is more brittle than the other two.

Chert: a rock with a vitreous luster and a hardness greater than 6.0. It occurs in both the opal-CT and quartz silica phases and contains greater than 90 percent biogenic silica by weight. Chert is a brittle rock that often contains natural fracture.

Dolomite: a dense, solid, non-fissil rock with a scratch hardness of 3 to 4. All of the dolomite beds in the Union-Leroy 51-18 core contain some degree of silica or detrital-clay contamination (10 to 40 percent).

Porcelanite: a rock without a vitreous luster and a hardness about 5.0. It occurs in both the opal-CT and quartz silica phases and is a highly siliceous rock. It is brittle and often contains natural fractures. The main differences between porcelanite and chert are fracture style, rock-hardness, and matte luster versus vitreous luster.

Siliceous Shale: a brittle-ductile rock that often contains natural fracture. It is highly siliceous but it invariably has a higher detrital-clay content (from 20 to 25 weight-percent) than chert or porcelanite.

Shale: a very soft rock that has well-developed fissility and does not contain natural fractures. Most shales from Monterey formation contain greater than 25 weight-percent detrital clay. The matrix porosity is usually higher than other lithologies. There are two typical shale types in the Monterey formation:

Phosphatic shale: characterized by the presence of thin layers and ellipsoidal nodules of tan-colored carbonate fluorapatite. Locally, the concentration of these layers and nodules becomes so great that the rock itself becomes a phosphorite.

Organic shale: referring to its unusually high content of amorphous kerogen. Organic shales in the Union-Leroy 51-18 core have total organic carbon (TOC) content in the range from 10 to 20%, which translates into roughly 25 to 45% of kerogen by volume.

D. Original and modeled well logs of Union-Leroy 51-18 well

The comprehensive log plots that follow contain the original caliper, gamma ray (track 1), density (track 2), and sonic logs (track 3) provided by Unocal Company, along with the lithology description (track 5) based on Dunham et al. (1990), and the sonic responses (track 4) modeled from sparse core measurements in this study. A 12 ft depth shift is applied to the original logs relative to the lithology column. However, nonuniform cable stretching prevents a complete matching between the lithology column and well logs.

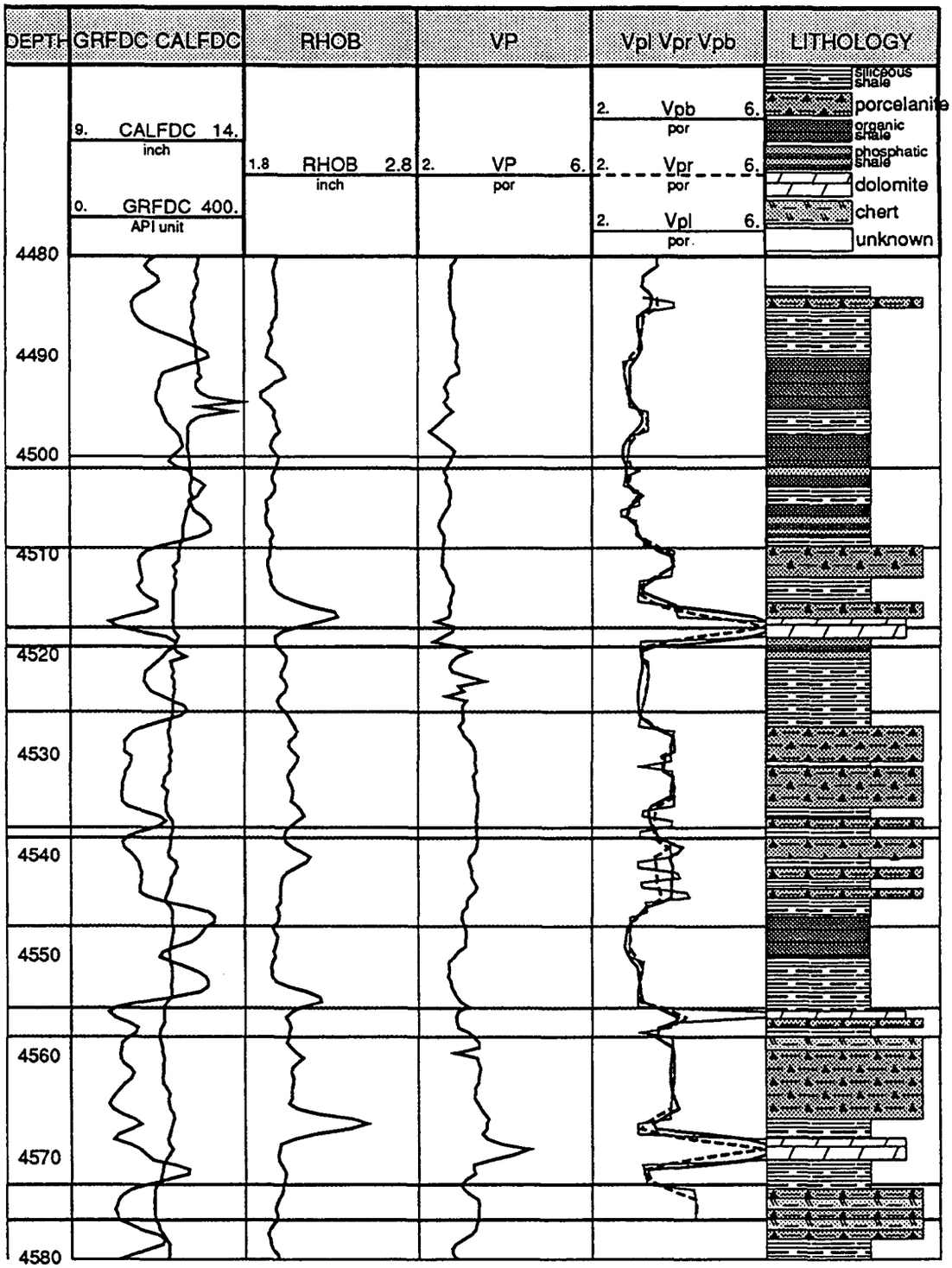

Log plotting software designed by X. (Frank) Liu 1993

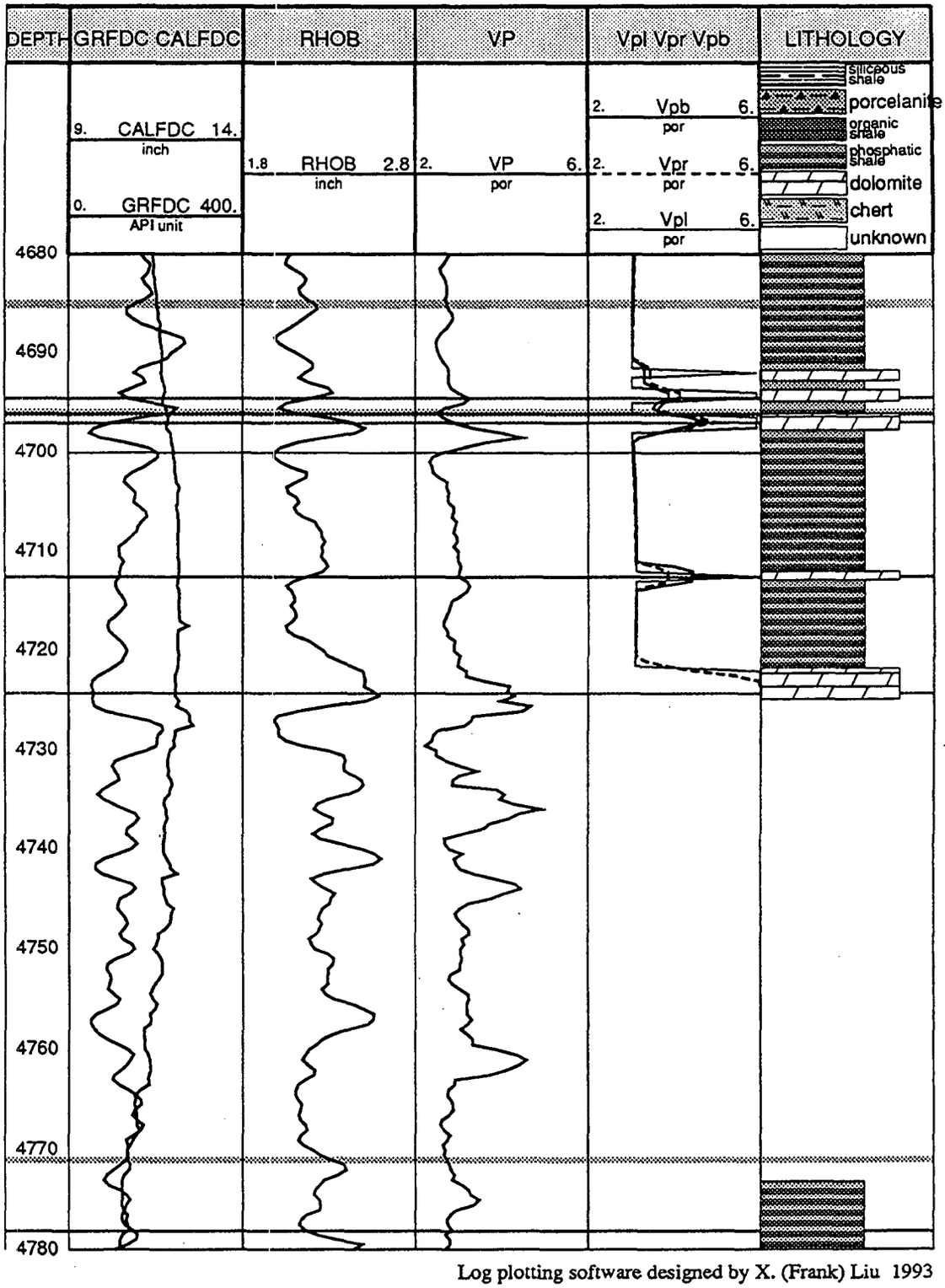

Log plotting software designed by X. (Frank) Liu 1993

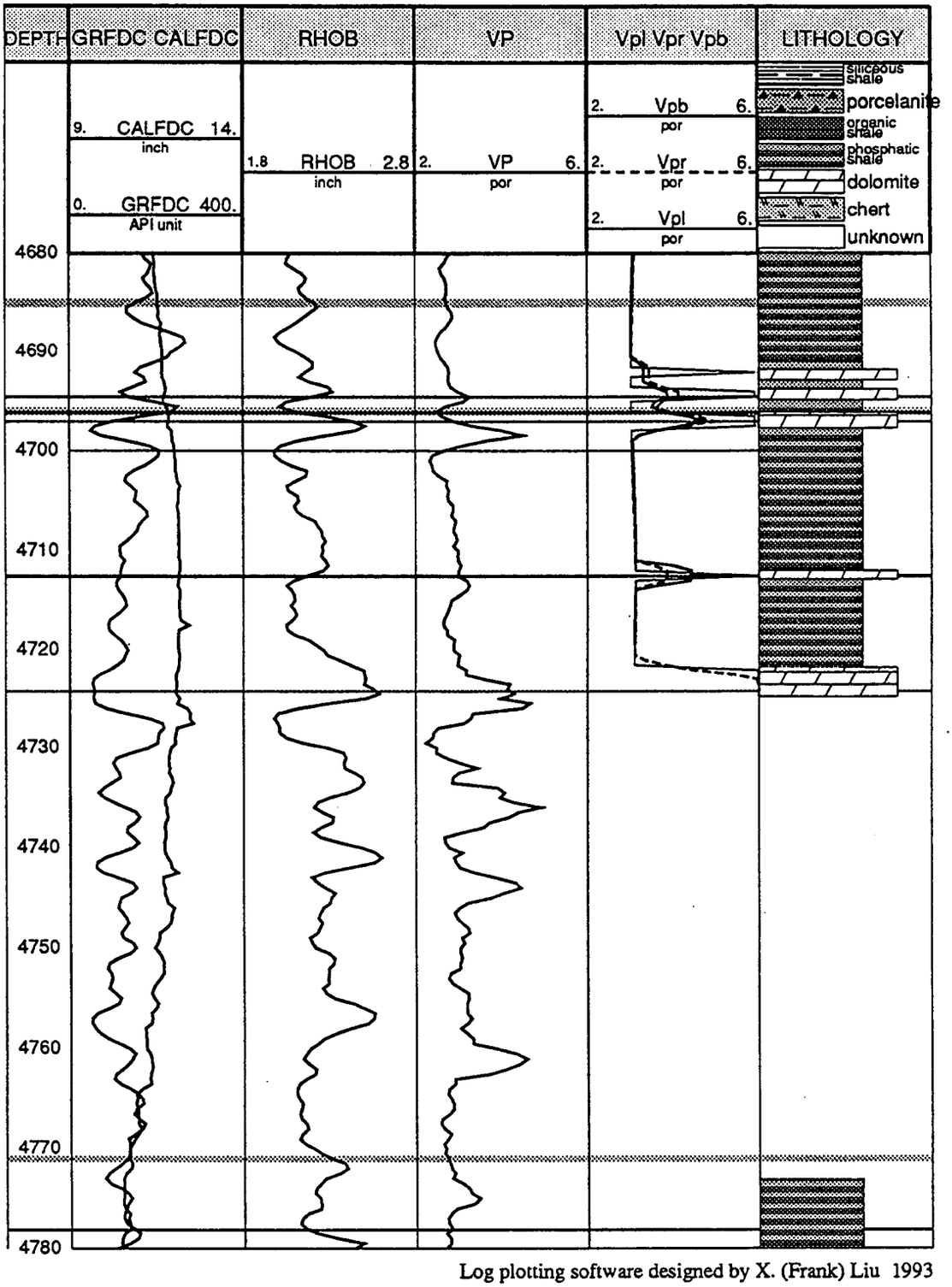

Log plotting software designed by X. (Frank) Liu 1993

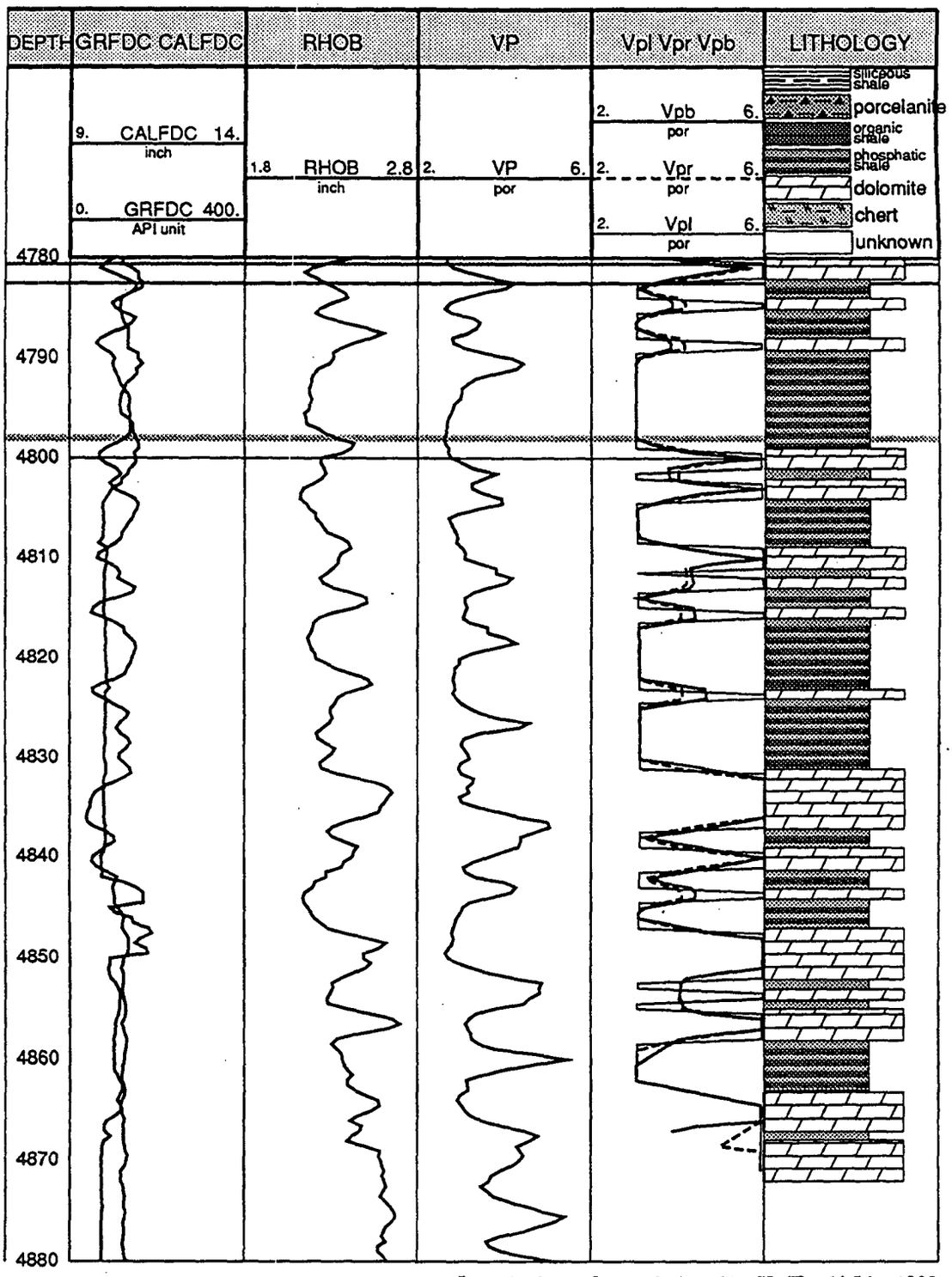

Log plotting software designed by X. (Frank) Liu 1993

References

Auld, B. A., 1990, Acoustic fields and waves in solids, v. I, II, Robert E. Krieger Publ. Co., Florida.

Backus, G. E., 1962, Long-wave elastic anisotropy produced by horizontal layering: J. Geophys. Res., **67**, 4427-4440.

Banik, N. C., 1984, Velocity anisotropy of shales and depth estimation in the North Sea basin: Geophysics, **49**, 1411-1419.

Berryman, J. G., 1994, Mixture theories for rock properties, *in press.*

Biot, M. A., 1956, Theory of propagation of elastic waves in a fluid-saturated porous solid. II. Higher-frequency range: J. Acoust. Soc. Am., **28**, 179-191.

Birch, F., 1962, The velocity of compressional waves in rocks to 10 kilobars: J. Geophys. Res., **66**, 2199-2224.

Brown, R. and J. Korringa, 1975, On the dependence of the elastic properties of a porous rock on the compressibility of the pore fluid: Geophysics, **40**, 608-616.

Dunham, J. B. and M. L. Cotton-Thornton, 1990, Lithology of the Monterey formation in the western Santa Maria valley field, Santa Maria Basin, California: SEPM Core Workshop, **14**, 202-239.

Dvorkin, J. and A. Nur, 1993, Dynamic poroelasticity: A unified model with the squirt and the Biot mechanisms: Geophysics, **58**, 524-533.

Gassmann, F., 1951, Uber die elastizitat poroser medien: Vier. der Natur Gesellschaft, **96**, 1-23.

Hashin, Z. and S. Shtrikman, 1963, A variational approach to the theory of the elastic behaviour of multiphase materials: J. Mech. Phys. Solids, **11**, 127-140.

Hill, R., 1952, The elastic behaviour of a crystalline aggregate: Proc., Phys. Soc. London, Ser. A, **65**, 349-354.

Isaacs, C. M., 1981, Outline of diagenesis in the Monterey formation examined laterally along the Santa Barbara coast, California: in Isaacs, C. M., ed., Guide to the Monterey formation in the California Coastal Area, Ventura To San Luis Obispo: Pac. Sect., Am. Assoc. Petr. Gelo. Publication, 25-38.

Isaacs, C. M., 1984, The Monterey: key to offshore California boom: Oil and Gas Journal, **82**, 75-81.

Isaacs, C. M., 1986, Guide to the Monterey Formation in the coastal California area, Ventura-San Luis Obispo, Pacific Section: AAPG, **52**, 91.

Israelachvili, J. N. and P. M. McGuiggan, 1988, Forces between surfaces in liquids: Science, **12**, 795-799.

Johnston, D. H., 1987, Physical properties of shale at temperature and pressure: Geophysics, **52**, 1392-1401.

Jones, L. E. A. and H. F. Wang, 1981, Ultrasonic velocities in Cretaceous shales from the Williston Basin: Geophysics, **46**, 288-297.

Kaarsberg, E., 1976, Relationships among the elastic properties, densities, porosities and permeabilities of a set of non-calcareous shales: EOS (Am. Geophys. Union Trans.), **57**, 597.

Lo, T. W., K. B. Coyner, and M. N. Toksoz, 1986, Experimental determination of elastic anisotropy of Berea sandstone, Chicopee shale, and Chelmsford granite: Geophysics, **51**, 164-171.

Mavko, G. and D. Jizba, 1991, Estimating grain-scale fluid effects on velocity dispersion in rocks: Geophysics, **56**, 1940-1949.

Mavko, G. and A. Nur, 1975, Melt squirt in the asthenosphere: J. Geophys. Res., **80**, 1444-1448.

Morris, C. E., 1978, Elastic constants of oil shale: Los Alamos Sci. Lab., **7164**, 21-28.

Mukerji, T. and G. Mavko, 1994, Pore fluid effects on seismic velocity in anisotropic rocks: Geophysics, **59**, 233-244.

Nur, A., 1991, Critical porosity, elastic bounds, and seismic velocities in rocks: Technical programme and abstract for papers, EAEG, **53**, 248-249.

O'Connell, R. J. and B. Budiansky, 1977, Viscoelastic properties of fluid saturated cracked solids: J. Geophys. Res, **82**, 5719-5736.

Passey, Q. R., S. Creaney, J. B. Kulla, F. J. Moretti, and J. D. Stroud, 1990, A practical model for organic richness from porosity and resistivity logs: AAPG Bulletin, **74**, 1777-1794.

Roy, B., 1988, Seismic expressions of Monterey Formation diagenesis; examples from offshore California: AAPG Bulletin, **72**, 393.

Sadler, R. K., 1990, The relationship of lithology and tectonics to fracturing in the Monterey formation, Point Arguello field, offshore California: SEPM Core Workshop, **14**, 245-269.

Seriff, A. J., 1985, Anisotropy, shear waves, and shales: Geophysics, **50**, 367-368.

Thomsen, L., 1986, Weak elastic anisotropy: Geophysics, **51**, 1954-1966.

Tosaya, C., 1982, Acoustical properties of clay-bearing rocks, Ph.D dissertation, Stanford University.

van Olphen, H., 1963, Clay colloid chemistry, John Wiley & Sons, New York, 318p.

Vernik, L. and A. Nur, 1992, Ultrasonic velocity and anisotropy of hydrocarbon source-rocks: Geophysics, **5**, 727-735.

Vernik, L., 1993, Microcrack-induced versus intrinsic elastic anisotropy in mature HC-source shales: Geophysics, **58**, 1703-1706.

Vernik, L., X. Liu, and A. Nur, 1994, Effect of kerogen on velocity anisotropy in source rocks: SEG extended abs. (accepted), Los Angeles.

White, J. E., 1965, Seismic Waves: Radiation, Transmission, and Attenuation, McGraw-Hill Book co.

White, J. E., L. Martineau-Nicoletis, and C. Monash, 1983, Measured anisotropy in Pierre shale: Geophys. Prosp., **31**, 709-725.

Winterstein, D. F. and B. N. P. Paulsson, 1990, Velocity anisotropy in shale determined from crosshole seismic and vertical seismic profile data: Geophysics, **55**, 470-479.

Yu, G. K., K. Vozoff, and D. W. Durney, The influence of confining pressure and water saturation on dynamic elastic properties of some Permian coals: Geophysics, **1**, 30-38.

Chapter 4

Reservoir properties of carbonates

Abstract

The role of linking rock physics and geostatistics in reservoir characterization is shown through the study of a carbonate reservoir. Rock physics provides the interrelationships between reservoir properties (porosity, permeability) and field measurables (seismic velocity, gamma ray intensity, etc.). It also provides an insight into the inevitable scatter or variability in any such interrelationships. One major cause for the scatter is the averaging or scale effect, as shown from measurements at core, logging, and crosswell scales. Geostatistics is used to map reservoir properties in regions with no direct measurements. With stochastic simulation, the resolution in crosswell seismic survey is enhanced globally. Also, geophysical data of a different scale and nature are effectively integrated.

For carbonate rocks formed of dolomite, siliciclastics, and anhydrite, the velocity-porosity relationship is found to be $V_p = V_o - 0.084\phi$ (ϕ is in percentage), where V_o is the mineral matrix velocity (see Section 4.2 for its values). In situ, porosity can be predicted from velocity if lithology is known. Gamma ray intensity can supply partial information of lithology. However, when spectral (K^{40}) instead of total gamma ray intensity is used, the prediction error can be greatly reduced. Permeability can be estimated from porosity by $\log_{10} k = 0.35\phi - 3.0\sqrt{1 + 0.25\sin^2\theta}$ (ϕ in percentage, k in mD, θ is the angle relative to the bedding direction). Finally, there is a linear relationship between acoustic impedance and velocity in carbonate rocks.

4.1 Introduction

The reservoir properties (porosity, permeability) between wells are important to reservoir development and enhanced oil recovery. To model the spatial distribution of reservoir properties we need to first find the interrelationships between the reservoir properties and field measurables such as velocity, gamma ray intensity, and then map their spatial distributions using all available measurements. With the recent advances in crosswell seismic technology, it is now possible to have the interwell velocity distribution (tomogram) for mapping interwell reservoir properties in addition to the sonic logs and core measurements at scattered well locations.

In relating different measurements of rock properties, two problems frequently arise. First, the measurements are often of different nature (e.g., fluid flow versus elastic or nuclear properties) and have quite different volume supports (e.g., core measurements versus well logs or seismic survey). Second, the relationships may not be represented by simple equations, and scatter (deviations from modeled relations) always exists. There can be several causes for the scatter. The physical link among different rock properties may be intrinsically weak. For the same rock property, measurements on different support volumes usually generate different results. Solutions to these problems require both understanding of the physical principles behind any petrophysical relationship and the appropriate statistical models to account for change of support. To achieve this, a joint effort from different disciplines is needed.

This report presents a study of the petrophysical properties of a carbonate reservoir using both rock physics and geostatistics. The study area and the study goals are described below.

The field under study[1] is shown schematically in Figure 4.1. It includes two cored wells (A and B), 8 logged wells (1 through 6, A and B) that form a double five-spot, and two cross sections (the shaded areas of 1-5 and 3-5) with crosswell seismic surveys. The geophysical measurements available in this field are listed in Table 4.1 and will be described more specifically in the following sections. There are three goals to this study. First, we want to find for carbonate rocks the petrophysical relationships between reservoir properties and field measurables and between different field measurables. Second, based on comparison between measurements made on different supports we want to understand the causes for scatter in inference, the support or averaging effect being the most important one. This analysis should provide clues

[1]The original data for this study belongs to Amoco Production Company. For proprietary reasons, all identification (field name, well names, and formation depths have been omitted intentionally.

support	wells	measurements
core	A, B	ρ, ϕ, k
plug	A, B	ρ, ϕ, k, V_p, V_s
logging	all wells	sonic (V_p), gamma ray (GR)
crosswell	1-5, 3-5	seismic velocity

Table 4.1: A list of the geophysical measurements in the study field showing the type and support of measurements. Notations in the table: ρ - density, ϕ - porosity, k - permeability, $V_{p,s}$ - P- and S-wave velocities.

for improving the accuracy of inference through improved geophysical measurements. Finally, we want to show how to globally undo the averaging (support) effect using stochastic simulation techniques and integrate geophysical data made on different supports. Section 2 presents a petrophysical study of the relationships between porosity, velocity and gamma ray intensity, between porosity and permeability, and between velocity and acoustic impedance, all based on the laboratory plug support and scale. In Section 3, the support effect of different geophysical measurements is analyzed using laboratory core measurements, well logs, and crosswell seismic data. For the mapping of interwell reservoir properties, stochastic simulation by simulated annealing is used to enhance the resolution of crosswell seismic data by integrating data obtained from different support (Section 4). The effectiveness of simulated annealing in honoring the various conditioning data is discussed from the comparison between simulation results and validation data.

4.2 Petrophysical relations

The petrophysical analysis here proposed aims at finding the relations between reservoir properties (porosity, permeability) and field measurables (velocity, gamma ray intensity, etc.). Such relations are used in log calibration (e.g. calculating porosity from sonic log) and in the geostatistical inference of interwell reservoir properties. The lithology and mineralogy of carbonate rocks are first described. Next, modeling based on effective medium theory is used to obtain the mineral matrix properties for a three-component system which are then compared with laboratory measurements. The field application of velocity-porosity relation is given afterwards. Finally, the interrelationships of other petrophysical properties are analyzed.

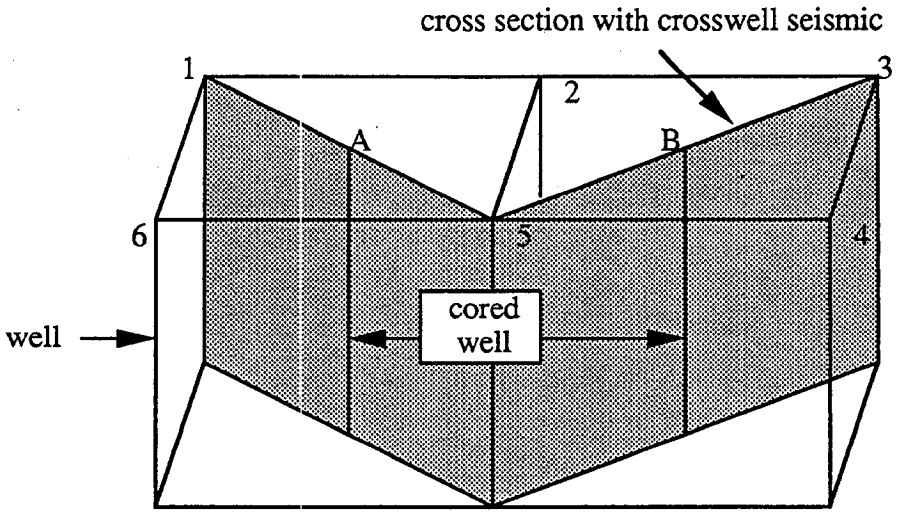

Figure 4.1: Well geometry of the carbonate reservoir under this study.

4.2.1 Lithology and mineralogy

Carbonate (or carbonate-siliciclastic) rock samples[2] for this study come from two cored wells (A and B in Figure 4.1) of a western Texas oil field located on the eastern edge of the Central Basin Platform. Most samples belong to the Permian Grayburg formation, which has a shoaling upward sequence formed during reflooding of the exposed San Andres carbonate platform. A few sandy samples belong to the bottom of the supratidal sediments of the Queen formation. In the open shelf deposits, the most abundant mineralogy components in the samples are carbonate (dolomitized), siliciclastic sediments (quartz, feldspar, and clay), and evaporite (anhydrite). The porosity types, as studied from the nearby McElroy field (Harris and Walker, 1988), include interparticle, intercrystalline, and micro-vuggy. Based on approximate volumetric compositions, the lithology (rock type) can be divided into dolomite, anhydritic dolomite, silty dolomite, dolomitic siltstone, anhydritic siltstone, and siltstone, as shown in Figure 4.2.

4.2.2 Velocity-porosity relationship

A velocity-porosity relationship is needed for estimating formation porosity from sonic logs. Such relationships have been studied mostly in clean or shaly sandstones (Wyllie, 1956; Han, 1986; Vernik, 1992) but only a few studies exist (Rafavich, 1983;

[2]Selected samples represent different lithologies, a wide range of porosity, grain or pore size, porosity type, three directions (parallel, 45°, and perpendicular to bedding), and some special textural features of the rocks such as stylolite.

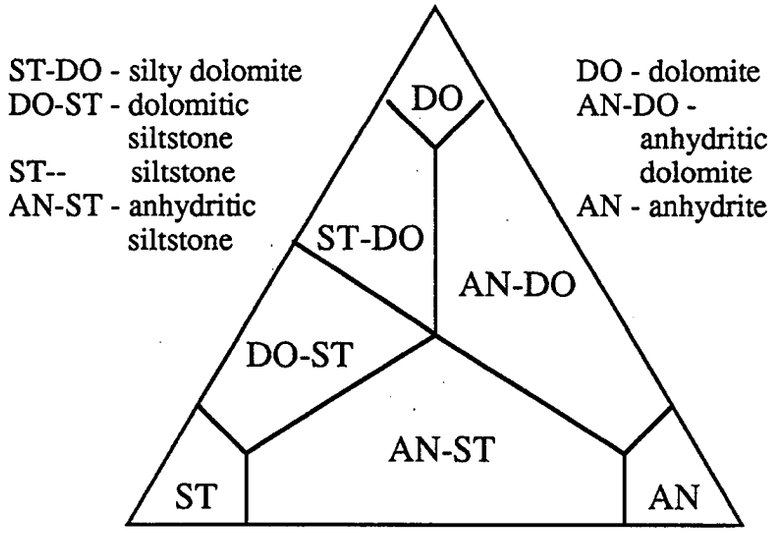

Figure 4.2: Ternary diagram for lithologies of carbonate rocks consisting of dolomite, anhydrite, and siliciclastics (quartz, clay, and feldspars).

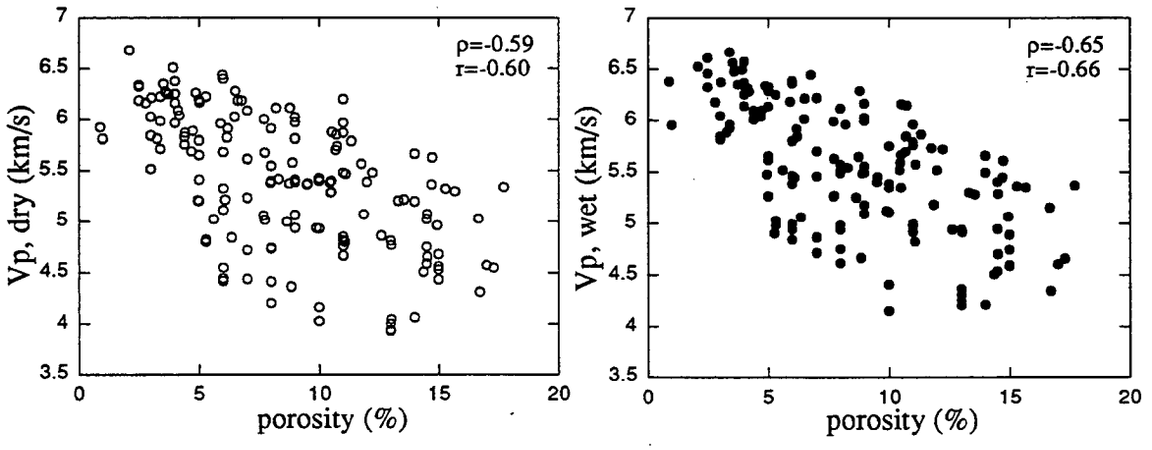

Figure 4.3: Laboratory-measured ultrasonic P-wave velocities versus porosity in both dry (left) and saturated (right) rocks on the plug support.

component	density (g/cm^3)	V_p (km/s)	V_s (km/s)	V_p/V_s
dolomite	2.87	6.93	4.01	1.73
anhydrite	2.96	6.04	3.05	1.98
siliciclastics	2.65	5.44	3.50	1.54

Table 4.2: Typical velocity and density values for three constituent components in carbonate rocks. Properties of quartz are used for the class of siliciclastics including quartz, clay, and feldspar.

Wilkens, 1984) for carbonate rocks. Besides, these studies are mostly empirical and no analysis of how to obtain matrix velocity or of how to obtain the lithology from field measurements has been sugested.

In Figure 4.3, the crossplots of velocity (dry and wet) versus porosity across all lithologies found in the field show poor correlations ($\rho \sim 0.6$ for both dry and saturated samples). The reason for such weak correlation is that the elastic properties of rocks depend on the lithology as well as on the porosity of rocks.

In order to analyze the effect of lithology on the velocities of rocks, the mineral matrix of the carbonate rocks in this field is treated as a three-component system of dolomite, anhydrite, and siliciclastics, as supported by the FTIR mineralogy analysis. The three components have different elastic properties, as shown in Table 4.2. The properties of quartz are used to represent those of siliciclastics since quartz, feldspar, and clay have similar average velocity and density values. Since the exact geometry and spatial distribution of these components in rocks are unknown, the upper and lower limits for the elastic properties (called elastic bounds in rock physics) can be found given the volumetric combinations of the three components. The arithmetic average of the properties corresponding to the higher and lower bounds can then be used as an estimate of the mineral matrix property. Hashin-Shtrikman equations (Hashin and Shtrikman, 1963, see appendix) are used for calculating the upper and lower bounds. Figure 4.4 plots the calculation results of velocities (as contour lines) for the upper and lower bounds (dash lines) as well as the average of the two (solid lines).

By superimposing Figure 4.4 (modeling results for V_p, V_s, and V_p/V_s) and Figure 4.2 (lithology division), we can read a first approximation of the matrix velocities of different rock types. V_p is highest for dolomite, lowest for siltstone, and intermediate (in decreasing order) for anhydritic dolomite, silty dolomite, dolomitic or anhydritic

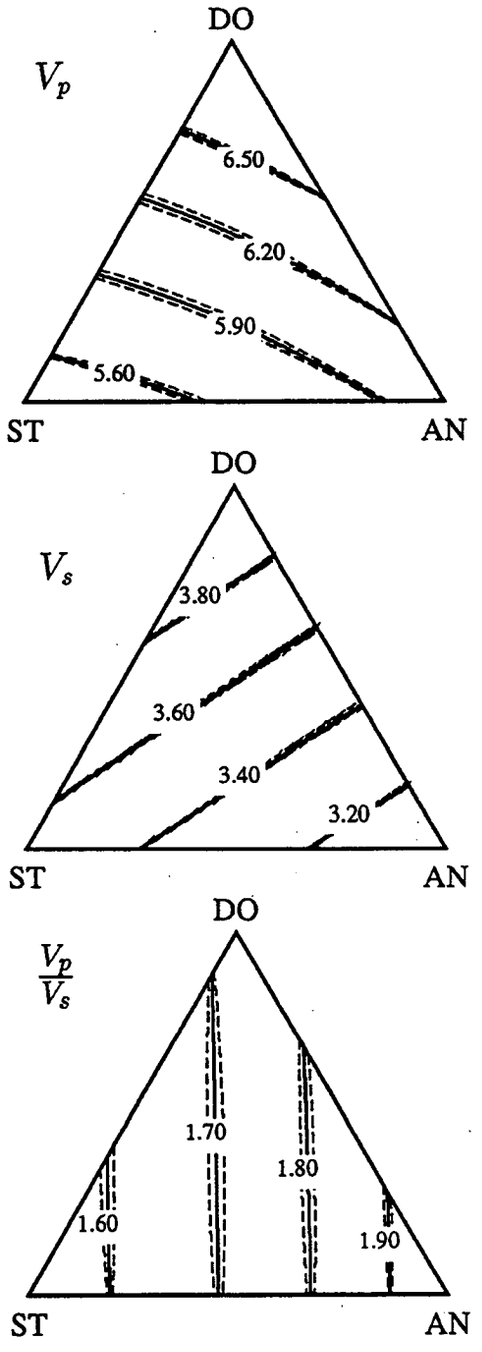

Figure 4.4: Modeled P- (top figure) and S-wave (middle figure) velocities and V_p/V_s ratio (bottom figure) plotted as contour lines for mineral matrix consisting of dolomite (DO), anhydrite (AN), and siliciclastics (ST).

siltstone, and siltstone. For V_s, the roles between anhydrite and siliciclastics (quartz) are interchanged. This is because siliciclastics have higher V_p but lower V_s than that of anhydrite. The overall trends are the following: both V_p and V_s are higher for very dolomitic rocks; V_p decreases as the rock becomes more silty (anhydritic rocks have intermediate velocities), and V_s decreases as the rock becomes more anhydritic (silty rocks have intermediate velocities). Therefore, at least theoretically, by having both V_p and V_s, the volume fractions of the three components (therefore of the rock types) can be determined. For the V_p/V_s ratio, the modeling shows that the more anhydritic rocks should have higher values than the more dolomitic or silty rocks. Since there is no S-wave sonic log in the two cored wells, more discussions are made on the P-wave velocities in the following.

Figure 4.5 shows the laboratory measured P-wave velocities of dry (circle) and saturated (dot) samples plotted against porosity. For each rock type, the intercept of the trending line with velocity axis is the approximate matrix velocity for that rock type. For dry samples, the values are 6.85 km/s for dolomite, 6.62 km/s for anhydritic dolomite, 6.20 km/s for silty dolomite, 5.64 for dolomitic or anhydritic siltstone. We see that except for siltstone, the matrix velocities from the model estimate and from the experiment agree very well. The lower experimental value for siltstone is probably resulting from altered feldspar and poor consolidation. The result for velocity ratio V_p/V_s is shown in Figure 4.7 (a) by slopes of V_p versus V_s. We see that more anhydritic rocks (AN-DO and AN-ST) have indeed steeper slopes, as predicted by theory.

The dependence of velocity on porosity can be obtained from the experimental measurements on plugs. It can be seen from Figure 4.5 that for different rock types, the slopes of velocity variation versus porosity are approximately the same, around -0.084 km/s per percent of porosity increase for dry samples. The velocity-porosity relation, given the matrix velocity V_{p0}, is $V_p = V_{p0} - 0.084\phi$. For saturated rocks, the slopes vary slightly while the mineral velocities do not. The velocity-porosity relationship for saturated rocks is found to be: $V_p = V_{p0} - 0.08\phi$. Therefore, to estimate the porosity of a rock, velocities of both the matrix mineral and the porous rock are needed.

4.2.3 Applications to well logging

The above analysis of the velocity-porosity relation is based on knowledge of the rock type. In situ, rock type proportions must be inferred from other physical measurements. In siliciclastic carbonate, K^{40} (1.46 MeV) in potassium feldspar gives out the strongest (in count) natural gamma ray radiation because of its abundance. So

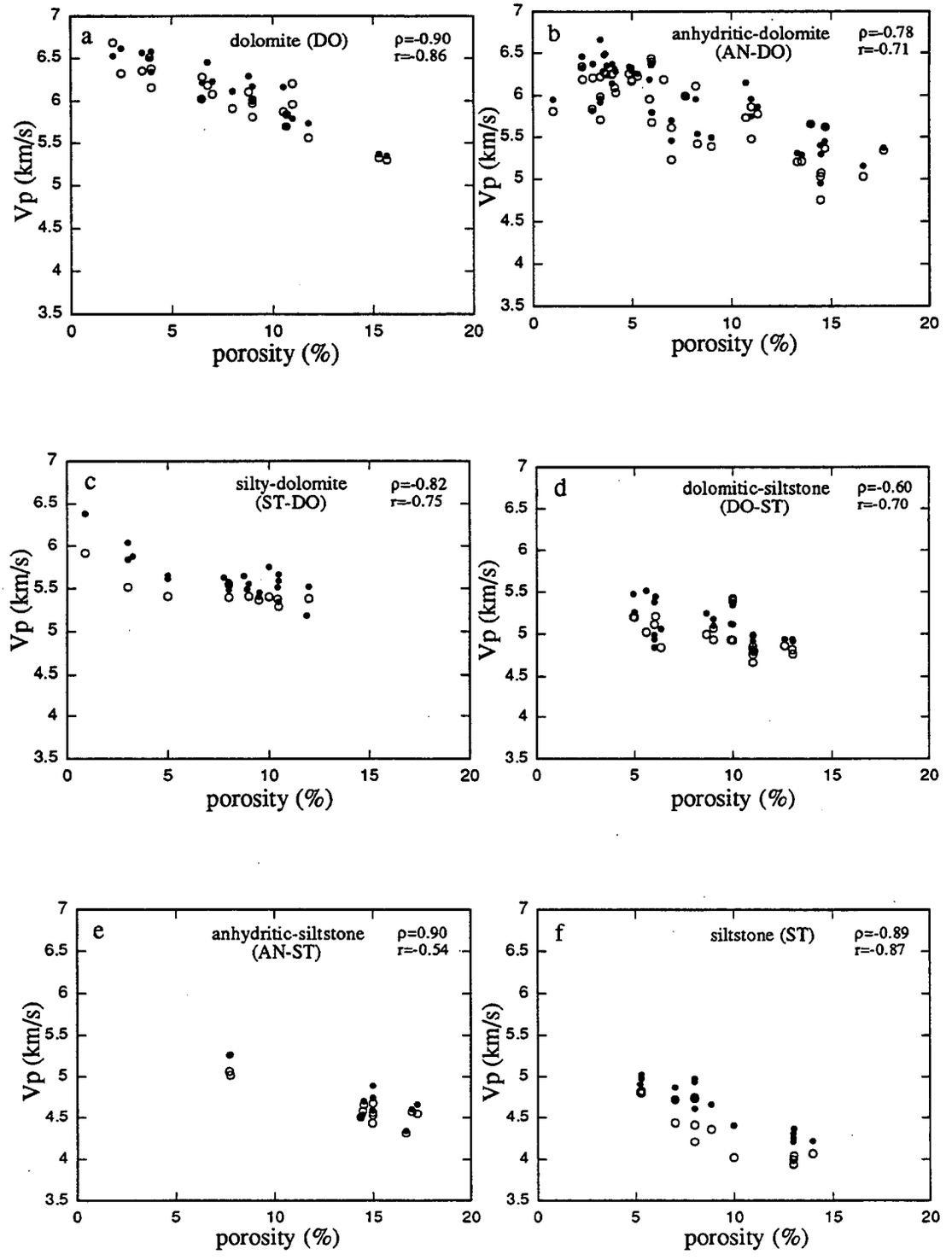

Figure 4.5: Measured P-wave velocity of dry (in circles) and saturated (in dots) samples grouped by rock types.

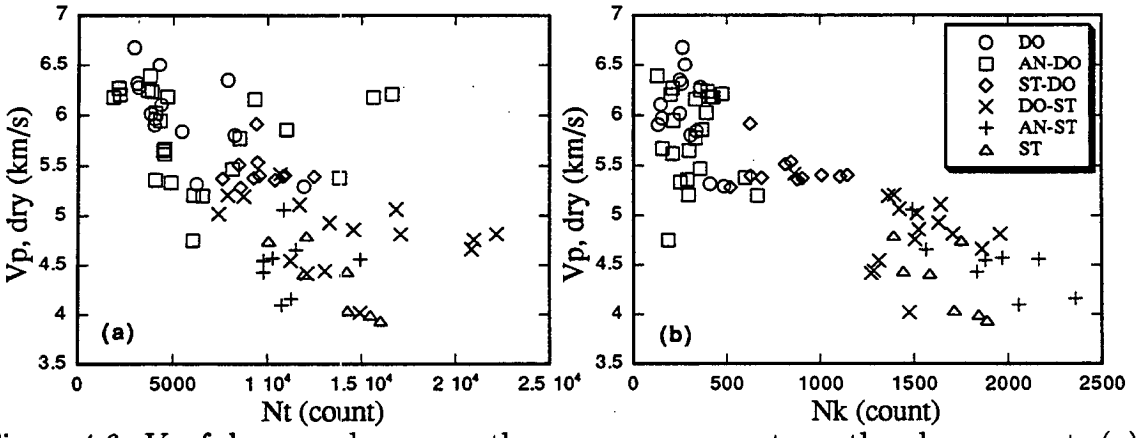

Figure 4.6: V_p of dry samples versus the gamma ray counts on the plug support: (a) total count N_t; (b) K^{40} count N_k.

the measured gamma ray (GR) intensity can be used to infer the "siltiness" of rock. This, when calibrated, allows an estimation of the matrix velocity. However, the more commonly-used total GR log may be less accurate because of complications arising from U^{235} (1.76 MeV) associated with organic matter in the stylolite abundant in the Grayburg formation. To illustrate this, Figure 4.6 shows V_p plotted against the total GR count N_t (a) and K^{40} count N_k (b) measured on plugs in shielded condition. The $V_p - N_k$ plot shows clearly two separated groups of more siliciclastic and more dolomitic or anhydritic samples; it also shows that the higher the GR count, the lower the V_p.

Linear correlations are performed among velocity V (both P and S in dry or saturated rocks), porosity ϕ, and GR count N_t or N_k using porosity and/or GR count as the predictor(s). Three types of correlations are considered: using only ϕ; using N_t in addition to ϕ; and using ϕ and N_k instead of N_t. The results are summarized below (ρ is the linear correlation coefficient):

1. $V = V_0 - a\,\phi$

dry:	$V_p = 5.98 - 0.095\phi$	$\rho = 0.59$
wet:	$V_p = 6.18 - 0.101\phi$	$\rho = 0.65$
dry:	$V_s = 3.49 - 0.0445\phi$	$\rho = 0.62$
wet:	$V_s = 3.44 - 0.0441\phi$	$\rho = 0.58$

2. $V = V_0 - a\,\phi - b\,N_t$

dry:	$V_p = 6.57 - 0.0757\phi - 8 \times 10^{-5} N_t$	$\rho = 0.80$
wet:	$V_p = 6.68 - 0.0843\phi - 6.9 \times 10^{-5} N_t$	$\rho = 0.81$
dry:	$V_s = 3.73 - 0.0371\phi - 3.1 \times 10^{-5} N_t$	$\rho = 0.78$
wet:	$V_s = 3.66 - 0.037\phi - 2.9 \times 10^{-5} N_t$	$\rho = 0.72$

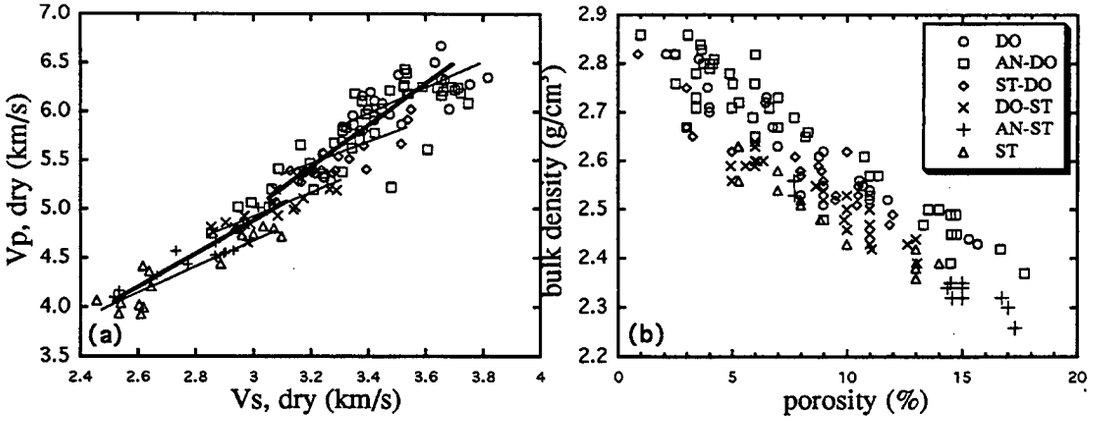

Figure 4.7: (a) V_p versus V_s in dry samples; (b) bulk density of dry rock versus porosity. All measurements are on the plug support.

3. $V = V_0 - a\,\phi - b\,N_k$

dry:	$V_p = 6.39 - 0.0576\phi - 7.59 \times 10^{-4} N_k$	$\rho = 0.90$
wet:	$V_p = 6.55 - 0.0664\phi - 7 \times 10^{-4} N_k$	$\rho = 0.92$
dry:	$V_s = 3.66 - 0.0296\phi - 3.06 \times 10^{-4} N_k$	$\rho = 0.87$
wet:	$V_s = 3.61 - 0.0286\phi - 3.15 \times 10^{-4} N_k$	$\rho = 0.84$

It can be seen that the linear correlation coefficient ρ increases from around 0.6 to 0.8 (except the V_s of wet rocks) when N_t is used in addition to ϕ in the linear regression. If N_k instead of N_t is used, ρ can be raised further from 0.8 to 0.9. This is reflected in the error defined as $(V_{pred} - V_{meas})/V_{meas}$ (V_{pred} = velocities predicted from the linear regression equation; V_{meas} = measured velocities) plotted against N_t (horizontal axis), as shown for V_p in Figure 4.8. When V_p is predicted from ϕ only (a), the error increases with N_t (i.e., there is a trend). When N_t is used in addition to ϕ (b), most of the trend is removed but the absolute error still increases with N_k. In (c), when N_t is replaced with N_k, the error is greatly reduced. The reasons that the residual error increases with either N_t or N_k are 1) only feldspar contains K^{40} while quartz and most clay minerals do not; 2) in silty rocks, dolomite can increase the velocity more than anhydrite does; however, the relative volumes of dolomite or anhydrite cannot be informed by the GR count.

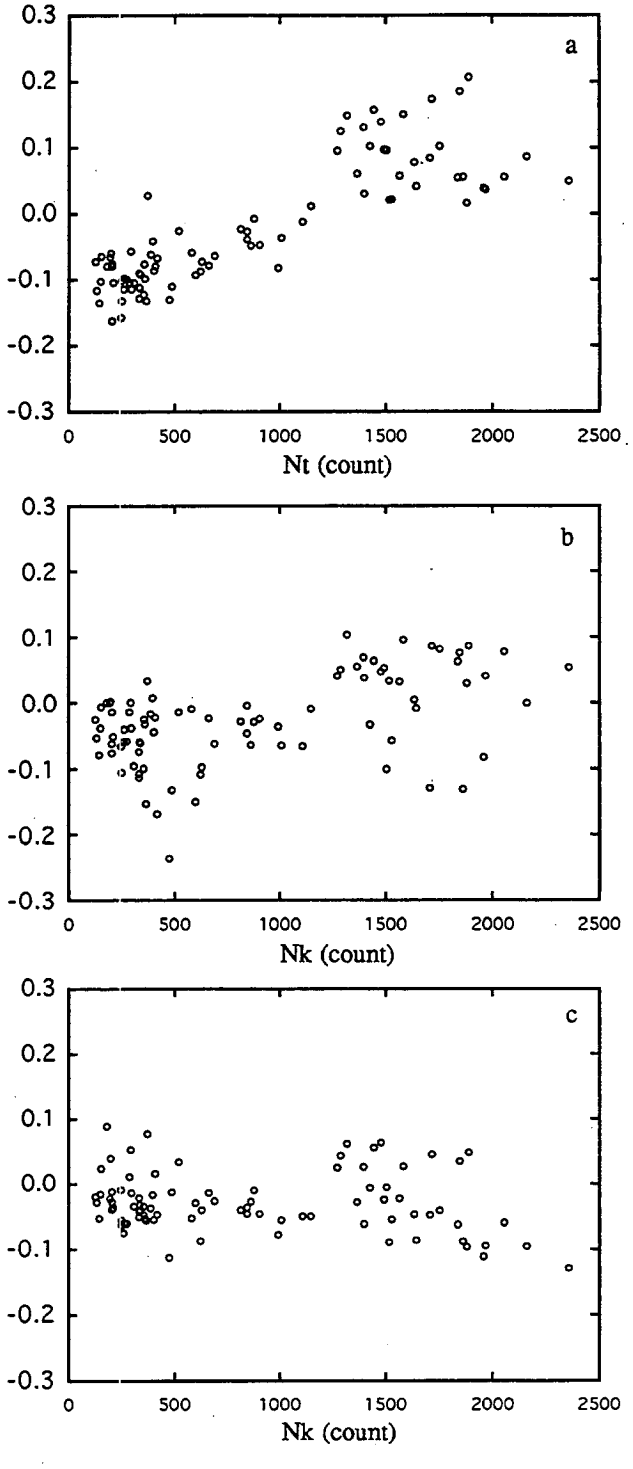

Figure 4.8: Error (vertical axis, defined as $(V_{pred} - V_{meas})/V_{meas}$) in predicted V_p using linear regressions: (a) $V = V_0 - a\,\phi$; (b) $V = V_0 - a\,\phi - b\,N_t$; (c) $V = V_0 - a\,\phi - b\,N_k$.

4.2.4 Other petrophysical relationships

In addition to the above $V - \phi - GR$ relationship, other petrophysical properties are also analyzed. Such relations are needed in reservoir characterization studies. For example, the porosity-permeability relation is needed to calculate permeability from porosity that is derived from the above equations. In crosswell seismic survey, impedance-velocity relation is needed to convert impedance to velocity.

Porosity and density

Unlike the velocity-porosity relationship, the crossplot of density and porosity shows much better correlation (Figure 4.7 (b)). This is because velocity is more strongly affected by lithology whereas density is less so. A similar conclusion can be drawn from a study of sand and shale rocks (Freund, 1992). Therefore, density log (neutron log) should provide better estimation of porosity than sonic log. Two major groups can be identified from the density-porosity plot. They have approximately the same slopes but different intercepts for porosity correlations:

$$\begin{aligned} \text{anhydritic rock:} \quad & \rho_d = 2.91 - 0.033\phi \\ \text{silty rock:} \quad & \rho_d = 2.78 - 0.033\phi \end{aligned}$$

Porosity and permeability

Crossplot of permeability versus porosity is shown in Figure 4.9 (a) for samples having permeabilities above the lower limit of the helium permeameter. There are two main causes for the scatter in the plot. First, the depositional and diagenetic processes may cause the permeability to be larger along the direction parallel to bedding (anisotropy). Second, the pore throats in a rock may vary in size with loading, and for different lithologies the pressure sensitivity is different. The following relationship is found to account for the deposition-related anisotropy at the plug scale:

$$\log_{10} k = 0.35\phi - 3.0\sqrt{1 + 0.25\sin^2\theta} \tag{4.1}$$

where k is permeability in mD (milli-Darcy), ϕ is porosity in percent, and θ is the angle of fluid flow direction relative to the bedding direction. In the field, however, the anisotropy in each lithology as caused by deposition can be neglected because of the large differences in permeability among different lithologies. As for the pressure-dependence of permeability, Jones (1988) has shown that permeability depends on confining pressure σ through: $k = k_0 e^{a(e^{-\sigma/\sigma_o - 1})}/(1 + C_\sigma)$. The parameters σ_o and C_σ are fit from experimental data and k_0 is the permeability at zero confining pressure.

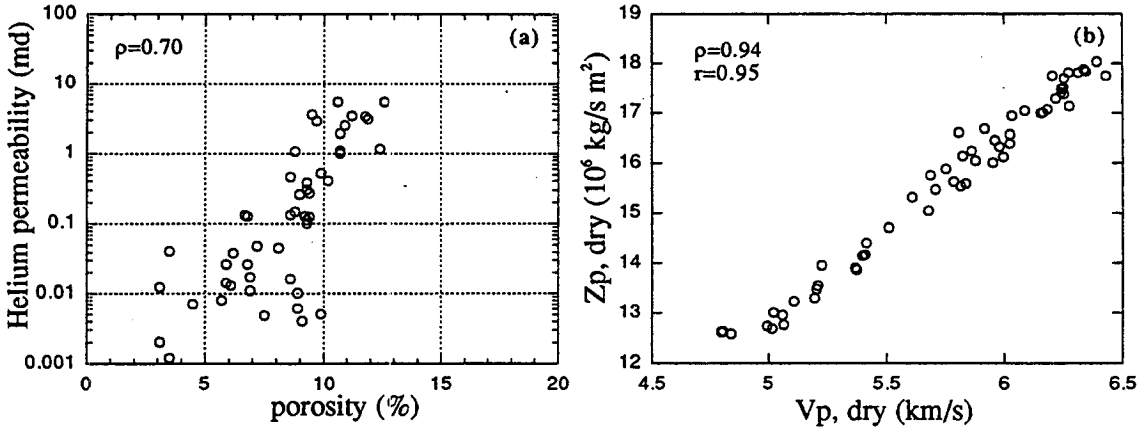

Figure 4.9: (a) Helium permeability versus porosity in carbonate rocks having permeability greater than 0.1 mD (the low measurement limit of instrument); (b) P-wave acoustic impedance versus P-wave velocity in dry rocks. Similar good correlations exist for S-wave and for saturated rocks.

Velocity and impedance

In the full waveform migration of crosswell seismic data, it is the acoustic impedance instead of velocity that can be derived. Knowing the impedance-velocity relationships allows estimating porosity directly from impedance. It is found from the core measurement that this relationship can be modeled very well by linear relations. Figure 4.9 (b) shows the correlation between P-wave impedance (Z_p) and velocity (V_p) in dry rocks. The correlation relations for all four impedances are:

$$\begin{aligned}
\text{dry:} \quad & Z_p = -5.08 + 3.53V_p \quad \rho = 0.98 \\
\text{wet:} \quad & Z_p = -4.75 + 3.51V_p \quad \rho = 0.99 \\
\text{dry:} \quad & Z_s = -4.06 + 3.85V_s \quad \rho = 0.97 \\
\text{wet:} \quad & Z_s = -2.78 + 3.53V_s \quad \rho = 0.98
\end{aligned}$$

Correlations between impedance and porosity show properties similar to those between velocity and porosity.

4.3 Scale and uncertainty analysis

The petrophysical relationships of the last section are all derived from measurements made on plugs ($\sim 20\ cm^3$ in volume). Before using them for any large scale inference (such as log-calibration), a study of support effect and uncertainty is needed.

Uncertainty is the property of non-uniqueness when estimating (inferring) one rock property from other properties of rocks. Different values will arise due to different measurements (at a different location or on a different support) of the same rock property or measurements of different rock properties. On crossplots of such values, uncertainty or scatter appear as "clouds" obscuring any desired correlation. The main sources of uncertainties are analyzed below.

4.3.1 Heterogeneity of rock properties

The heterogeneity of rocks is a geologic or intrinsic source for almost all uncertainties in relating two different rock properties. The scale of such heterogeneity varies greatly. On a large scale, the heterogeneity may arise from the layering of sediments or structural changes due to tectonics. On a small scale, heterogeneity arises from complexities in the minerals composition, the pore geometry, and other textural features. Consequently, the correlation between properties measured on heterogeneous rocks is seldom simple and clean.

There are several different solutions to modeling large scale heterogeneities. The most commonly used one is to break up the lithology of the formation into several homogeneous facies, based on sedimentary stratigraphic analysis done from well logging measurements (e.g. gamma ray intensity). From a rock physics point of view, the division of rock types should be based on matrix velocity. Since the measured velocity depends on both matrix velocity and porosity, the division of facies in situ is done with both gamma ray and sonic logs.

4.3.2 Effect of support

All measurement tools sample rocks on a finite volume. The measured properties are therefore averages over that volume. This averaging is an irreversible process in that fine-scale properties get lost. However, it will be shown in Section 4 that by using stochastic simulation some fine scale features can be "restored" globally provided their spatial distributions are known.

The support effect is a complex concept that relates to the sampling volume geom-

type	frequency	wavelength	object for comparison
laboratory	1 MHz	6 mm (1/4 in)	vug or nodule
logging	10 kHz	0.6 m (2 ft)	thin bed
crosswell	0.8 kHz	7.5 m (25 ft)	sequence
VSP & seismic	30 Hz	200 m (650 ft)	formation

Table 3. Wavelength (directly related to resolution) of laboratory ultrasonic, sonic logging, , cross-well seismic, VSP and surface seismic measurements in carbonate rock (using average V_p of 6.0 km/s).

etry, size, and resolution of the measurement tool (see Table 3), dispersion, acquisition methods, and data processing techniques. The laboratory velocity measurement and a crosswell seismic survey are two examples. The ultrasonic ($\sim$ 1 MHz) transmission technique can resolve millimeter scale features (resolution). But the velocity measured on a plug is the average over the length of a plug (sampling dimension). If the sample is saturated, the result will be different from that measured with a low-frequency tool (for example, resonant bar technique) because of frequency-related dispersion (Biot, 1956; Mavko and Jizba, 1991). The result can be further complicated depending on which technique (first break travel time, phase spectrum, or maximum energy travel time) is used to calculate velocities (data processing). In the case of crosswell seismic survey, the measured velocity is averaged over a much larger volume and preferentially along the direction perpendicular to the well instead of along the well because of the field restriction in acquisitions (acquisition method).

Below, we discuss the support effect of measurements made on core, well logs, and crosswell seismic.

Core measurement vs. sonic log

As opposed to core velocity measurement which is made on inch-scale plugs, sonic velocity is averaged over at least 2 ft interval depending on the sonic tool used. Comparison of the two measurements can be used to indicate existence of thin layers, borehole condition, formation pressure, etc. Depth shifting was made prior to superimposing laboratory core measurements and sonic logs for comparison (see discussions in Section 4.3.3). The original estimate of formation pressure from depth was too low resulting in systematically lower core velocities. Therefore, data at higher pressures was used. As seen from Figure 4.10 (left), the core measurement agrees with the sonic log. The mismatches at certain depths (for example, in the bottom 100 ft portion of well A (left)) show the averaging effect of well logging as they happen mostly at those

depths where velocity extremes (especially low extremes) are. Many techniques, most of them based on deconvolution, are available to reverse this effect (called resolution enhancement). It was not done here because the averaging is not very strong.

Sonic log vs. crosswell tomography

The comparison between sonic velocity and tomogram velocity picked along wells shows a strong averaging effect (Figure 4.10, right). The tomogram velocity cannot follow sudden velocity changes caused by low velocity layers. Sonic velocity must be averaged over at least 20 ft in order to match the tomogram velocity. The three main reasons for this are 1) the resolution of the crosswell seismic survey is at least 10 times lower because of the low frequency used; 2) the acquisition geometry in crosswell survey limits the homogeneous coverage of wave propagation over the whole cross section; and 3) the data processing in getting the velocity tomogram uses only travel time information, and recent progress has shown that by using the whole waveforms (reflection seismogram and wave migration are among the two ways currently used) higher resolution in getting the velocity structure can be reached.

The histogram of the sonic velocity from two wells between which the crosswell seismic survey was conducted and the histogram of tomogram velocity are shown in Figure 4.11. It can be seen that because of the averaging effect, low velocity values are lost more than highs. Rock types corresponding to low velocity are usually silty and have high permeability. Therefore, the averaging associated with crosswell tomogram may lead to an underestimation of flow properties.

Velocity-porosity-gamma ray relationship

Both velocity and gamma ray measurements in well logging are averaged over volumes at least hundreds of times larger than plugs. The relation between velocity and porosity at the core support and well log support is shown by the crossplots of Figure 4.12. In the crossplot for the well logging measurement, porosity measured on whole cores (1 foot long) is used. It can be seen that cores were preferentially sampled in low velocity and high porosity zones, whereas the formation is mainly of the high velocity type (dolostone). However, the two crossplots result in very close $V - \phi - GR$ relationships as shown below:

$$\begin{aligned} \text{core measurement:} \quad & V_p = 6.55 - 0.0843\phi - 8 \times 10^{-5} N_t \qquad \rho = 0.81 \\ \text{well logging:} \quad & V_p = 6.85 - 0.0785\phi - 0.0162 N_t \qquad \rho = 0.78 \end{aligned}$$

The difference between the two coefficients of N_t in the two equations is due to different units used, counts in the first one and API unit in the second one.

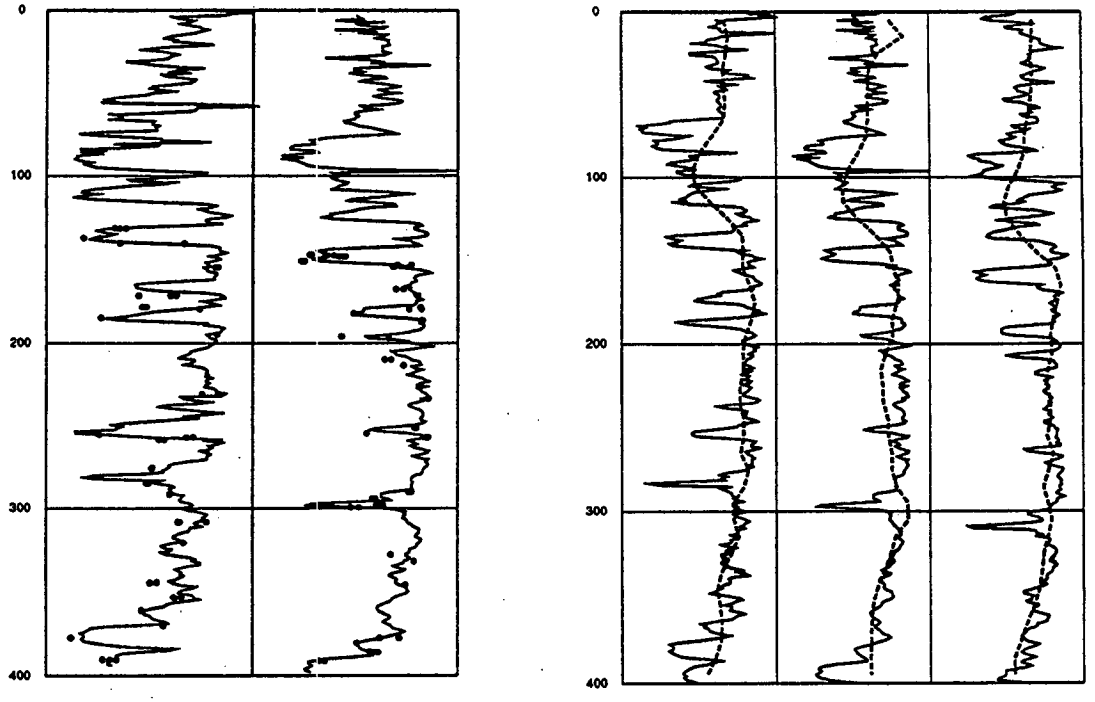

Figure 4.10: Comparison of velocities measured at different supports. Left: core (dot) versus log (curve) in two wells (A and B). Right: log (solid line) versus cross well seismic (dash line) along three wells (from left to right, 5, B, and 3). Range: V_p from 3 (left) to 7 (right) km/s; depth in ft.

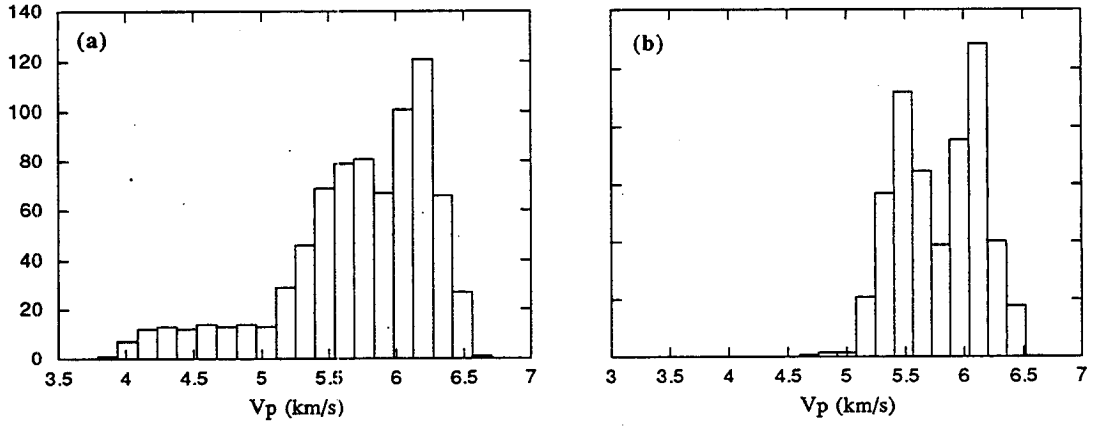

Figure 4.11: Histograms of the sonic velocity (a) along two wells (5 and 3) between which the crosswell seismic survey was conducted and of the tomogram velocity (b) picked along the two wells.

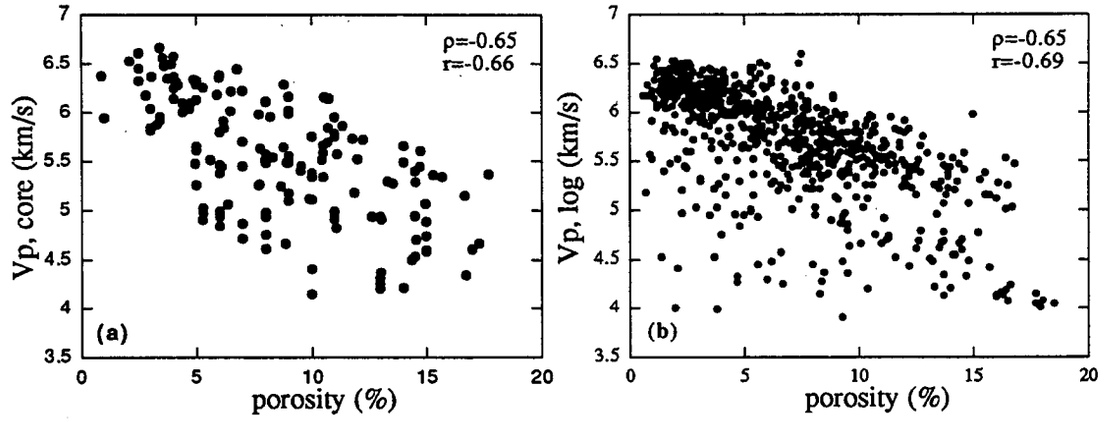

Figure 4.12: Crossplots of measured P-wave velocity versus porosity on plug support (left) and on well logging support (right).

4.3.3 Influence of field conditions

Field measurements usually involve complex conditions (varying formation pressure, borehole rugosity, noise, inadequate data processing, etc.). Therefore, a discrepancy always exists between field measurements and laboratory core measurements for which the experimental conditions can be better controlled. Several corrections are commonly considered. First, depth shift may be needed because cores are marked by the driller's depth while well logs are marked by wireline depth. The amount of shift can be visually determined by examining the plot of core measurements superimposed on the sonic log or by trial and error on the crossplot of the two measurements until the best linear correlation is reached. However, this has to be done with caution, for example, by limiting the maximum shift, in order to prevent generating artificially high correlation. Second, formation pressure needs to be estimated since it determines at what pressure the laboratory measurement should be used for comparison. Again, the trial and error method is used. Third, correction for borehole damage may be needed, as borehole breakouts may increase travel time and therefore gives an underestimation of the sonic velocity.

4.3.4 Randomness from stochastic simulation

Uncertainty in modeling the spatial distribution of rock properties may also stem from the randomness inherent in the stochastic method itself. The power of stochastic models lies in producing equiprobable spatial distributions given some statistics

characteristic of the the variability within the entire field. However, the simulated properties may be artificially more variable than the true rock properties. There are two reasons for this. One is the limited amount of data: fewer data tend to lead to a higher apparent nugget effect. Another reason is that the global variability as shown in variograms may not be applicable locally. An avenue different from relying only on variogram (two-point statistics) needs to be explored in geostatistics. The ultimate solution to stochastic randomness is to obtain more data to allow better conditioning of the simulations. For example, when simulating porosity along the well, using both velocity log and gamma ray log should be more informative than using the velocity log only.

Solutions under study to the problem of randomness due to limited amount of data include the smoothing of the histogram (pre-processing) and smoothing locally the simulated values (post-processing) (Schnetzler, 1994). A simple way of smoothing is to simulate the center values of pixels larger than the size needed and then interpolate values at the non-center locations.

4.4 Resolution enhancement with simulation

Though spatially smoothed as compared with sonic logs, the tomogram velocity from crosswell seismic provides the only velocity measurement in the interwell region. Surface seismic can provide vast subsurface volume coverage, but its resolution is too low. In a 400 ft depth interval, only one and a half cycles can be identified on the 3-D seismogram, which informs neither the structure nor velocity in the interwell region. However, before the tomogram velocity can be used for modeling the spatial distribution of porosity and permeability, the corresponding smoothing effect must be corrected, otherwise extreme values would either be underestimated or overestimated. One solution to resolution enhancement is the increase of the ray coverage density in the crosswell seimic acquisition and the reduction of cell size in the travel-time inversion. The problem, however, is the high cost associated with both field data acquisition and computing time. In this section, the stochastic simulation is adopted as an alternative solution. The idea is to stochastically simulate the interwell velocity at a scale finer than that of the tomogram. In stochastic simulation, additional variability is superimposed on the spatially smoothed tomogram velocity so that the total variability of the modeled velocity mimics that of the sonic logs. At the same time, the velocities averaged over the tomogram cells are required to equal the tomogram velocities. By doing so, sonic logs and crosswell seismic, although defined

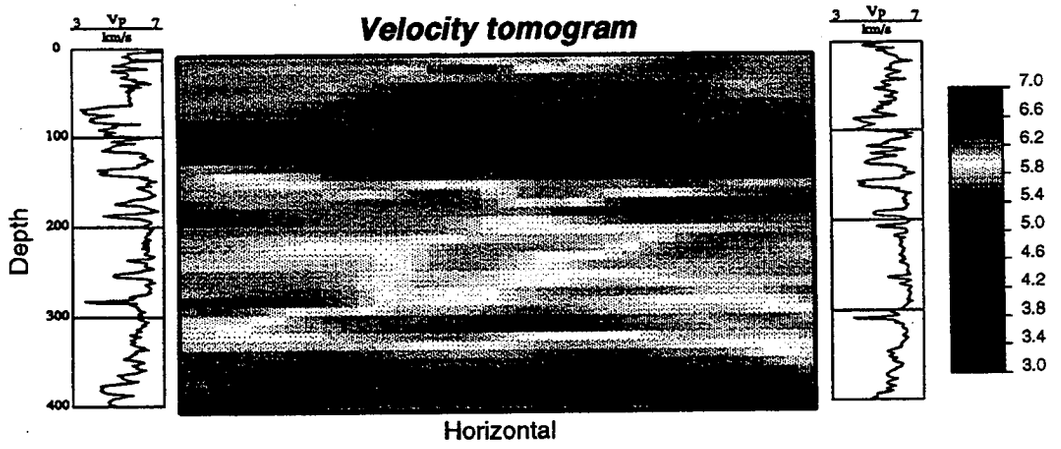

Figure 4.13: Sonic logs and tomogram velocity used to simulate the interwell velocity in the cross section 3-5.

on two different supports, are effectively integrated. In this section, the geometry and variography for the velocity simulation is presented first. Next, the procedure of simulated annealing for variogram matching and the scheme for matching tomogram velocity is given. Finally, simulation results are discussed and the comparison to a sonic log used as validation is presented.

4.4.1 Geometry for simulation and variography

The cross-section 3-5 of Figure 4.1 is chosen for this study of the resolution enhancement by stochastic simulation. Available data are the tomogram velocity between wells 3 and 5 and the sonic logs along wells 3, 5, and B. The sonic logs from wells 3 and 5 are used for simulation while the sonic log from well B is used for validation of the stochastic model.

Figure 4.13 shows that cross-section with the two sonic logs (3 and 5) on the two ends and the tomogram velocity displayed in between. The cross-section's horizontal extent is 720 ft (between 3 and 5) with a depth interval of 400 ft. Thus the tomogram covers $720 \times 400 = 288,000$ ft^2. The cell size in the velocity tomogram is 20×10 ft^2, so there are 1,440 cells in the cross-section. To reduce computing time, the size of the simulation pixels is chosen to be 4×2 ft^2 (instead of 1×1 ft^2), consistent with the sampling interval of sonic logs. There are $(720 \times 400)/(4 \times 2) = 36,000$ pixels in the cross-section, with $(20 \times 10)/(4 \times 2) = 25$ pixels each cell.

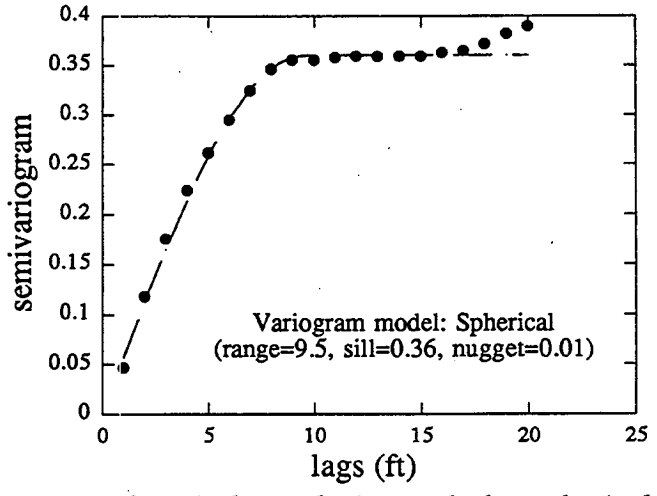

Figure 4.14: Variogram of sonic log velocity and the spherical model. ($a = 9.5$, $c = 0.36$).

The interwell velocity is simulated under the following conditions:

- along well 3 and 5, the velocity values are set equal to the sonic log (conditioning data).
- in the interwell region, the simulated velocity is assumed to have the same histogram as the sonic log
- the simulated velocity has the same variability as that from sonic logs (vertical) and outcrop studies (horizontal) - variogram matching
- the average of the simulated velocity (pixels) over each velocity tomogram cell equals that of the tomogram velocity - tomogram matching

Vertical variability is characterized by a vertical variogram modeled by a spherical model with a range of 9.5 ft (Figure 4.14). Ideally, we should derive the horizontal variogram from well data over a large area. For this work, we have assumed a horizontal range of 10,000 ft (e.g., from outcrop studies), hence an horizontal to vertical anisotropy ratio of 1000. There is a small dipping angle from well 5 to well 3 (2.54°) for the sediment layers in this section, which is an input parameter for the variogram model.

4.4.2 Simulated annealing

Solution to the above problem requires a combinatorial optimization in which all conditions are satisfied. The global optimization technique - simulated annealing (Kirkpatrick et al., 1983) is used here for such a purpose.

The GSLIB stochastic simulation program *sasim* given in Deutsch and Journel (1992) can be used directly for velocity simulation with variogram matching. The steps of a *sasim* run are

1. Non-conditionally simulating the velocity values at all locations in the inter-well region (2D) using the histogram built from the sonic logs (Monte Carlo simulation).

2. Evaluating the objective function defined as the square of the normalized differences between the model variogram $\gamma(h)$ and the (experimental) variogram calculated from simulated values $\gamma^*(h)$:

$$O = \sum_h \frac{[\gamma^*(h) - \gamma(h)]^2}{\gamma(h)^2},$$

   where the summation is over different lags h.

3. Perturbing the 2-D image by the random swapping of velocity values at two different locations and observing if the new objective function O' is less than O. If it is, the acceptance of the swap. If it is not, the swap is accepted with probability $P = exp(-\frac{E_j - E_i}{t})$. This implementation is called *simulated annealing*[3].

4. Repeating the last two steps until certain criteria (for example, the objective function is below a preset value) are met.

4.4.3 Tomogram matching

The flexibility of the simulated annealing technique lies in the fact that the objective function can include many components. By minimizing the total objective function,

[3]Simulated annealing draws analogy from the thermodynamics of a "high" temperature system that has an energy E. When the temperature t of the system is allowed to drop (cooling), the transition probability P of the system from state i to state j is determined by a Boltzman function $P = exp(-\frac{E_j - E_i}{t})$. In geostatistics, the energy E is the objective function O accounting for the various constraints.

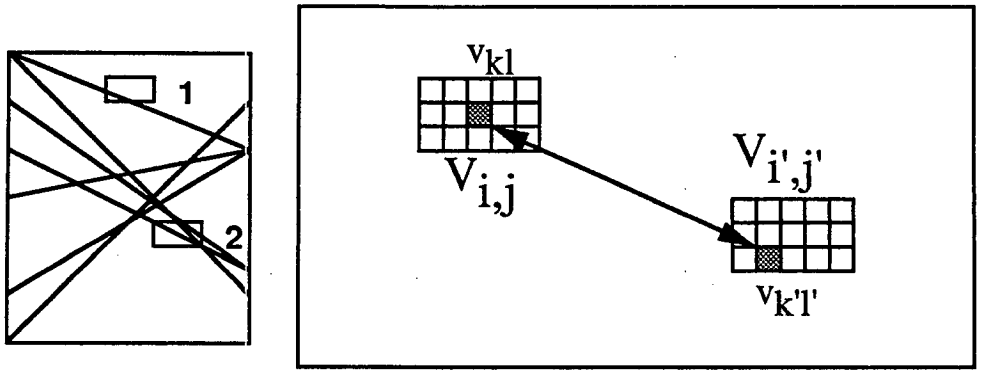

Figure 4.15: Schematic of the relationship between pixel velocity and cell velocity. The double-end arrow represents a swap between pixels (k, l) and (k', l'). The block on the left shows schematically the necessity of weighting cells differently depending on ray density, e.g., cell 2 should be weighted more than cell 1.

each component is also minimized (if some components are dependent, the minimization is a "joint" minimization) so that all conditions are satisfied. Here, a second component for tomogram matching O_2 is defined as:

$$O_2 = \sum_{i,j} w_{i,j}(\bar{V} - V)^2$$

where (i, j) are the indices for a cell in the velocity tomogram whose value V is inverted from cross-well travel times. $\bar{V}$ is the average of the simulated velocity values $v_{k,l}$ over the 25 pixels of the cell. This average could be defined in many ways: algebraic, harmonic, geometric, ... In this study, the arithmetic average is used for simplicity:

$$\bar{V}^*_{i,j} = \frac{1}{25}\sum_{k,l} v_{kl}$$

The relationship between pixel velocity and cell velocity is shown in Figure 4.15 with the arrow representing a swap. $w_{i,j}$ is a weighting factor that weights the ray density in cell (i, j). The more rays pass through a cell (i, j), the higher $w_{i,j}$ since that cell is better informed. $w_{i,j}$ can be calculated from cross-well survey geometry (source spacing, receiver spacing, and depth intervals of both sources and receivers). However, since the velocity tomogram in this study was taken from the homogeneously covered middle part of a larger survey area, all $w_{i,j}$ are set to 1.

The objective function of program *sasim* now contains two components:

$$\begin{aligned} O &= \lambda_1 \frac{1}{\sigma_1} O_1 + \lambda_2 \frac{1}{\sigma_2} O_2 \\ &= \lambda_1 \times \frac{1}{\sigma_1} \sum_h \frac{[\gamma^*(h) - \gamma(h)]^2}{\gamma(h)^2} + \lambda_2 \times \frac{1}{\sigma_2} \sum_{i,j} w_{i,j}(\bar{V}^*_{i,j} - V_{i,j})^2 \end{aligned}$$

where λ_1 and λ_2 are weights assigned by the user ($\lambda_1 + \lambda_2 = 1$), depending on which constraint is to be emphasized, σ_1 and σ_2 are normalization factors so that $O_1 = O_2 = 1$ at the start of simulated annealing.

4.4.4 Simulation results and validation

The original *sasim* program was modified to accommodate the second component in the objective function (see appendix). To test the effect of using different weights for the variogram and velocity tomogram matching, six combinations of weights $(\lambda_1, \lambda_2) = (1, 0), (0.8, 0.2), (0.6, 0.4), (0.4, 0.6), (0.2, 0.8)$, and $(0, 1)$ are used in different *sasim* runs. Manual schedule was used in all simulations with for initial temperature $t_0 = 1$, reduction factor $\lambda = 1$, maximum number of attempted perturbations at any one temperature $K_{max} = 2 \times 10^6$, acceptance target $K_{accept} = 0.2 \times 10^6$, stopping number $S = 3$, and convergence value of the objective function $\Delta O = 0.02$. The results of these simulations are shown in Figure 4.16. The corresponding changes in the objective function O and its components O_1 and O_2, versus number of attempted swaps are plotted in Figure 4.17.

As the weight for the component of tomogram matching λ_2 increases from 0 to 1, a gradual increase of the influence of the tomogram data can be seen. When $\lambda_2 = 0$ (no tomogram matching), the simulated velocity shows a layered structure controlled by the large horizontal to vertical anisotropy ratio of the variogram. There appears also a short periodic structure seen along the layers. This is because of the small number (15) of lags used in the variogram matching. This can be corrected by increasing the number of lags but at a substantial increase in computing time. The influence of velocity tomogram is seen already when λ_2 is as low as 0.2. As long as both λ_1 and λ_2 are non-zero, the effects of both variogram matching and tomogram matching can be seen. Different relative weights do not to produce very different simulations. When $\lambda_2 = 1$ (no variogram matching), however, the layering structure is essentially removed. The simulated velocity follows the pattern of tomogram velocity with additional randomness brought by the stochastic simulation. Interestingly, even though variogram matching is not used, the component of objective function for variogram matching does drop with the annealing, reflecting the weak layering in the velocity tomogram.

Comparison between the sonic log along well B (validation data) and the simulation results picked along well B is shown in Figure 4.18. As the weight λ_2 increases, we see that the trend of simulated velocities better match that of the velocity tomogram but the simulated velocities deviate more from the sonic log. Such deviation is large

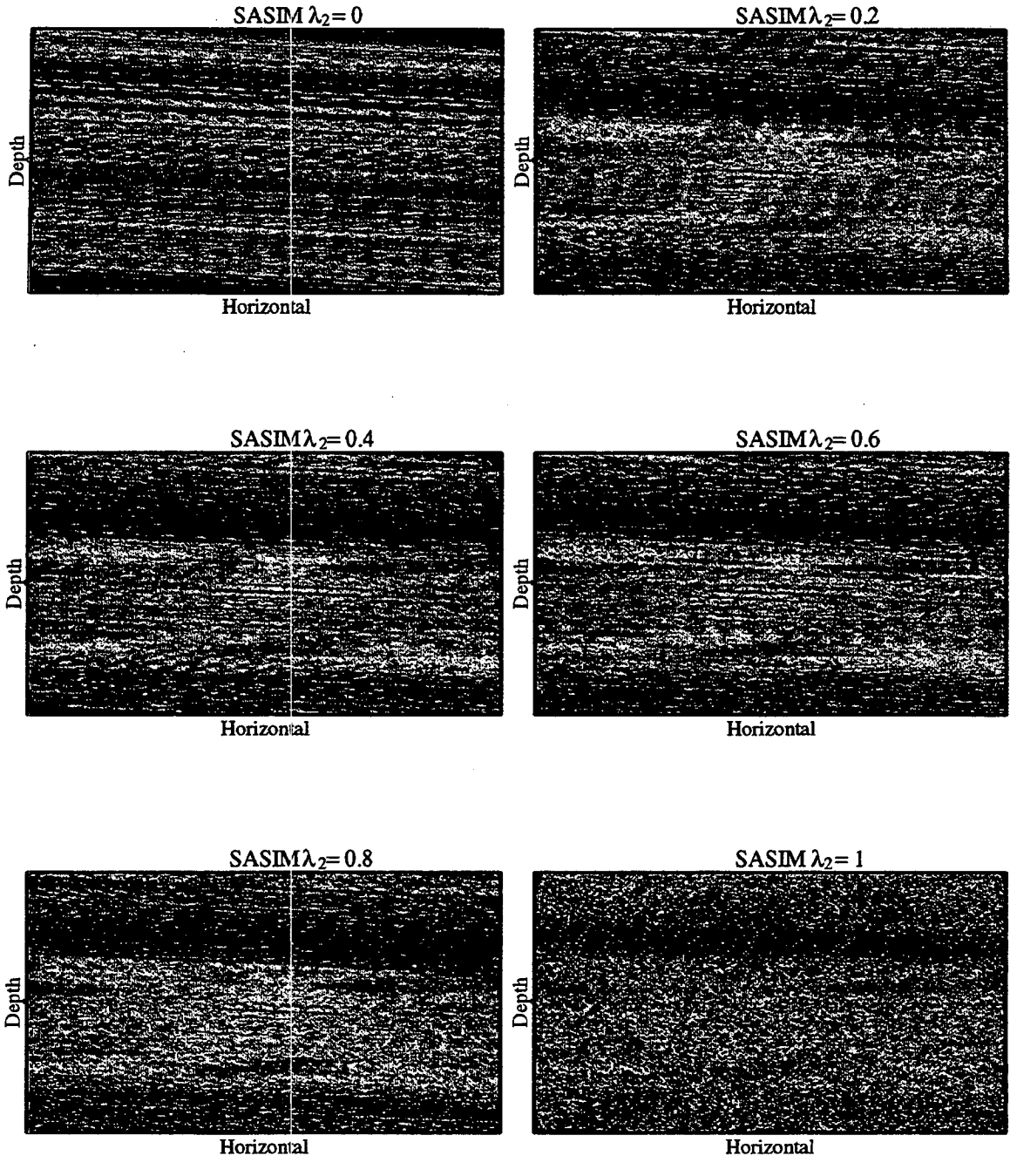

Figure 4.16: Simulation results using different weighting schemes for variogram and the velocity tomogram matching in the objective function. λ_2 is the relative weight for the tomogram matching. Color scale for velocity values is the same as used before.

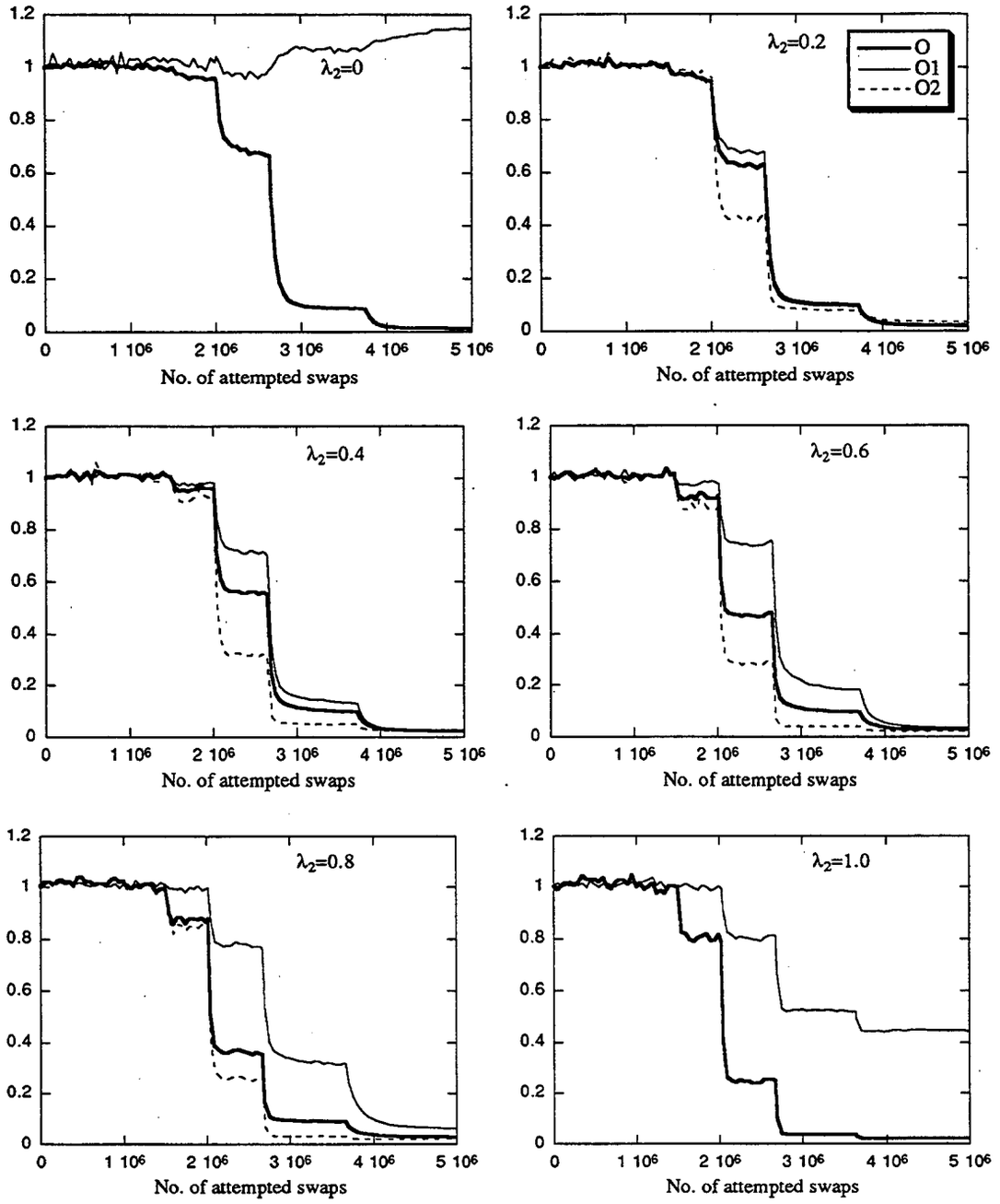

Figure 4.17: Decrease of the objective functions (the sum (thick solid line) and the two components for variogram (thin solid line) and tomogram (dashed line)) with the number of attempted swaps for six different weighting schemes.

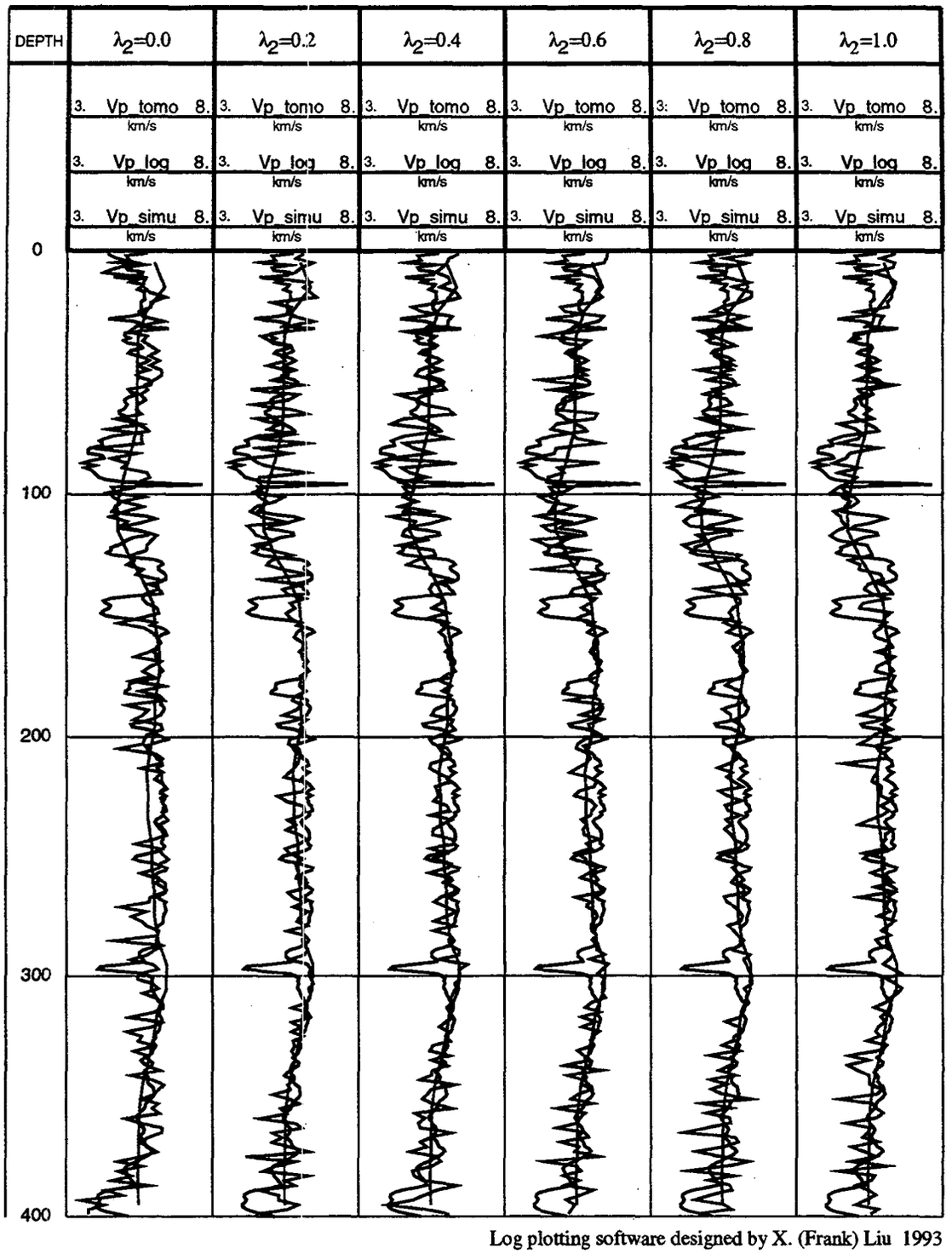

Figure 4.18: Comparison of the simulated velocity (red), sonic velocity (black) and tomogram velocity (green) along well B for six different weighting schemes.

when when sudden changes occur in the sonic log (e.g., at depths 150' and 295'). This is partly because of the edge effect that can be removed by a more complex objective function (Deutsch, 1992).

4.5 Conclusions

Using geophysical measurements made at core, well logging, and crosswell scales, the relations among the petrophysical properties of carbonate rocks and the associated scatters have been investigated. The $V - \phi - GR$ relationship is modeled by $V_p = 6.85 - 0.0785\phi - 0.0162N_t$ (ϕ in percent; N_t in API unit). That regression can be used for estimating porosity from sonic and gamma ray logs. Analysis of residual scatter when correlating measurements made at different supports shows that 1) inaccurate formation pressure is the main cause of scatter when comparing laboratory core with sonic measurements; and 2) the averaging effect of tomogram velocity entails severely poor matching of the sonic logs.

To "reverse" the averaging effect in crosswell tomogram velocity, stochastic simulation by simulated annealing is used to add to the tomogram velocity the short scale variability observed in well logs. The same method can be used (not done here) to simulate the final porosity and permeability distributions in the interwell region. Therefore, geophysical data at different scales (core, well logging, and crosswell) and of different natures (velocity, gamma ray intensity, porosity, and permeability) can be effectively integrated.

Acknowledgements:

Amoco Production Company kindly provided the data for this study. This study was initiated jointly by Dr. Gary Mavko, Dr. Richard Chambers of APR, and the author. The author participated in the acquisition of core (i.e., plug) data while working as a summer intern in 1993 with financial support from APR. He thanks Dr. Richard Chambers, Dr. Chandra Rai, Dr. Gary Mavko, and Wenlong Xu for their helpful discussions and advice.

Appendix

A. Elastic bounds

When the constituent properties (volume fractions, moduli k and μ, and density ρ) of a system are known, the upper and lower limits for the elastic constants of the system can be found using Hashin-Shtrikman equations (Hashin, 1963).

Denoting upper and lower bounds by HS+ and HS- respectively, for a multi-component system we have (Berryman, 1993):

$$\begin{aligned} K^{HS+} &= \Lambda(\mu_{max}) \\ K^{HS-} &= \Lambda\mu_{min} \\ \mu^{HS+} &= \Gamma(\zeta(K_{max}, \mu_{max})) \\ \mu^{HS-} &= \Gamma(\zeta(K_{min}, \mu_{min})) \end{aligned}$$

where

$$\begin{aligned} \Lambda(z) &= \langle \frac{1}{K(r) + \frac{4}{3}z} \rangle^{-1} - \frac{4}{3}z \\ \Gamma(z) &= \langle \frac{1}{\mu(r) + z} \rangle^{-1} - z \\ \zeta(K, \mu) &= \frac{\mu}{6}(\frac{9K + 8\mu}{K + 2\mu}). \end{aligned}$$

The brackets <> indicates volume average over the medium. The average of the HS upper and lower bounds can then be used as estimate of the effective moduli.

Once bulk and shear moduli are known, the compressional and shear wave velocities V_p and V_s can be calculated from

$$V_p = \sqrt{\frac{K + \frac{4}{3}\mu}{\rho}} \tag{4.2}$$

and

$$V_s = \sqrt{\frac{\mu}{\rho}} \tag{4.3}$$

where ρ is the density of the composite that is calculated by $\rho = \sum_i f_i \rho_i$.

B. Modifications to the GSLIB program *sasim* (Deutsch et al., 1992)

Modifications have been made to the original GSLIB program *sasim* to accommodate a second component in the objective function (that for tomogram matching):

a. input of the velocity tomogram data and related information such as grid specification.

b. objective function calculation. For efficient coding, one should update the velocity averages of only those cells involved in the swap, similar to the procedure used for variogram updating (Deutsch and Journel, 1992, p.156). If (k,l) and (k',l') are the two pixels of cells (i,j) and (i',j') to be swapped, the new cell averages $\bar{V}_{i,j}$ and $\bar{V}_{i',j'}$ are:

$$\begin{aligned} \bar{V}_{i,j}^{new} &= \bar{V}_{i,j}^{old} - \frac{1}{25}(v_{kl} - v_{k'l'}); \\ \bar{V}_{i',j'}^{new} &= \bar{V}_{i',j'}^{old} - \frac{1}{25}(v_{k'l'} - v_{kl}). \end{aligned}$$

And the new component objective function is:

$$\begin{aligned} O_2^{new} = \; & O_2^{old} - w_{i,j}[(\bar{V}_{i,j}^{old} - V_{i,j})^2 - (\bar{V}_{i,j}^{new} - V_{i,j})^2] \\ & - w_{i',j'}[(\bar{V}_{i',j'}^{old} - V_{i',j'})^2 - (\bar{V}_{i,j}^{new} - V_{i,j})^2]. \end{aligned}$$

The two subroutines *initob* and *object* with their modifications are listed hereafter.

c. output of intermediate images for given values of the objective function. This is useful to monitor the gradual "cooling" process.

References

Berge, P. A., Bonner, B. P., and Berryman, J. K., 1993, Seismic velocity-porosity relationships for synthetic sandstones: submitted to Geophysics.

Biot, M. A., 1956b, Theory of propagation of elastic waves in a fluid-saturated porous solid. II. Higher-frequency range: J. Acoust. Soc. Am., **28**, 179-191.

Birch, F., 1960, The velocity of compressional waves in rocks to 10 kilobars, 1: J. Geophys. Res., **65**, 1083-1102.

Deutsch, C. V. and Journel, A. G., 1992, GSLIB: Geostatistical Software Library and User's Guide, Oxford University Press.

Frykman, P., and Stentoft, N., 1988, Pore geometry and sound velocity response in Zechstein carbonates: International association of sedimentologists European regional meeting , 78-79.

Han, D., Nur, A. and Morgan, D., 1986, Effects of porosity and clay content on wave velocities in sandstones: Geophysics, **51**, 2093-2107.

Harris, P. M. and S. D. Walker, 1988, McElroy field, in Atlas of oil and gas fields, Treatise of petroleum geology.

Hashin, Z., 1962, The elastic moduli of heterogeneous materials: Am. Soc. Mech. Eng. Trans., J. Appl. Mech., **29**, 143-150.

Hashin, Z., and S. Shtrikman, 1963, A variational approach to the theory of the elastic behaviour of multiphase materials: J. Mech. Phys. Solids, **11**, 127-140.

Hughes, D. S., and H. J. Jones, 1950, Variation of elastic moduli of igneous rocks with pressure and temperature: Bull., Geol. soc. Am., **61**, 843-856.

Jones, S. C., 1988, Two-point determinations of permeability and PV vs. net confining stress: SPE Formation Evaluation.

Kirkpatrick, S., C. D. Gelatt, Jr., and M. P. Vecchi, 1983, Optimization by simulated annealing: Science, **220**, 671-680.

Mavko, G., and D. Jizba, 1991, Estimating grain-scale fluid effects on velocity dispersion in rocks: Geophysics, **56**, 1940-1949.

Rafavich, F., C. Kendall, and T. P. Todd, 1983, The relationship between acoustic properties and the petrographic character of carbonate rocks: Geophysics, **49**, 281-295.

Raymer, L. L., E. R. Junt, and J. S. Gardener, 1980, An improved sonic transit time-to-porosity tarnsform: SPWLA, 21st Ann. Logg. Symp., Paper P.

Reuss, A., 1929, Berechnung der fliessgrense von mischkristallen auf grund der plastizitatsbedingung fur einkristalle: Zeitschrift fur Angewandte Mathematik and Mechanik, **9**, 49-58.

Tosaya, C. and A. Nur, 1982, Effects of diagenesis and clays on compressional velocities in rocks: Geophys. Res. Letts., **9**, 5-8.

Vernik, L., and A. Nur, 1992, Petrophysical classification of siliciclastics for lithology and porosity prediction from seismic velocities: AAPG Bulletin, **76**, 1295-1309.

Voigt, W., 1928, Lehrbuch der kristallphysik: Teubner.

Wilkens, R., G. Simmons, and L. Caruso, 1984, The ratio V_p/V_s as a discriminant of composition for siliceous limestones: Geophysics, **49**, 1850-1860.

Wyllie, M. R. J., A. R. Gregory, and L. W. Gardner, 1956, Elastic wave velocities in heterogeneous and porous media: Geophysics, **21**, 41-70.

Chapter 5

Data collection

This chapter documents all data collected for this dissertation work. The data consist of velocities measured under both uniaxial compressive stress and confining pressure, made for studying the applicability of using second-order elasticity theory for the stress dependence of velocities (Chapter 2), and velocities along different directions relative to bedding made for the study of the relationships between velocity, elastic anisotropy and petrophysical-chemical parameters of shales (Chapter 3). At the beginning of each section, there is a self-contained description of the original experimental design, equipment, and experimental procedure. All samples parameters such as porosity, density, and so on are listed in a single table which is then followed by data tables.

5.1 Velocities under uniaxial stress and hydrostatic pressure

Original design

Data documented in this section was collected for studying the nonlinear elasticity of and, in particular, for measuring the third-order elastic (TOE) constants of rocks. Equations for calculating the TOE constants can be found in Hughes and Kelly (1953). The measured ultrasonic velocities include those of compressional and shear modes along the same propagation path under hydrostatic confining pressure and along three orthogonal paths under unconfined uniaxial stress (one along and two perpendicular to the direction of stress).

Experimental procedure

For the unconfined uniaxial measurement, stress levels were coded into the computer control program (written in *LabView*© [1]) and stress was increased at steps from 0 to 0.6, 1.2, 1.8, 2.4, 3.0, 4.0, 6.0, ..., MPa until the rock sample failed. At each stress level, four waveforms of different modes or different propagation paths were recorded, averaged over 256 times, and stored in the computer disk for later analysis. Four pairs of transducers (two compressional and two shear) were dedicated to the measurement. The sample length (along which direction stress was applied) was recorded. LVDT was used to monitor the diameter change on one rock sample. The analysis was mainly velocity calculation from the picked first-break of the signal and the sample length (length of wave paths).

For the hydrostatic case, effective pressures (the pore pressure was atmospheric) at which velocities were measured were 0, 0.6, 1.2, 1.8, 2.4, 3.0, 4.0, 6.0, ..., 68 MPa. Pressure was manually controlled with an air pump. At each pressure level, waveforms of transmitted broadband signals (averaged over 256 times to reduce noise) were recorded and stored in the computer hard disk for later analysis. Though the transducers operated in shear mode, a small but strong enough compressional mode signal always accompanied the shear mode. So the same pair of shear mode transducers was used to obtain both shear and compressional wave velocities. The analysis was similar to that in the hydrostatic case.

[1] *LabView*© is a laboratory data acquisition and signal analysis software by National Instruments, Inc.

Equipment and set-up

Equipment

The equipment and its use for this experiment is listed below:

equipment	uses
Instron 4508 test system	applying unconfined uniaxial stress to test sample
Autoclave Engineers' pressure vessel and control	applying hydrostatic pressure to test sample
Panametric 5052 UA ultrasonic analyzer	adjustable, broad-band signal source and receiving
Panametric ultrasonic transducers (V133,156,102)	transmitter and receiver of broad-band ultrasonic signals
Racal-Dana high voltage multi-switch	switch for 4 pairs of transmitter-receivers
RTD710 Digitizer (by Tectronix and Sony)	signal digitization
Mac IIfx computer (with *LabView* software)	measurement control and data processing

Set-up

The ultrasonic transmission measurement system was the same in both uniaxial and hydrostatic measurements. The main differences in other aspects were the stress application and the number of transmitter-receiver pairs. Figure 5.1 (a) is a schematic diagram of the experimental set-ups showing both uniaxial and hydrostatic measurement sysmtems.

Samples

The two rock samples for the respective uniaxial and hydrostatic tests were cored next to each other from the same block and the two surfaces for positioning transducers were groundd parallel to each other. Figure 5.1 (b) shows the sample geometries and wave modes, as well as propagation path designations as used in the data tables (a for the uniaxial stress test and b for the hydrostatic pressure test). All rock samples were washed clean, oven-dried at 80 °C for one night, and then left in room-conditions for one day before the test.

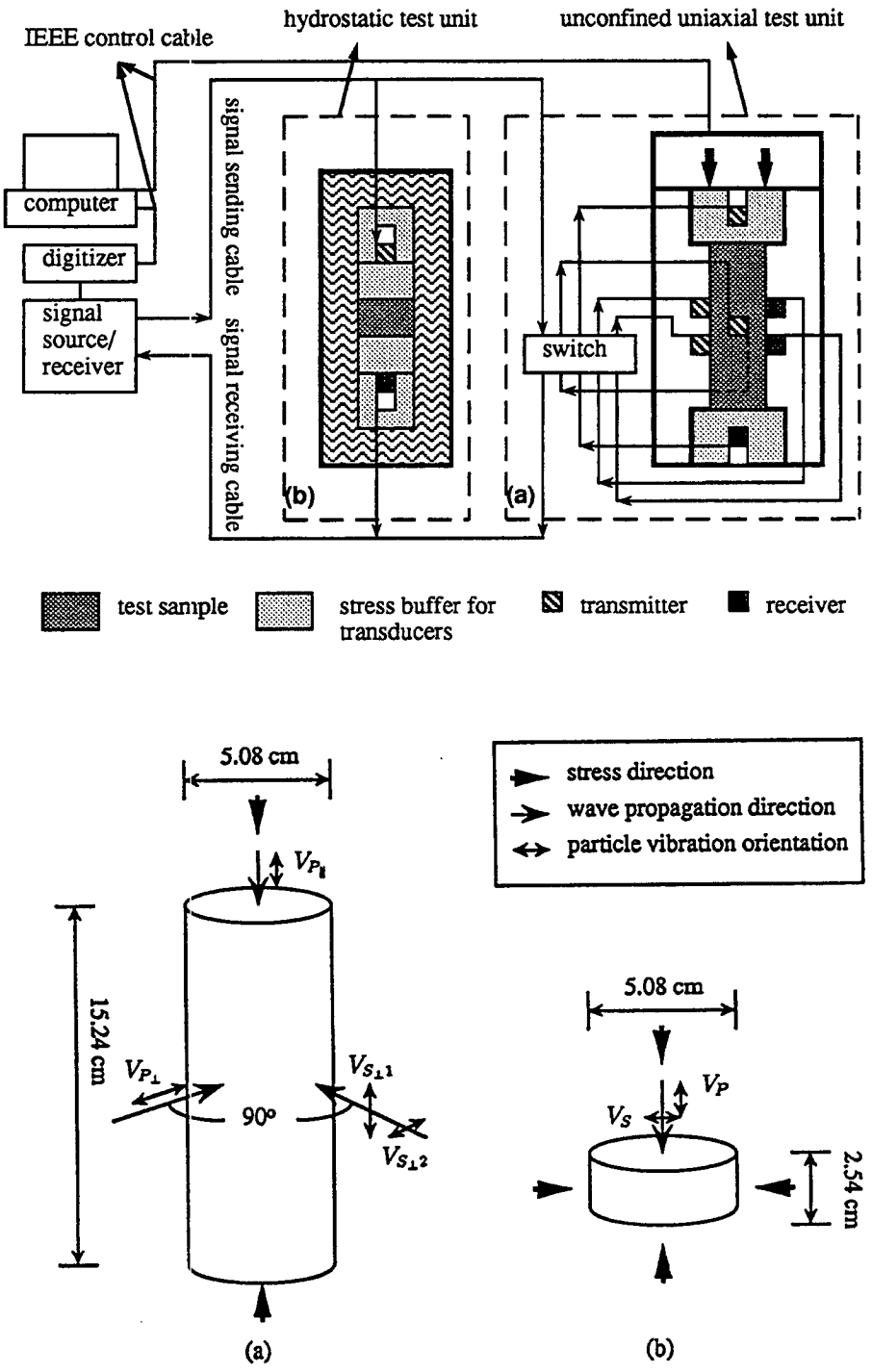

Figure 5.1: Top: A schematic diagram of the experimental setup used for velocity measurements under uniaxial stress (block a) and hydrostatic pressure (block b); Bottom: Sample geometry and velocity designations for measurement under (a) uniaxial stress and (b) confining pressure.

Tables

Table 6.1 lists the parameters for samples on which velocities are measured under both uniaxial stress and hydrostatic pressure. Table 6.2 through 6.10 then list the ultrasonic velocities measured in 8 rock samples and 1 synthetic sample (cemented glass beads) under either uniaxial stress or hydrostatic pressure. Refer to Figure 5.1 for the velocity designations).

Table 5.1.1 Parameters of samples

sample	grain density (g/cm^3	porosity (%)	permeability (md)	failure stress MPa
Berea sandstone	2.66	22.0	131.0	44.5
Massillon sandstone (1066)	2.74	24.6	1,425	32.0
Massillon sandstone (1185)	2.65	21.0	2,500	44.0
Hanson sandstone	2.70	16.0	1.7	52.0
Buff sandsonte	2.70	16.0	1.2	44.0
Portland sandsonte	2.68	20.0	850	34.0
cemented glass beads	2.28		3,500	74.0
Westerly granite				
Leuders limestone	2.20	19.8	0.5	50.0

Table 5.1.2 Ultrasonic velocities of Berea sandstone

P (MPa)	$-\Delta L$ (mm)	$V_{P\parallel}$ (km/s)	$V_{P\perp}$ (km/s)	$V_{S\perp 1}$ (km/s)	$V_{S\perp 2}$ (km/s)	V_P (km/s)	V_S (km/s)
0.0	0.000	1.942	1.894	1.321	1.281	1.941	1.344
0.1	0.177	1.966	1.917	1.326	1.289	2.001	1.401
0.6	0.288	2.038	1.946	1.357	1.311	2.172	1.504
1.2	0.345	2.175	1.978	1.417	1.330	2.271	1.558
1.8	0.392	2.325	2.000	1.459	1.344	2.361	1.633
2.4	0.429	2.455	2.030	1.494	1.363	2.459	1.688
3.0	0.462	2.557	2.052	1.540	1.381	2.506	1.731
4.0	0.508	2.735	2.084	1.603	1.405	2.600	1.788
6.0	0.580	2.978	2.135	1.698	1.452	2.718	1.870
8.0	0.640	3.127	2.178	1.763	1.487	2.806	1.940
10.0	0.692	3.227	2.208	1.804	1.516	2.898	2.003
12.0	0.739	3.318	2.230	1.836	1.541	2.985	2.053
14.0	0.783	3.377	2.250	1.865	1.561	3.048	2.103
16.0	0.824	3.436	2.269	1.891	1.574	3.106	2.142
18.0	0.864	3.472	2.281	1.914	1.583	3.156	2.172
20.0	0.903	3.505	2.290	1.927	1.584	3.201	2.199
22.0	0.941	3.541	2.293	1.936	1.586	3.234	2.221
24.0	0.980	3.571	2.290	1.943	1.583	3.268	2.253
26.0	1.018	3.585	2.287	1.948	1.579	3.290	2.265
28.0	1.056	3.600	2.279	1.952	1.573	3.325	2.282
30.0	1.093	3.606	2.267	1.951	1.567	3.345	2.303
32.0	1.132	3.612	2.249	1.950	1.558	3.375	2.316
34.0	1.170	3.614	2.224	1.946	1.544	3.390	2.333
36.0	1.208	3.615	2.191	1.939	1.526	3.413	2.352
38.0	1.248	3.618	2.160	1.925	1.505	3.428	2.357
40.0	1.289	3.619	2.109	1.908	1.459	3.443	2.369
41.0	1.314	3.610	2.047	1.887	1.427	3.459	2.375
42.0	1.338	3.609	2.000	1.869	1.397	3.463	2.385
43.0	1.364	3.605	1.956	1.847	1.377	3.469	2.390
44.0	1.394	3.593	1.766	1.680	1.206	3.472	2.396

Table 5.1.3 Ultrasonic velocities of Massillong sandstone (#1066)

P (MPa)	$-\Delta L$ (mm)	$V_{P_\parallel}$ (km/s)	$V_{P_\perp}$ (km/s)	$V_{S_{\perp 1}}$ (km/s)	$V_{S_{\perp 2}}$ (km/s)	V_P (km/s)	V_S (km/s)
0.0	0.000	2.062	2.148	1.401	1.383	2.162	1.413
0.1	0.736	2.073	2.152	1.407	1.390	2.389	1.568
0.6	0.861	2.189	2.162	1.452	1.397	2.574	1.702
1.2	0.904	2.359	2.190	1.490	1.408	2.660	1.752
1.8	0.936	2.501	2.223	1.532	1.429	2.735	1.809
2.4	0.965	2.607	2.239	1.573	1.441	2.826	1.845
3.0	0.991	2.698	2.268	1.602	1.451	2.873	1.882
4.0	1.027	2.819	2.300	1.653	1.474	2.936	1.913
6.0	1.091	2.979	2.330	1.728	1.511	3.026	1.966
8.0	1.145	3.072	2.355	1.787	1.532	3.096	2.014
10.0	1.193	3.125	2.366	1.806	1.538	3.142	2.052
12.0	1.238	3.177	2.375	1.826	1.546	3.178	2.100
14.0	1.281	3.218	2.381	1.849	1.549	3.222	2.133
16.0	1.323	3.243	2.384	1.858	1.550	3.269	2.171
18.0	1.367	3.258	2.369	1.864	1.540	3.307	2.202
20.0	1.410	3.274	2.345	1.861	1.528	3.338	2.223
22.0	1.454	3.278	2.324	1.848	1.511	3.353	2.245
24.0	1.498	3.290	2.288	1.831	1.488	3.374	2.270
26.0	1.543	3.296	2.260	1.804	1.459	3.388	2.283
28.0	1.589	3.301	2.186	1.792	1.413	3.409	2.301
30.0	1.642	3.308	2.081	1.745	1.335	3.430	2.285

Table 5.1.4 Ultrasonic velocities of Massillong sandstone (#1185)

P (MPa)	$-\Delta L$ (mm)	$V_{P_\parallel}$ (km/s)	$V_{P_\perp}$ (km/s)	$V_{S_\perp 1}$ (km/s)	$V_{S_\perp 2}$ (km/s)	V_P (km/s)	V_S (km/s)
0.0	0.000	2.434	2.684	1.733	1.753	2.643	1.740
0.1	0.717	2.438	2.686	1.730	1.752	2.728	1.826
0.6	0.835	2.546	2.689	1.762	1.759	2.823	1.908
1.2	0.875	2.718	2.700	1.809	1.774	3.061	2.025
1.8	0.914	2.828	2.712	1.834	1.789	3.127	2.131
2.4	0.946	2.892	2.726	1.861	1.797	3.187	2.154
3.0	0.974	2.973	2.732	1.876	1.809	3.227	2.231
4.0	1.019	3.049	2.746	1.902	1.816	3.311	2.285
6.0	1.087	3.172	2.755	1.946	1.825	3.406	2.355
8.0	1.148	3.242	2.760	1.981	1.827	3.474	2.389
10.0	1.205	3.293	2.766	2.024	1.832	3.521	2.433
12.0	1.253	3.341	2.761	2.048	1.834	3.563	2.462
14.0	1.299	3.398	2.760	2.063	1.834	3.614	2.488
16.0	1.345	3.449	2.755	2.078	1.833	3.659	2.530
18.0	1.386	3.486	2.751	2.091	1.829	3.704	2.547
20.0	1.426	3.530	2.745	2.103	1.829	3.759	2.569
22.0	1.467	3.555	2.736	2.115	1.822	3.780	2.586
24.0	1.504	3.571	2.729	2.117	1.817	3.809	2.620
26.0	1.543	3.583	2.715	2.115	1.812	3.835	2.640
28.0	1.580	3.593	2.702	2.111	1.805	3.871	2.673
30.0	1.617	3.596	2.681	2.106	1.800	3.895	2.685
32.0	1.655	3.605	2.662	2.094	1.785	3.922	2.710
34.0	1.694	3.616	2.644	2.084	1.767	3.935	2.728
36.0	1.734	3.631	2.604	2.066	1.736	3.951	2.754
38.0	1.771	3.634	2.556	2.051	1.698	3.960	2.763
40.0	1.814	3.631	2.443	2.013	1.645	3.976	2.775
42.0	1.868	3.620	2.230	1.895	1.460	3.990	2.786

Table 5.1.5 Ultrasonic velocities of Hanson sandstone

P (MPa)	$-\Delta L$ (mm)	$V_{P_\parallel}$ (km/s)	$V_{P_\perp}$ (km/s)	$V_{S_\perp 1}$ (km/s)	$V_{S_\perp 2}$ (km/s)	V_P (km/s)	V_S (km/s)
0.0	0.000	3.020	3.246	2.047	2.122	3.091	2.022
0.1	0.182	3.024	3.250	2.049	2.123	3.115	2.029
0.6	0.280	3.050	3.250	2.051	2.122	3.178	2.038
1.2	0.309	3.088	3.253	2.068	2.126	3.212	2.056
1.8	0.332	3.119	3.256	2.080	2.128	3.252	2.070
2.4	0.352	3.156	3.254	2.099	2.132	3.272	2.080
3.0	0.372	3.187	3.258	2.113	2.133	3.299	2.102
4.0	0.401	3.234	3.262	2.132	2.138	3.329	2.119
6.0	0.456	3.315	3.269	2.161	2.145	3.392	2.159
8.0	0.505	3.373	3.277	2.180	2.152	3.440	2.188
10.0	0.552	3.418	3.268	2.188	2.153	3.496	2.216
12.0	0.597	3.455	3.268	2.196	2.150	3.533	2.235
14.0	0.643	3.482	3.262	2.202	2.145	3.582	2.265
16.0	0.687	3.512	3.256	2.208	2.143	3.603	2.291
18.0	0.730	3.544	3.248	2.214	2.136	3.647	2.311
20.0	0.772	3.572	3.236	2.219	2.128	3.690	2.335
22.0	0.814	3.594	3.226	2.222	2.122	3.726	2.355
24.0	0.855	3.613	3.218	2.225	2.118	3.752	2.367
26.0	0.896	3.638	3.208	2.231	2.114	3.775	2.385
28.0	0.938	3.657	3.191	2.235	2.107	3.802	2.412
30.0	0.976	3.666	3.170	2.242	2.103	3.830	2.422
32.0	1.021	3.683	3.158	2.242	2.094	3.860	2.437
34.0	1.056	3.697	3.150	2.243	2.091	3.880	2.454
36.0	1.095	3.707	3.134	2.241	2.082	3.923	2.474
38.0	1.135	3.720	3.116	2.239	2.074	3.945	2.486
40.0	1.174	3.728	3.098	2.239	2.063	3.973	2.508
42.0	1.213	3.735	3.080	2.238	2.054	3.988	2.520
44.0	1.253	3.740	3.053	2.235	2.049	4.009	2.532
46.0	1.292	3.749	3.039	2.231	2.038	4.026	2.545
48.0	1.333	3.755	3.010	2.226	2.023	4.054	2.561
50.0	1.374	3.765	2.987	2.221	2.010	4.072	2.575
52.0	1.417	3.769	2.954	2.217	1.998	4.085	2.590
54.0	1.458	3.772	2.929	2.206	1.971	4.096	2.598
56.0	1.502	3.774	2.883	2.192	1.947	4.114	2.612
58.0	1.554	3.769	2.838	2.177	1.917	4.130	2.620
60.0	1.598	3.766	2.782	2.158	1.881	4.156	2.639
62.0	1.664	3.757	2.637	2.107	1.800	4.170	2.645
64.0	1.718	3.744	2.481	2.030	1.718	4.189	2.662

Table 5.1.6 Ultrasonic velocities of Buff sandstone

P (MPa)	$-\Delta L$ (mm)	$V_{P\parallel}$ (km/s)	$V_{P\perp}$ (km/s)	$V_{S\perp 1}$ (km/s)	$V_{S\perp 2}$ (km/s)	V_P (km/s)	V_S (km/s)
0.0	0.000	3.200	3.007	2.029	1.970	3.158	2.102
0.1	0.524	3.202	3.003	2.030	1.970	3.185	2.090
0.6	0.632	3.224	3.000	2.033	1.968	3.200	2.111
1.2	0.670	3.250	2.994	2.036	1.966	3.222	2.124
1.8	0.705	3.273	2.986	2.040	1.965	3.242	2.133
2.4	0.732	3.293	2.982	2.041	1.963	3.261	2.145
3.0	0.757	3.315	2.979	2.046	1.962	3.271	2.155
4.0	0.790	3.340	2.972	2.051	1.956	3.300	2.168
6.0	0.850	3.389	2.956	2.060	1.952	3.343	2.197
8.0	0.905	3.432	2.942	2.067	1.945	3.383	2.226
10.0	0.957	3.469	2.929	2.073	1.937	3.429	2.256
12.0	1.012	3.504	2.915	2.078	1.932	3.475	2.280
14.0	1.054	3.536	2.898	2.083	1.926	3.513	2.301
16.0	1.099	3.561	2.886	2.089	1.919	3.552	2.321
18.0	1.144	3.592	2.873	2.091	1.909	3.586	2.339
20.0	1.189	3.611	2.857	2.094	1.899	3.623	2.362
22.0	1.232	3.640	2.845	2.096	1.891	3.652	2.376
24.0	1.274	3.668	2.822	2.100	1.879	3.682	2.396
26.0	1.319	3.684	2.808	2.102	1.870	3.710	2.415
28.0	1.359	3.702	2.795	2.102	1.859	3.749	2.431
30.0	1.402	3.725	2.771	2.100	1.848	3.770	2.450
32.0	1.443	3.734	2.749	2.098	1.836	3.808	2.474
34.0	1.485	3.749	2.725	2.095	1.823	3.830	2.485
36.0	1.529	3.758	2.698	2.093	1.808	3.861	2.504
38.0	1.574	3.773	2.670	2.088	1.792	3.885	2.516
40.0	1.614	3.785	2.639	2.081	1.775	3.911	2.539
42.0	1.657	3.794	2.609	2.074	1.756	3.940	2.550
44.0	1.705	3.800	2.566	2.060	1.732	3.967	2.576
46.0	1.747	3.807	2.520	2.043	1.707	3.980	2.589
48.0	1.795	3.810	2.453	2.021	1.662	4.012	2.601
50.0	1.849	3.800	2.371	1.980	1.608	4.030	2.614
52.0	1.931	3.781	2.310	1.891	1.471	4.059	2.629

Table 5.1.7 Ultrasonic velocities of Portland sandstone

P (MPa)	$-\Delta L$ (mm)	$V_{P_\parallel}$ (km/s)	$V_{P_\perp}$ (km/s)	$V_{S_{\perp 1}}$ (km/s)	$V_{S_{\perp 2}}$ (km/s)	V_P (km/s)	V_S (km/s)
0.0	0.000	2.999	3.060	1.856	1.841	3.005	1.837
0.1	0.347	3.003	3.063	1.856	1.843	3.020	1.843
0.6	0.440	3.010	3.065	1.858	1.845	3.032	1.847
1.2	0.472	3.017	3.065	1.860	1.846	3.042	1.853
1.8	0.496	3.028	3.067	1.862	1.848	3.059	1.866
2.4	0.517	3.035	3.065	1.864	1.844	3.068	1.872
3.0	0.537	3.046	3.068	1.866	1.843	3.074	1.883
4.0	0.568	3.071	3.070	1.871	1.842	3.098	1.892
6.0	0.624	3.104	3.072	1.880	1.841	3.131	1.920
8.0	0.676	3.135	3.071	1.891	1.838	3.154	1.932
10.0	0.726	3.167	3.067	1.902	1.832	3.198	1.949
12.0	0.773	3.194	3.067	1.910	1.831	3.228	1.966
14.0	0.821	3.224	3.062	1.918	1.830	3.256	1.986
16.0	0.865	3.242	3.059	1.923	1.827	3.293	2.011
18.0	0.911	3.269	3.050	1.926	1.824	3.313	2.030
20.0	0.961	3.282	3.046	1.929	1.821	3.343	2.044
22.0	1.015	3.300	3.022	1.930	1.814	3.373	2.062
24.0	1.071	3.312	2.986	1.927	1.805	3.404	2.082
26.0	1.132	3.326	2.965	1.923	1.787	3.428	2.094
28.0	1.197	3.338	2.917	1.914	1.767	3.460	2.111
30.0	1.268	3.342	2.868	1.898	1.730	3.475	2.120
31.0	1.319	3.349	2.832	1.887	1.709	3.495	2.130
32.0	1.367	3.347	2.770	1.868	1.677	3.510	2.145
33.0	1.426	3.340	2.671	1.835	1.614	3.525	2.152

Table 5.1.8 Ultrasonic velocities of cemented glass beads

P (MPa)	$-\Delta L$ (mm)	$V_{P_\parallel}$ (km/s)	$V_{P_\perp}$ (km/s)	$V_{S_\perp 1}$ (km/s)	$V_{S_\perp 2}$ (km/s)	V_P (km/s)	V_S (km/s)
0.0	-.023	3.108	2.962	1.824	1.749	3.088	1.797
0.1	0.528	3.110	2.962	1.825	1.750	3.089	1.800
0.6	0.656	3.110	2.963	1.826	1.750	3.093	1.809
1.2	0.703	3.113	2.963	1.827	1.750	3.101	1.812
1.8	0.736	3.117	2.964	1.827	1.751	3.106	1.817
2.4	0.765	3.123	2.964	1.828	1.750	3.113	1.820
3.0	0.789	3.124	2.964	1.828	1.751	3.118	1.826
4.0	0.825	3.126	2.965	1.829	1.751	3.124	1.833
6.0	0.887	3.128	2.965	1.829	1.751	3.139	1.840
8.0	0.946	3.131	2.965	1.830	1.752	3.150	1.850
10.0	1.000	3.135	2.965	1.831	1.751	3.156	1.856
12.0	1.053	3.137	2.965	1.832	1.751	3.167	1.862
14.0	1.103	3.140	2.965	1.833	1.751	3.174	1.869
16.0	1.154	3.141	2.965	1.833	1.750	3.185	1.876
18.0	1.205	3.144	2.965	1.834	1.750	3.196	1.882
20.0	1.256	3.151	2.965	1.835	1.750	3.205	1.890
22.0	1.308	3.156	2.965	1.836	1.748	3.214	1.896
24.0	1.360	3.159	2.964	1.837	1.748	3.224	1.904
26.0	1.414	3.163	2.964	1.837	1.748	3.235	1.909
28.0	1.467	3.172	2.963	1.838	1.748	3.247	1.915
30.0	1.524	3.170	2.962	1.838	1.747	3.253	1.922
32.0	1.581	3.178	2.961	1.838	1.747	3.263	1.927
34.0	1.639	3.184	2.959	1.839	1.747	3.268	1.932
36.0	1.701	3.191	2.957	1.839	1.747	3.277	1.938
38.0	1.767	3.192	2.957	1.839	1.747	3.287	1.943
40.0	1.834	3.199	2.955	1.839	1.747	3.297	1.949
42.0	1.902	3.202	2.952	1.839	1.746	3.310	1.955
44.0	1.975	3.204	2.950	1.840	1.745	3.320	1.961
46.0	2.055	3.208	2.948	1.840	1.744	3.330	1.966
48.0	2.137	3.213	2.946	1.840	1.744	3.340	1.972
50.0	2.221	3.210	2.945	1.839	1.742	3.348	1.979
52.0	2.353	3.213	2.943	1.839	1.741	3.358	1.985
54.0	2.437	3.217	2.941	1.839	1.739	3.367	1.992
56.0	2.540	3.220	2.938	1.838	1.736	3.377	1.997
58.0	2.655	3.221	2.933	1.837	1.732	3.386	2.004
60.0	2.800	3.228	2.930	1.837	1.730	3.396	2.012

Table 5.1.9 Ultrasonic velocities of Westerly granite

P (MPa)	$-\Delta L$ (mm)	$V_{P_\parallel}$ (km/s)	$V_{P_\perp}$ (km/s)	$V_{S_\perp 1}$ (km/s)	$V_{S_\perp 2}$ (km/s)	V_P (km/s)	V_S (km/s)
0.0	0.000	4.753	4.832	3.004	2.995	4.791	2.957
0.1	0.684	4.758	4.835	3.009	2.995	4.817	2.963
0.6	0.778	4.775	4.846	3.012	2.995	4.822	2.994
1.2	0.806	4.796	4.861	3.020	2.997	4.854	3.030
1.8	0.826	4.830	4.874	3.025	3.000	4.891	3.056
2.4	0.845	4.859	4.881	3.030	3.000	4.941	3.076
3.0	0.859	4.898	4.896	3.034	3.001	4.982	3.093
4.0	0.881	4.958	4.911	3.049	3.002	5.013	3.116
6.0	0.921	5.050	4.947	3.066	3.003	5.120	3.165
8.0	0.956	5.103	4.981	3.083	3.005	5.204	3.219
10.0	0.988	5.152	5.013	3.101	3.009	5.263	3.260
12.0	1.017	5.193	5.030	3.115	3.012	5.321	3.301
14.0	1.045	5.226	5.047	3.129	3.017	5.399	3.333
16.0	1.072	5.264	5.065	3.138	3.020	5.451	3.385
18.0	1.098	5.295	5.085	3.149	3.024	5.499	3.406
20.0	1.124	5.324	5.092	3.155	3.034	5.564	3.443
22.0	1.148	5.349	5.101	3.165	3.041	5.596	3.471
24.0	1.172	5.373	5.115	3.173	3.047	5.636	3.498
26.0	1.196	5.392	5.123	3.183	3.050	5.680	3.526
28.0	1.221	5.411	5.128	3.191	3.053	5.727	3.551
30.0	1.244	5.421	5.131	3.195	3.057	5.760	3.571
32.0	1.267	5.438	5.134	3.201	3.065	5.804	3.592
34.0	1.280	5.443	5.139	3.205	3.067	5.850	3.610
36.0	1.314	5.455	5.143	3.208	3.071	5.894	3.624
38.0	1.337	5.460	5.146	3.211	3.073	5.930	3.642
40.0	1.359	5.466	5.146	3.214	3.077	5.963	3.661
42.0	1.382	5.471	5.148	3.217	3.081	5.990	3.680
44.0	1.405	5.476	5.149	3.221	3.085	6.026	3.696
46.0	1.426	5.481	5.150	3.225	3.091	6.056	3.714
48.0	1.449	5.490	5.152	3.228	3.094	6.093	3.729
50.0	1.470	5.494	5.157	3.230	3.099	6.140	3.745
52.0	1.494	5.504	5.162	3.232	3.100	6.171	3.769
54.0	1.515	5.517	5.167	3.235	3.102	6.210	3.786
56.0	1.536	5.524	5.170	3.236	3.107	6.253	3.809
58.0	1.558	5.529	5.171	3.238	3.112	6.280	3.825
60.0	1.580	5.540	5.173	3.241	3.115	6.314	3.851

Table 5.1.10 Ultrasonic velocities of limestone (#1078)

P (MPa)	$-\Delta L$ (mm)	$V_{P_\parallel}$ (km/s)	$V_{P_\perp}$ (km/s)	$V_{S_\perp 1}$ (km/s)	$V_{S_\perp 2}$ (km/s)	V_P (km/s)	V_S (km/s)
0.0	0.000	4.079	4.122	2.375	2.384	4.057	2.324
0.1	0.835	4.079	4.121	2.375	2.384	4.066	2.324
0.6	0.936	4.081	4.120	2.376	2.383	4.068	2.327
1.2	0.971	4.085	4.120	2.376	2.383	4.076	2.333
1.8	0.997	4.088	4.119	2.377	2.382	4.079	2.338
2.4	1.021	4.090	4.117	2.378	2.382	4.082	2.343
3.0	1.043	4.093	4.116	2.378	2.381	4.084	2.346
4.0	1.069	4.094	4.114	2.379	2.380	4.093	2.350
6.0	1.113	4.099	4.112	2.379	2.378	4.109	2.363
8.0	1.155	4.105	4.110	2.380	2.378	4.117	2.369
10.0	1.192	4.106	4.109	2.380	2.377	4.129	2.379
12.0	1.225	4.107	4.107	2.381	2.374	4.139	2.384
14.0	1.258	4.108	4.103	2.381	2.372	4.148	2.390
16.0	1.289	4.111	4.100	2.381	2.370	4.158	2.398
18.0	1.319	4.112	4.093	2.380	2.367	4.171	2.403
20.0	1.349	4.112	4.085	2.379	2.365	4.181	2.410
22.0	1.378	4.111	4.077	2.378	2.363	4.196	2.420
24.0	1.407	4.110	4.066	2.378	2.361	4.212	2.431
26.0	1.437	4.109	4.058	2.377	2.353	4.222	2.435
28.0	1.466	4.109	4.049	2.377	2.347	4.232	2.441
30.0	1.496	4.107	4.028	2.376	2.344	4.243	2.449
32.0	1.525	4.103	4.016	2.372	2.340	4.253	2.456
34.0	1.555	4.097	4.002	2.368	2.330	4.268	2.460
36.0	1.585	4.094	3.981	2.365	2.316	4.280	2.464
38.0	1.616	4.085	3.947	2.358	2.300	4.290	2.470
40.0	1.648	4.083	3.920	2.355	2.290	4.307	2.477
42.0	1.682	4.076	3.873	2.349	2.274	4.312	2.483
44.0	1.714	4.064	3.845	2.342	2.254	4.322	2.490
46.0	1.750	4.052	3.778	2.337	2.227	4.335	2.495
48.0	1.793	4.038	3.700	2.328	2.193	4.345	2.505
50.0	1.837	4.008	3.646	2.306	2.156	4.355	2.510

5.2 Velocities of kerogen-rich shales

Original design

Data documented in this section was collected as part of the larger shale database built for studying the elastic and inelastic properties (velocity, anisotropy, and attenuation) of kerogen-rich shales and how they vary with mineralogy and hydrocarbon contents. Ultrasonic velocities of both compressional and shear modes, density, porosity, permeability (for limited number of samples) were measured in this experiment.

Experimental procedure

All samples were cored and cut to cylindrical shapes of approximately 1 inch (2.54 cm) in diameter and between 1 to 1.5 inch (2.54 to 3.81 cm) in length. Sample end surfaces were polished with sandwheel and the parallelism was checked with a caliper. They were then oven dried to 110 ^{o}C.

Density was calculated from sample weight and volume. Weight was measured with an electronic balance. Volumes were calculated from dimensions for regular samples or estimated from fluid overflow upon suspension for irregular samples.

Porosity was measured using standard Helium porosimeter for some samples and estimated from water saturation for others.

Permeability was measured using the high confining pressure (10 MPa) fluid permeameter equipment of USGS (Menlo Park, California).

XRD mineralogy and Rock-Eval for TOC content were done by Arco company.

Ultrasonic velocity was measured under confining pressure in a pressure vessel filled with silicone oil (dimethylpoly-siloxane, viscosity of 5 cs at 20 ^{o}C). The pressure levels selected for shale samples from different formations vary. The typical pressures are 2, 5, 10, 20, 30, 40 (or 50) MPa, for the Niobrara formation samples; the highest pressure is 90 MPa. At each pressure, waveforms (averaged over 16 times) were recorded and stored in the computer disk for later analysis.

Equipment and samples

Equipment

The equipment and its use for this experiment is listed below:

equipment	uses
pressure vessel in Stanford Rock Physics Lab	applying hydrostatic confining pressure
Velonex 570 high power pulse and burst generator	broad-band signal source
HP 222A pulse generator	trigger source
HP 54510A Digitizing Oscilloscope	broad-band signal receiving and digitizing
HP 465A amplifier Krohn-Hite 3202R filter	signal amplification reducing low frequency noise

Set-up

The systme is designed such that one P-wave signal and two S-wave (orthorgonal to each other) signals can be measured at one time on the same sample. The computer controled signal acquisition and data storage significantly eased the manual work and reduced experimentation time. Programming was an important part but less recognizable part of the shale project.

See Figure 5.2 (a) for a schematic diagram of the equipment set-up.

Samples

Most shale samples in this study have hexagonal symmetry and the elastic properties are transverse isotropic. Therefore, 3 plugs of orientations parallel, 45 degree, and perpendicular to bedding or lamination direction were taken next to each other from the same block. Two samples, however, contain two sets of cracks and five plugs were taken with three of them oriented along the bedding direction (two along the two orthogonal sets of cracks, one bisecting the two crack sets).

Samples for which data are presented here are from the Monterey formation (both outcrop and core) and the Niobrara formation.

Figure 5.2 (b) shows the sample orientations, wave modes, and propagation direction designations as used in the tables.

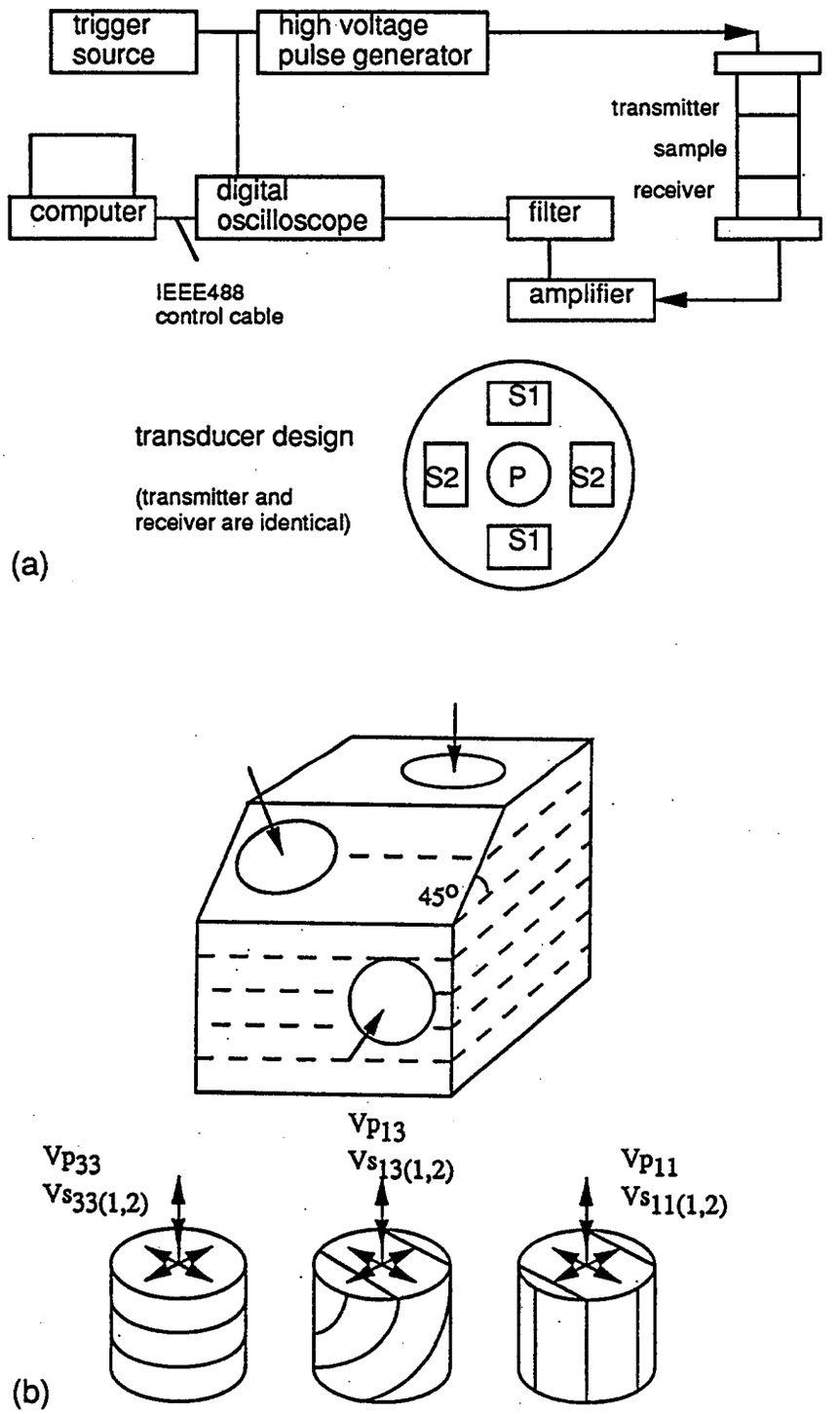

Figure 5.2: (a) A schematic diagram of the experimental setup used for the ultrasonic velocity measurements; (b) Sample orientations relative to bedding-plane and designations for measured velocities that are listed in data tables.

Tables

Data are organized according to the three groups. A separate sample parameter table is provided for each group.

Table 5.2.1 Parameters of the Monterey formation shale samples from the outcrop at Gaviota of Monterey, California

depth (ft)	depth (m)	Lithology	TOC ($\%wt$)	HI (mg/gOC)	Por (%)	Density (g/cm^3)
1	0	porcelanite			16.6	2.58
2	0	siliceous shale	7.93	572	28.8	2.19
3	0	shale	15.55	559	30.9	2.08
5	0	Opal-CT porcelanite	2.47	495	29.6	2.22
6	0	siliceous shale	3.61	735	10.3	2.49
7	0	shale	4.18	391	29.3	2.35
8	0	siliceous dolomite	1.60	439	5.9	2.72
9	0	shale	1.36	450	5.0	2.73

Table 5.2.2 Ultrasonic velocities of (room) dry samples

sample	P_c	$V_{P_{33}}$	$V_{P_{13}}$	$V_{P_{11}}$	$V_{S_{33}}$	$V_{S_{13_1}}$	$V_{S_{11_1}}$	$V_{S_{13_2}}$
1	5	3.59	3.74	4.28	2.26	2.34	2.43	2.18
	10	3.59	3.75	4.28	2.26	2.34	2.44	2.18
	20	3.60	3.75	4.29	2.26	2.34	2.44	2.19
	30	3.60	3.76	4.29	2.26	2.34	2.44	2.19
	50	3.62	3.77	4.29	2.27	2.34	2.44	2.19
2	5	2.38	2.54	2.82	1.63	1.71	1.75	1.64
	10	2.40	2.56	2.83	1.64	1.72	1.75	1.65
	20	2.45	2.58	2.85	1.65	1.73	1.76	1.66
	30	2.50	2.61	2.86	1.67	1.74	1.77	1.67
	50	2.58	2.67	2.90	1.69	1.76	1.78	1.70
3	5	2.20	2.38	2.51	1.43	1.49	1.57	1.46
	10	2.22	2.39	2.53	1.44	1.50	1.58	1.47
	20	2.28	2.43	2.56	1.46	1.51	1.59	1.48
	30	2.32	2.46	2.60	1.48	1.52	1.60	1.50
	50	2.40	2.54	2.67	1.51	1.54	1.62	1.52
5	5	2.58	2.82	3.20	1.75	1.83	2.04	1.82
	10	2.60	2.82	3.20	1.75	1.84	2.05	1.83
	20	2.62	2.84	3.20	1.76	1.84	2.05	1.83
	30	2.64	2.85	3.21	1.77	1.85	2.05	1.84
	50	2.68	2.88	3.22	1.79	1.86	2.05	1.85

(continued from last page of Table 5.2.2)

sample	P_c	$V_{P_{33}}$	$V_{P_{13}}$	$V_{P_{11}}$	$V_{S_{33}}$	$V_{S_{13_1}}$	$V_{S_{11_1}}$	$V_{S_{13_2}}$
6	5	4.41	4.49	4.65	2.66	2.74	2.93	2.70
	10	4.42	4.49	4.65	2.66	2.74	2.94	2.71
	20	4.42	4.50	4.66	2.66	2.75	2.94	2.71
	30	4.43	4.51	4.66	2.66	2.75	2.95	2.72
	50	4.44	4.52	4.67	2.66	2.75	2.95	2.73
7	5	2.20	2.55	2.77	1.59	1.77	1.83	1.61
	10	2.24	2.57	2.78	1.60	1.77	1.84	1.63
	20	2.30	2.62	2.81	1.63	1.79	1.85	1.65
	30	2.37	2.65	2.85	1.65	1.80	1.86	1.67
	50	2.48	2.73	2.90	1.69	1.81	1.88	1.70
8	5	4.43	4.64	5.00	2.83	2.90	2.96	2.76
	10	4.44	4.66	5.01	2.84	2.90	2.96	2.77
	20	4.46	4.67	5.03	2.84	2.90	2.96	2.78
	30	4.48	4.70	5.05	2.85	2.91	2.96	2.78
	50	4.52	4.74	5.09	2.86	2.91	2.96	2.79
9	5	4.43	4.78	4.93	2.74	2.95	3.04	2.84
	10	4.44	4.79	4.94	2.74	2.96	3.05	2.84
	20	4.47	4.80	4.96	2.75	2.97	3.05	2.85
	30	4.49	4.82	4.98	2.76	2.97	3.06	2.86
	50	4.54	4.85	5.01	2.77	2.98	3.07	2.87

Table 5.2.3 Ultrasonic velocities of brine saturated samples

sample	P_c	$V_{P_{33}}$	$V_{P_{13}}$	$V_{P_{11}}$	$V_{S_{33}}$	$V_{S_{13_1}}$	$V_{S_{11_1}}$	$V_{S_{13_2}}$
1	5	3.60	3.70	4.28	2.03	2.08	2.16	1.95
	10	3.64	3.75	4.31	2.05	2.10	2.17	1.98
	20	3.69	3.80	4.34	2.07	2.12	2.18	2.00
	30	3.74	3.85	4.36	2.08	2.13	2.19	2.01
	50	3.82	3.91	4.39	2.11	2.16	2.20	2.04
2	5	2.52	2.56	2.72	1.33	1.36	1.41	1.28
	10	2.56	2.60	2.75	1.34	1.37	1.42	1.30
	20	2.61	2.65	2.80	1.36	1.38	1.44	1.31
	30	2.65	2.69	2.84	1.37	1.39	1.45	1.32
	50	2.71	2.75	2.89	1.39	1.41	1.47	1.36
3	5	2.12	2.10	2.23	1.14	1.24	1.36	1.16
	10	2.20	2.16	2.30	1.15	1.25	1.39	1.17
	20	2.28	2.24	2.38	1.17	1.27	1.41	1.18
	30	2.36	2.33	2.47	1.20	1.29	1.43	1.21
	50	2.48	2.45	2.58	1.24	1.31	1.46	1.24
5	5	2.60	2.74	3.06	1.38	1.46	1.77	1.48
	10	2.62	2.77	3.08	1.39	1.47	1.78	1.50
	20	2.66	2.81	3.10	1.40	1.48	1.79	1.52
	30	2.70	2.85	3.13	1.41	1.50	1.80	1.53
	50	2.74	2.88	3.15	1.42	1.52	1.81	1.55

(continued from last page of Table 5.2.3)

sample	P_c	$V_{P_{33}}$	$V_{P_{13}}$	$V_{P_{11}}$	$V_{S_{33}}$	$V_{S_{13_1}}$	$V_{S_{11_1}}$	$V_{S_{13_2}}$
6	5	4.34	4.43	4.63	2.52	2.54	2.69	2.52
	10	4.37	4.46	4.66	2.53	2.55	2.70	2.54
	20	4.41	4.49	4.70	2.55	2.56	2.72	2.56
	30	4.44	4.52	4.73	2.56	2.57	2.73	2.57
	50	4.48	4.56	4.77	2.58	2.59	2.75	2.59
7	5	2.42	2.57	2.68	1.22	1.33	1.43	1.30
	10	2.48	2.62	2.72	1.24	1.35	1.44	1.31
	20	2.54	2.67	2.77	1.27	1.37	1.46	1.33
	30	2.60	2.71	2.81	1.29	1.40	1.47	1.34
	50	2.66	2.77	2.88	1.32	1.42	1.49	1.35
8	5	4.66	4.82	5.20	2.58	2.65	2.78	2.57
	10	4.72	4.87	5.24	2.61	2.67	2.80	2.60
	20	4.83	4.95	5.28	2.64	2.70	2.82	2.63
	30	4.91	5.01	5.32	2.67	2.73	2.84	2.66
	50	5.03	5.12	5.40	2.72	2.78	2.87	2.72
9	5	4.68	4.95	5.17	2.59	2.70	2.77	2.65
	10	4.75	5.02	5.23	2.62	2.73	2.80	2.69
	20	4.86	5.11	5.31	2.66	2.77	2.83	2.73
	30	4.93	5.17	5.38	2.69	2.80	2.85	2.76
	50	5.00	5.25	5.46	2.73	2.84	2.89	2.81

Table 5.2.4 Parameters of the Monterey formation shale samples from the Union-Leroy 51-18 well in Santa Maria Valley field, Santa Maria basin, California

depth (ft)	depth (m)	Lithology	TOC ($\%wt$)	HI (mg/gOC)	Por (%)	Density (g/cm^3)	Dip ($^\circ$)
4560	1390	Opal-CT porcelanite	2.40	537	11.4	2.17	47
4571	1393	Opal-CT porcelanite	2.28	546	10	2.14	45
4590	1399	dolomite	0.19c	316	3	2.72	45
4642	1415	siliceous dolomite	8.12	655	16.5	2.38	40
4685	1428	shale	8.19	645	21	2.35	35
4696	1431	shale	18.22	527	21	2.02	33
4771	1454	siliceous dolomite	5.83	692	19	2.49	30
4798	1462	shale	9.31c	657	18	2.35	32
5478	1670	siliceous shale	6.81	583	5	2.24	
5553	1693	siliceous dolomite	0.52	423	11	2.70	

Table 5.2.5 Ultrasonic velocities of (room) dry samples

sample	P_c	$V_{P_{33}}$	$V_{S_{33\parallel}}$	$V_{S_{33\perp}}$	$V_{P_{13}}$	$V_{S_{13\parallel}}$	$V_{S_{13\perp}}$
4560	2	3.82	2.52	2.44	3.79	2.42	2.45
	5	3.84	2.53	2.46	3.81	2.45	2.48
	10	3.86	2.54	2.48	3.83	2.48	2.50
	20	3.88	2.55	2.50	3.85	2.51	2.53
	30	3.90	2.56	2.51	3.87	2.53	2.56
	40	3.91	2.57	2.52	3.89	2.54	2.58
4571	2	3.70	2.44	2.45	3.76	2.47	2.44
	5	3.71	2.45	2.46	3.77	2.48	2.45
	10	3.72	2.46	2.47	3.78	2.49	2.46
	20	3.74	2.47	2.48	3.80	2.51	2.48
	30	3.75	2.48	2.49	3.81	2.52	2.49
	40	3.76	2.49	2.50	3.82	2.53	2.50

cont'd	$V_{P_{11}}$	$V_{S_{11\parallel}}$	$V_{S_{11\perp}}$	$V_{P_{12}}$	$V_{S_{12\parallel}}$	$V_{S_{12\perp}}$	$V_{P_{22}}$	$V_{S_{22\parallel}}$	$V_{S_{22\perp}}$
	4.12	2.32	2.43	4.20	2.56	2.37	4.05	2.49	2.47
	4.15	2.36	2.45	4.21	2.58	2.38	4.09	2.51	2.48
	4.17	2.39	2.48	4.23	2.60	2.40	4.12	2.54	2.49
	4.20	2.43	2.51	4.25	2.62	2.43	4.15	2.58	2.50
	4.21	2.45	2.53	4.27	2.63	2.45	4.17	2.60	2.51
	4.23	2.47	2.54	4.28	2.64	2.46	4.19	2.61	2.51
	3.85	2.45	2.43	3.89	2.53	2.49	3.92	2.58	2.53
	3.86	2.46	2.44	3.90	2.54	2.51	3.93	2.59	2.54
	3.87	2.47	2.45	3.91	2.55	2.52	3.94	2.60	2.56
	3.88	2.49	2.46	3.92	2.57	2.55	3.95	2.61	2.59
	3.88	2.50	2.47	3.92	2.58	2.55	3.95	2.62	2.59
	3.89	2.51	2.48	3.93	2.59	2.56	3.96	2.63	2.60

(continued from last page of Table 5.2.5)

sample	P_c	$V_{P_{33}}$	$V_{S_{33_1}}$	$V_{S_{33_2}}$	$V_{P_{13}}$	$V_{S_{13_1}}$	$V_{S_{13_2}}$	$V_{P_{22}}$	$V_{S_{11_1}}$	$V_{S_{11_2}}$
4590	2	5.95	3.48	3.51	5.75	3.36	3.29	6.72	3.71	3.62
	5	6.03	3.50	3.53	5.85	3.39	3.32	6.76	3.72	3.63
	10	6.10	3.53	3.56	5.95	3.43	3.37	6.81	3.73	3.65
	20	6.17	3.56	3.58	6.05	3.47	3.41	6.87	3.75	3.67
	30	6.23	3.59	3.61	6.11	3.49	3.44	6.92	3.77	3.69
	40	6.29	3.61	3.62	6.17	3.52	3.46	6.97	3.78	3.72
4642	2	2.89	1.90	1.91	3.05	2.02	1.81	3.52	2.20	2.02
	5	3.02	1.95	1.94	3.13	2.05	1.88	3.55	2.22	2.05
	10	3.12	1.99	1.98	3.22	2.08	1.93	3.60	2.24	2.08
	20	3.25	2.04	2.04	3.33	2.13	2.00	3.68	2.27	2.13
	30	3.37	2.08	2.09	3.44	2.17	2.04	3.75	2.30	2.17
	40	3.45	2.12	2.12	3.53	2.21	2.08	3.83	2.33	2.19
4685	2	1.82	1.46	1.48				2.94	1.76	1.47
	5	1.91	1.49	1.51				2.98	1.78	1.49
	10	2.05	1.52	1.56				3.03	1.81	1.52
	20	2.32	1.60	1.60				3.12	1.86	1.54
	30	2.52	1.66	1.66				3.22	1.90	1.58
	40	2.68	1.72	1.72				3.28	1.94	1.62
4696	2	2.02	1.41	1.45	2.46	1.78	1.49	3.22	2.05	1.40
	5	2.13	1.44	1.47	2.55	1.80	1.53	3.26	2.06	1.42
	10	2.25	1.48	1.49	2.65	1.82	1.56	3.29	2.07	1.46
	20	2.37	1.52	1.52	2.76	1.84	1.59	3.31	2.08	1.49
	30	2.49	1.56	1.54	2.84	1.86	1.62	3.34	2.09	1.52
	40	2.56	1.59	1.56	2.89	1.88	1.65	3.36	2.10	1.54

(continued from last page of Table 5.2.5)

sample	P_c	$V_{P_{33}}$	$V_{S_{33_1}}$	$V_{S_{33_2}}$	$V_{P_{13}}$	$V_{S_{13_1}}$	$V_{S_{13_2}}$	$V_{P_{22}}$	$V_{S_{11_1}}$	$V_{S_{11_2}}$
4771	2	2.42	1.65	1.69	2.78	1.84	1.77	3.24	1.96	1.63
	5	2.51	1.70	1.71	2.84	1.87	1.80	3.28	1.98	1.66
	10	2.59	1.74	1.73	2.91	1.90	1.84	3.35	2.01	1.72
	20	2.77	1.80	1.79	3.05	1.95	1.90	3.45	2.06	1.79
	30	2.90	1.85	1.84	3.16	2.00	1.96	3.56	2.10	1.83
	40	3.01	1.89	1.92	3.24	2.04	2.01	3.64	2.14	1.87
4798	2	2.20	1.69	1.64	2.64	1.78	1.67	3.20	1.93	1.48
	5	2.38	1.72	1.71	2.71	1.81	1.72	3.23	1.95	1.51
	10	2.50	1.79	1.75	2.81	1.85	1.76	3.26	1.97	1.56
	20	2.67	1.84	1.82	2.92	1.90	1.82	3.30	2.00	1.62
	30	2.77	1.87	1.87	2.99	1.94	1.86	3.33	2.02	1.65
	40	2.85	1.92	1.88	3.04	1.97	1.90	3.37	2.04	1.68
5478	2	3.60	2.37	2.33	3.69	2.35	2.31	4.06	2.60	2.50
	5	3.62	2.38	2.34	3.71	2.36	2.33	4.07	2.61	2.53
	10	3.64	2.40	2.35	3.74	2.37	2.35	4.08	2.62	2.54
	20	3.66	2.41	2.36	3.77	2.38	2.36	4.10	2.63	2.55
	30	3.68	2.42	2.38	3.79	2.39	2.37	4.11	2.64	2.56
	40	3.70	2.43	2.39	3.82	2.40	2.38	4.12	2.65	2.58
5553	2	4.57	2.73	2.91				5.32	3.32	2.98
	5	4.66	2.79	2.92				5.34	3.33	3.01
	10	4.73	2.85	2.94				5.37	3.34	3.02
	20	4.83	2.90	2.96				5.40	3.36	3.04
	30	4.93	2.94	2.99				5.43	3.37	3.06
	40	5.03	2.99	3.02				5.46	3.38	3.08

Table 5.2.6 Ultrasonic velocities of brine saturated samples

sample	P_c	$V_{P_{33}}$	$V_{S_{33\parallel}}$	$V_{S_{33\perp}}$	$V_{P_{13}}$	$V_{S_{13\parallel}}$	$V_{S_{13\perp}}$
	2	3.85	2.46	2.45	3.83	2.57	2.54
	5	3.87	2.47	2.46	3.84	2.58	2.55
	10	3.88	2.48	2.47	3.86	2.59	2.56
	20	3.89	2.48	2.48	3.88	2.60	2.58
	30	3.90	2.48	2.49	3.90	2.61	2.59
	40	3.92	2.49	2.50	3.91	2.62	2.60
	2	3.67	2.29	2.41	3.74	2.46	2.45
	5	3.69	2.33	2.43	3.75	2.49	2.46
	10	3.71	2.35	2.45	3.76	2.52	2.47
	20	3.73	2.38	2.46	3.78	2.54	2.48
	30	3.74	2.39	2.48	3.79	2.56	2.49
	40	3.75	2.40	2.48	3.80	2.57	2.50

(contd)	$V_{P_{11}}$	$V_{S_{11\parallel}}$	$V_{S_{11\perp}}$	$V_{P_{12}}$	$V_{S_{12\parallel}}$	$V_{S_{12\perp}}$	$V_{P_{22}}$	$V_{S_{22\parallel}}$	$V_{S_{22\perp}}$
	4.12	2.54	2.31	4.20	2.59	2.32	4.30	2.69	2.43
	4.13	2.55	2.31	4.21	2.60	2.35	4.31	2.70	2.44
	4.14	2.56	2.32	4.23	2.61	2.36	4.32	2.71	2.44
	4.16	2.57	2.33	4.25	2.62	2.38	4.34	2.72	2.45
	4.18	2.59	2.34	4.27	2.63	2.40	4.36	2.73	2.46
	4.20	2.60	2.35	4.29	2.64	2.41	4.38	2.74	2.46
	3.81	2.38	2.32	3.86	2.41	2.38	4.05	2.54	2.53
	3.83	2.39	2.32	3.88	2.43	2.39	4.06	2.56	2.54
	3.84	2.40	2.32	3.89	2.44	2.40	4.07	2.57	2.54
	3.85	2.41	2.33	3.91	2.46	2.41	4.08	2.59	2.56
	3.86	2.42	2.33	3.92	2.47	2.42	4.09	2.60	2.56
	3.88	2.43	2.34	3.94	2.48	2.43	4.10	2.61	2.57

(continued from last page of Table 5.2.6)

sample	P_c	$V_{P_{33}}$	$V_{S_{33_1}}$	$V_{S_{33_2}}$	$V_{P_{13}}$	$V_{S_{13_1}}$	$V_{S_{13_2}}$	$V_{P_{22}}$	$V_{S_{11_1}}$	$V_{S_{11_2}}$
4590	2	6.17	3.40	3.39	5.96	3.30	3.20	6.84	3.67	3.55
	5	6.21	3.42	3.41	6.05	3.34	3.23	6.86	3.68	3.57
	10	6.26	3.45	3.42	6.12	3.38	3.27	6.88	3.69	3.58
	20	6.34	3.48	3.46	6.17	3.43	3.30	6.92	3.70	3.62
	30	6.38	3.51	3.49	6.22	3.47	3.34	6.95	3.71	3.64
	40	6.43	3.53	3.51	6.27	3.50	3.37	6.99	3.72	3.67
4642	2	3.10	1.73	1.73	3.25	1.88	1.70	3.56	1.97	1.84
	5	3.22	1.79	1.81	3.32	1.91	1.77	3.65	2.01	1.87
	10	3.33	1.84	1.85	3.42	1.94	1.82	3.74	2.04	1.92
	20	3.46	1.91	1.91	3.55	1.98	1.89	3.86	2.08	1.97
	30	3.52	1.95	1.95	3.63	2.01	1.94	3.94	2.11	2.00
	40	3.58	1.98	1.97	3.69	2.03	1.98	3.98	2.13	2.02
4685	2	2.61	1.46	1.48				3.00	1.57	1.32
	5	2.69	1.49	1.50				3.06	1.60	1.35
	10	2.76	1.51	1.52				3.13	1.62	1.37
	20	2.90	1.52	1.53				3.20	1.66	1.40
	30	3.00	1.54	1.55				3.28	1.68	1.42
	40	3.07	1.56	1.56				3.34	1.70	1.44
4696	2	2.35	1.45	1.46	2.49	1.48	1.32	2.74	1.56	1.47
	5	2.43	1.47	1.50	2.57	1.50	1.35	2.78	1.57	1.48
	10	2.53	1.51	1.51	2.64	1.52	1.37	2.84	1.59	1.50
	20	2.66	1.54	1.52	2.75	1.54	1.39	2.91	1.61	1.51
	30	2.73	1.56	1.54	2.82	1.56	1.41	2.98	1.63	1.51
	40	2.78	1.57	1.56	2.87	1.58	1.42	3.03	1.65	1.54

(continued from last page of Table 5.2.6)

sample	P_c	$V_{P_{33}}$	$V_{S_{33_1}}$	$V_{S_{33_2}}$	$V_{P_{13}}$	$V_{S_{13_1}}$	$V_{S_{13_2}}$	$V_{P_{22}}$	$V_{S_{11_1}}$	$V_{S_{11_2}}$
4771	2	2.43	1.34	1.36	3.04	1.57	1.78	3.28	1.65	1.54
	5	2.53	1.37	1.41	3.15	1.61	1.80	3.42	1.70	1.57
	10	2.62	1.40	1.43	3.26	1.68	1.82	3.55	1.75	1.60
	20	2.72	1.46	1.45	3.38	1.76	1.84	3.72	1.80	1.64
	30	2.79	1.47	1.48	3.46	1.81	1.86	3.82	1.85	1.67
	40	2.84	1.48	1.50	3.53	1.85	1.88	3.88	1.89	1.71
4798	2	2.76	1.56	1.58	2.83	1.63	1.61	2.87	1.66	1.42
	5	2.85	1.58	1.61	2.92	1.65	1.64	2.95	1.67	1.44
	10	2.96	1.61	1.63	3.01	1.67	1.66	3.05	1.69	1.44
	20	3.06	1.64	1.66	3.13	1.70	1.68	3.17	1.71	1.46
	30	3.18	1.67	1.67	3.23	1.72	1.70	3.26	1.73	1.48
	40	3.25	1.69	1.67	3.30	1.73	1.71	3.36	1.74	1.49
5478	2	3.72	2.35	2.30	3.60	2.17	2.09	4.10	2.49	2.21
	5	3.74	2.35	2.31	3.63	2.18	2.10	4.12	2.50	2.24
	10	3.76	2.36	2.33	3.65	2.19	2.12	4.15	2.51	2.25
	20	3.79	2.36	2.35	3.69	2.21	2.16	4.18	2.53	2.26
	30	3.81	2.37	2.35	3.72	2.22	2.18	4.21	2.55	2.29
	40	3.83	2.37	2.36	3.75	2.23	2.20	4.23	2.56	2.31
5553	2	4.69	2.60	2.70				5.38	3.23	2.75
	5	4.78	2.68	2.74				5.42	3.27	2.80
	10	4.89	2.76	2.78				5.46	3.33	2.84
	20	5.05	2.88	2.87				5.53	3.42	2.90
	30	5.20	2.98	2.95				5.60	3.49	2.94
	40	5.31	3.06	3.00				5.67	3.54	2.96

Table 5.2.7 Parameters of the Niobraraformation shale samples

depth (ft)	depth (m)	Lithology	TOC ($\%wt$)	HI (mg/gOC)	Por (%)	Density (g/cm^3)
3620	1103	shale	1.3	124	6.4	2.71
3679	1121	shale	1.15	107	3.2	2.71
3803	1159	shale	1.93	120	4.6	2.69
3915	1193	shale	0.82	66	8.1	2.80
3975	1212	shale	1.02	72	8.4	2.83
7376	2248	shale	2.13	19	5.7	2.65
7451	2271	shale	1.69	16	6.7	2.75
7622	2323	shale	1.60	7	7.0	2.80
7709	2350	shale	0.53	15	5.8	2.71
7762	2366	shale	1.01	10	6.0	2.77

Table 5.2.8 Ultrasonic velocities of (room) dry samples

sample	P_c	$V_{P_{33}}$	$V_{P_{13}}$	$V_{P_{11}}$	$V_{S_{33}}$	$V_{S_{13_1}}$	$V_{S_{11_1}}$	$V_{S_{13_2}}$
3679	5	3.94	4.26	5.03	2.55	2.64	3.04	2.52
	10	4.05	4.31	5.09	2.59	2.66	3.06	2.56
	20	4.16	4.42	5.14	2.64	2.70	3.09	2.64
	30	4.27	4.50	5.21	2.68	2.73	3.11	2.66
	50	4.43	4.64	5.31	2.72	2.77	3.14	2.70
	70	4.55	4.75	5.39	2.76	2.80	3.17	2.74
	90	4.65	4.85	5.48	2.79	2.83	3.19	2.78
3803	5	3.49	4.01	4.74	2.29	2.53	2.83	2.38
	10	3.64	4.11	4.78	2.34	2.55	2.85	2.41
	20	3.85	4.22	4.83	2.38	2.59	2.87	2.48
	30	4.00	4.34	4.89	2.41	2.60	2.90	2.53
	50	4.17	4.46	4.96	2.46	2.64	2.92	2.58
	70	4.31	4.56	5.02	2.50	2.66	2.94	2.61
	90	4.39	4.64	5.11	2.53	2.68	2.96	2.63
7376	5	3.11	3.68	4.46	2.08	2.35	2.78	2.24
	10	3.36	3.79	4.52	2.16	2.40	2.81	2.29
	20	3.55	3.94	4.58	2.23	2.44	2.83	2.32
	30	3.71	4.06	4.65	2.26	2.47	2.85	2.35
	50	3.90	4.21	4.76	2.33	2.51	2.87	2.41
	70	4.06	4.31	4.83	2.36	2.53	2.91	2.46
	90	4.13	4.39	4.90	2.39	2.56	2.94	2.49

(continued from last page of Table 5.2.8)

sample	P_c	$V_{P_{33}}$	$V_{P_{13}}$	$V_{P_{11}}$	$V_{S_{33}}$	$V_{S_{13_1}}$	$V_{S_{11_1}}$	$V_{S_{13_2}}$
7622	5	3.07	3.83	4.57	2.11	2.41	2.76	2.20
	10	3.41	3.96	4.65	2.19	2.47	2.79	2.30
	20	3.69	4.10	4.72	2.26	2.51	2.82	2.38
	30	3.86	4.20	4.79	2.31	2.55	2.85	2.45
	50	4.08	4.34	4.87	2.39	2.60	2.88	2.53
	70	4.23	4.45	4.96	2.43	2.63	2.90	2.57
	90	4.31	4.54	5.01	2.46	2.65	2.93	2.60
7709	5	3.30	3.82	4.80	2.28	2.51	2.91	2.41
	10	3.65	3.95	4.86	2.35	2.55	2.92	2.46
	20	3.90	4.11	4.93	2.43	2.62	2.95	2.56
	30	4.08	4.23	5.01	2.48	2.67	2.97	2.63
	50	4.29	4.40	5.10	2.53	2.72	2.99	2.68
	70	4.40	4.53	5.17	2.56	2.76	3.02	2.72
	90	4.52	4.62	5.24	2.60	2.80	3.04	2.77
7762	5	3.39	4.04	4.48	2.29	2.51	2.78	2.27
	10	3.67	4.20	4.53	2.38	2.56	2.80	2.35
	20	3.92	4.35	4.61	2.49	2.61	2.84	2.47
	30	4.11	4.47	4.68	2.55	2.66	2.87	2.55
	50	4.36	4.66	4.82	2.64	2.74	2.91	2.67
	70	4.51	4.81	4.97	2.68	2.80	2.96	2.71
	90	4.61	4.91	5.06	2.70	2.85	2.99	2.76

Table 5.2.9 Ultrasonic velocities of brine saturated samples

sample	P_c	$V_{P_{33}}$	$V_{P_{13}}$	$V_{P_{11}}$	$V_{S_{33}}$	$V_{S_{13_1}}$	$V_{S_{11_1}}$	$V_{S_{13_2}}$
3803	5	3.75	4.00	4.55	2.00	2.28	2.53	2.19
	10	3.86	4.09	4.64	2.04	2.30	2.56	2.23
	20	3.99	4.21	4.73	2.11	2.36	2.62	2.29
	30	4.09	4.31	4.79	2.16	2.40	2.65	2.35
	50	4.25	4.44	4.89	2.25	2.48	2.72	2.43
	70	4.35	4.53	4.98	2.31	2.53	2.76	2.48
	90	4.45	4.62	5.06	2.34	2.57	2.80	2.49
7709	5	3.89	4.10	4.59	2.03	2.27	2.57	2.24
	10	3.95	4.16	4.65	2.07	2.29	2.61	2.26
	20	4.09	4.26	4.74	2.11	2.32	2.65	2.31
	30	4.16	4.32	4.84	2.14	2.34	2.67	2.33
	50	4.22	4.38	4.95	2.18	2.38	2.74	2.36
	70	4.26	4.43	5.03	2.21	2.40	2.78	2.39
	90	4.29	4.47	5.08	2.23	2.42	2.80	2.41